Final Report:

Development of tools for coupled InSAR and Seismicity monitoring of EGS reservoir development and management

Funding Opportunity Announcement:
DE-FOA-0000522

Award Number:
DE-EE0005510

PI: Nicholas Davatzes, Temple University
Co-PIs: Kurt Feigl[1], Herb Wang[1], Rob Mellors[2], Bill Foxall[2], Denise Templeton[2], Tabrez Ali, **Co-I:** Peter Drakos[3]
[1]University of Wisconsin–Madison; [2]Lawrence Livermore National Laboratory, [3]ORMAT

This material is based upon work supported by the U.S. Department of Energy's Office of Energy Efficiency and Renewable Energy (EERE) under the Geothermal Technologies Office award number DE-EE0005510.

EXECUTIVE SUMMARY

Development and management of a geothermal resource is significantly hampered by the large degree of uncertainty in the potential geometry of the resource and its key mechanical and hydrologic properties. Wells provide detailed insights but are so spatially restricted that they only benchmark these attributes sparsely, and *if* the well successfully intersects hot, permeable rock. During production of either a traditional or enhanced geothermal system from a limited number of wells, much of uncertainty in the reservoir geometry and its properties persist. As a result, there is limited basis to inform management of the reservoir or potential for further development of regions appropriate for stimulation. Ultimately, this leads to degrading well performance, uncertainty in injection strategies, and drilling of failed wells or failed stimulations that raise the Levelized Cost of Energy (LCOE).

We have successfully developed software tools to: (1) implement systematic analyses that improve the definition of a reservoir by investigating reservoir responses to pumping such as surface deformation and induced seismicity (2) demonstrate the viability of this procedure through application to the Brady Geothermal field, NV.

The primary products are detailed workflows from the initial capture of raw data through data processing, model development and calibration, and delivery of data products have been developed. These workflows incorporate cutting edge techniques in InSAR and seismology including new tools developed within the scope of this project and also incorporates previously developed cutting edge tools most of which are available as free ware or open-source software. The software also includes tools to format and pipe data between steps in the workflow.

Three workflow modules are defined:

(1) A module using the history of the surface displacement field to constrain the geometry and position of subsurface volume changes accompanying pumping (SOPO Task 1);
(2) Analysis of seismicity including improved earthquake locations and determination of seismic attributes (SOPO Task 2);
(3) Reservoir modeling that assesses the key mechanisms of deformation in the reservoir and then the reservoir characteristics compatible with the pumping records, surface deformations and seismicity (SOPO Task 3).

Key advances include clear relationship between injection pressures and seismicity (Cardiff et al., 2018), an unparalleled set of images detailing surface deformation (Ali et al., 2016b; Feigl GDR/NGDS), and low-cost measurements of the seismic velocity structure using either seismic interferometry or tomography (Phase 1 Technical Report, Appendix). The use of templates proved useful in identifying characteristic seismic noise using novel means.

The combined analysis serves to: (a) identify the key physical processes governing the reservoir response to pumping, (b) evaluate natural sources of recharge or fluid loss to the reservoir, (c) define the uncertainty in key model parameters, (c) develop conceptual models of the reservoir, and (d) test competing hypotheses. As implemented, the workflow successfully fulfills the requirement of Phase I of the project.

To demonstrate the viability of these workflows, we have applied it to Brady Geothermal field by analysis of production behavior from 2004 through 2014 and an EGS stimulation attempted on one well during the project period. We have incorporated observations of surface deformation, a database of well characteristics, laboratory measured rock properties, a 3D geologic model, pumping records, SAR scenes, and seismicity. These results focus on the successful evaluation of surface deformation and improved understanding of the intermittent seismicity in this geothermal field.

Table of Contents

TECHNICAL DOCUMENT

1.0 Project Goals and Metrics

1.1 Background and Objectives

The goal of this project is to develop a set of tools to monitor the evolution of fluid flow within a geothermal system or during and following stimulation to create an Enhanced Geothermal System (EGS). These tools enable the location and geometry of the reservoir to be constrained. Combined with an appropriate geomechanical model, the permeability, porosity, saturation and pore pressure distribution can also be constrained. The information on the production volume can also inform the location of new wells and metrics for stimulation wells such as minimum distances the stimulation must extend. The comparison between injection volume, production volume, and volume change of the subsurface reservoir also provide insights into the long-term water balance and hydrology of the reservoir. Furthermore, such an analysis provides essential information of the "pre-stressing" of the reservoir and surrounding volume that can strongly influence stimulation success and aid in mitigating seismic hazard.

The ability to inform these decisions provides a basis to optimize long-term field management including evaluation of the longevity of permeability and porosity, drawdown or fluid sources supporting the reservoir as well as the short and long-term impacts of stimulation.

We have successfully met the objectives of the project to: (1) provide new constraints on the geometry and properties of a geothermal reservoir from seismicity and surface deformation induced by pumping at the Brady Geothermal Field; (2) develop a systematic procedure to support determination and updating of these constraints by defining analysis workflows supported by software tools to implement the workflow steps.Reservoir characteristics are constrained by correlating pumping to resulting micro-seismicity and surface deformation as measured by Interferometric Synthetic Aperture Radar (InSAR) and Global Positioning System (GPS) through a geomechanical model. Together, these data sets provide a temporally and spatially rich constraint that exploits two distinct responses to stress change induced by pumping that depend on evolving reservoir characteristics. The tools include workflows and supporting software to analyze the InSAR/GPS and seismicity data, and conduct the geomechanical modeling. The model also tests the suitability of different rheologies including elasticity, poroelasticity, thermoelasticity, and poroplasticity to best explain the correlation between pumping and the responding deformation. The final analysis of Brady indicated the thermal contraction within a finite volume was the most important element to consider (Ali et al., 2016; Reinish et al., 2018), which can most easily and efficiently be modeled using elastic dislocations with specified volume change.

These tools were developed using data from the Brady Geothermal Area and in close coordination with the operator. Testing of the tools in realistic scenarios was accomplished by analysis of production behavior from 2004 through 2014 and an EGS stimulation attempted on one well during the project period. The PoroTomo project (Feigl et al., 2020, DE-EE0006760) funded by DOE, which developed as a direct result early work in this project, performed a reservoir-wide flow test to further probe reservoir properties at even higher resolution.

Synergy with PoroTomo and Brady EGS: Note that this project works in synergy with PoroTomo for continued data acquisition, submissions to the GDR, and coordinated development of tools to enhance the analysis. The project benefited from overlapping timelines and consequently similar completion dates. The InSAR and MEQ project has also worked in conjunction with the Brady EGS (DE-FG36-08GO1820008GO1820) project for planning, post stimulation evaluation, and data management (which was incorporated into the Brady EGS Final Report and GDR submission). The result has been an extension in the period of acquisition of pumping, SAR, and seismicity data as well as coordinate archival of that data among the collective partners of these studies.

This project meets the objectives of the DOE Geothermal Technologies Program and funding announcement DE-FOA-0000522 by:

- Providing tools to enhance the use of seismicity in monitoring stimulation or production activity through better data processing
- Providing tools to define the geometry of the geothermal reservoir and measure fluid pressure fluctuations correlated to pumping activity
- Providing rapid development of technology to monitor and guide stimulation during the development of enhanced geothermal systems (EGS)
- Integrating these tools into a data collection framework ("workflow") facilitating assessment of stimulations and injection/production

From an operations perspective, the resulting information increases production efficiencies and lowers the levelized cost of electricity (LCOE) by:

- Improving management of injection/production practice to more efficiently sweep heat and minimize fluid losses;
- Improving siting of new wells (Reduced potential of failed wells) by defining the volume in communication with existing wells;
- Assessing stimulation potential from the proximity of tight wells to the reservoir;
- Avoiding development of short circuits.

An additional goal of this project is a better understanding of the correlation between induced seismicity and pumping under production, injection, and stimulation conditions.

Technical Barriers and Targets

Stimulation and management of enhanced geothermal system (EGS) reservoirs involves manipulating the fluid pressure at depth to create new permeability. These pressure changes cause two distinct effects: (1) slip on fractures that can often be detected as seismic events and (2) expansion or contraction revealed by displacements at the ground surface. To date, managing EGS stimulation has relied on monitoring induced seismicity to map the extent of fluid pressure perturbations and to identify the volume of connected porosity that results from opening new fractures or dilation that occurs where fractures slip. These pressure changes occur throughout the lifespan of the reservoir and could reveal the changing geometry of the fracture network over time. ***Thus, the primary objective of the research is to develop a framework and tools to monitor stimulation and reservoir management to better define the reservoir***.

The use of seismicity to map permeability creation presumes that the percolation of the stimulation fluid pressure initiates shear failure of fractures due to the reduction of normal stress resulting in slip and/or creates new opening-mode fractures, and that these failure events are sensible through microseismic monitoring thus revealing the extent of stimulation. However, the volume of increased fluid pressure must first expand to invade well-oriented, highly stressed fractures, which may be preceded by stress changes in the host rock. The expanding pressurized volume will also have a complex relationship to the history of pumping at the surface, the initial permeability structure, and the stresses measured at the well. Currently, no tool effectively provides direct monitoring of the progress of fluid pressure into the natural fracture network or surrounding formation. This problem is exacerbated by the simple fact that the displacement of fracture walls may be either aseismic or below the detection threshold of the local seismic network.

This lack of tools to map the pressurized volume leaves several key issues un-resolved including: (1) What is the initial geometry of the reservoir (early in exploitation or prior to

stimulation)? (2) What is the geometry of the pathways that connect pore space enhanced by stimulation? (3) How does access to the stimulated volume evolve during and after stimulation? (4) How does the pre-stressing of the reservoir from tectonic or prior pumping influence the stimulation behavior? (5) How is induced seismicity related to injection/production and the volume experiencing fluid flow and pore pressure change? (6) What is the driving mechanism of induced seismicity? (7) Does the 3D stress and fracture model from well analysis used in designing the stimulation plan predict the growth of the reservoir?

The primary technical target is to constrain the geometry and properties of the reservoir at a higher resolution than can practically be provided by wells during stimulation and production phases of EGS development. The improved resolution is derived from monitoring surface deformations and MEQ activity as responses to injection/production as well as tectonics (Figure 1.1-1).

- Develop a database to support tool development and testing including: (1) Geology, Faults, Alteration history; (2) Stress state from well observations; (3) Petrophysical properties; (4) Pumping/Injection and Temperature records. (5) Acquire ALOS SAR scenes archived prior to initiation of this project and continuously acquire TerraSAR-X scenes during the course of the project. (6) Acquire the MEQ catalog managed by Lawrence Berkeley National Laboratory.
- Characterize time history of deformation from (1) InSAR and (2) Seismicity.
- Model deformation history as a *response* to pumping history using appropriate rheologies to infer the development and geometry of the (1) pore pressure field and (2) permeable volume hosting fluid flow during normal operations and EGS stimulation.
- Develop software tools to conduct the analyses and pass data between steps in the workflow.

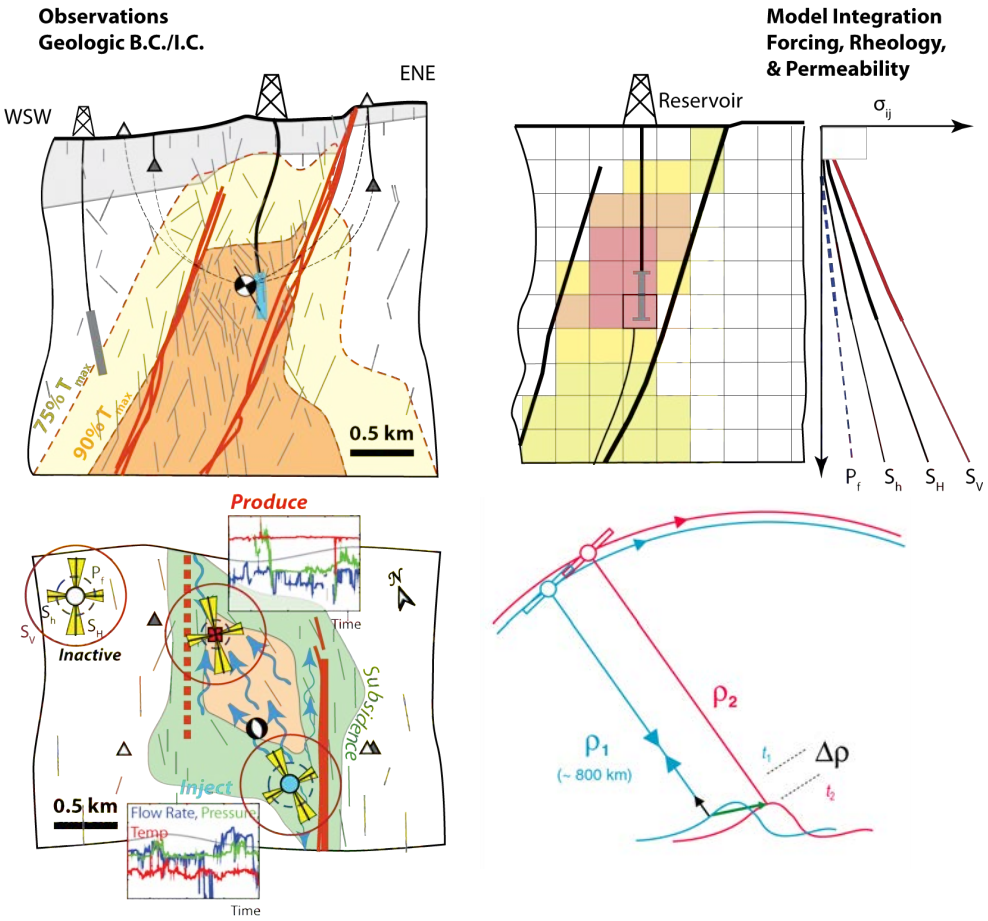

Figure 1.1-1*: Summary of technical approach to investigating the geometry and stressing of a geothermal reservoir using: Upper left: geological constraints; Lower left: geomechanical and pumping data from analysis of wells; Lower right: observations of spatial deformation from phase changes in InSAR; Upper right: geomechanical modeling of the correspondence between deformation responses and the impulse from pumping to infer reservoir shape and properties.*

Technical Approach

We have used InSAR supported by GPS to map the surface deformation resulting from fluid injection and extraction at the Brady's Hot Springs EGS experiment and hence infer the resulting time history of strain and the shape of the stimulated volume at depth using geomechanical modeling and inversion (Figure 1.1-1). We have acquired new SAR scenes since the inception of the project taking advantage of new satellites that provide improved spatial resolution, and combine these with images available since pumping began in 1992 to 2007. We have analyzed these images using innovative techniques to define the history of volume deformations in the subsurface. We have acquired continuously recorded seismic data as well as triggered data to analyze seismicity in the reservoir. We have used new techniques to improve microseismic analysis, including locations and focal mechanisms. These techniques are applied in conjunction with the InSAR analysis and with well injection and flow data to elucidate the relationship of seismicity to stimulation and gain insight into the parameters controlling reservoir productivity (Figure 1.1-1). The results document the evolution and properties of the Brady Reservoir.

The project has developed tools for determining reservoir geometries compatible with surface deformation and the distribution of induced seismicity. The data and steps in the analysis are

assembled into the overall workflow summarized in Figure 1.1-2. External constraints are supplied by the geology, geophysical well logs, and rock mechanics (e.g., Figure 1.1-1) and supplied to the Finite Element (FEM) simulator. The initial conditions and Impulse is supplied by the well data. The simulator can be run for the period of the pumping records, which currently extend back to 2004 in digital format, to pre-condition the model. The model then provides sensitivity analysis according to the reasonable variations in physical properties through a series of forward models. This approach clearly defines the sensitivity of predictions to the model inputs and rheologies, providing the basis for robust uncertainty assessments. The predictions of these forward models are evaluated in terms of the measured responses of surface deformation from InSAR and MEQ activity (e.g., Figure 1.1-1). The monitoring of these responses requires separate workflows in order to supply the constraining responses to the simulator.

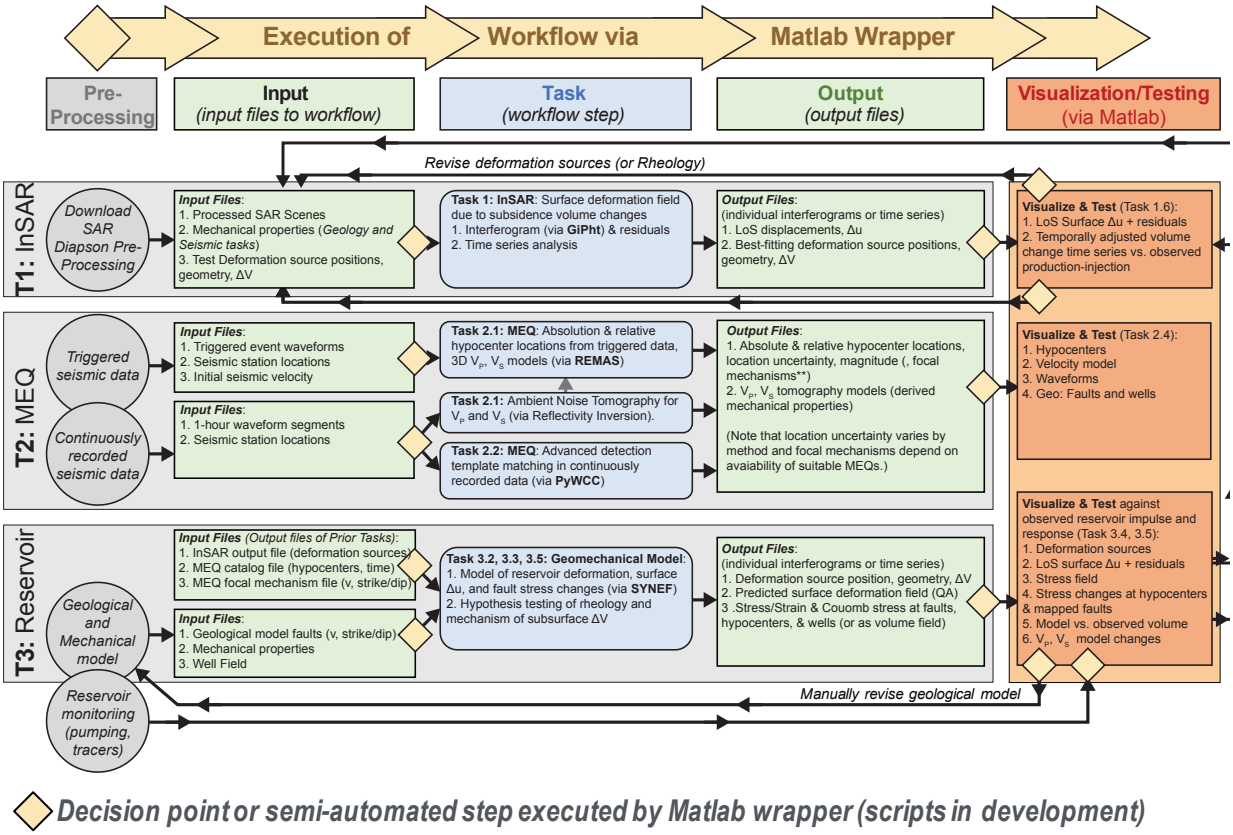

***Figure 1.1-2**: Workflow for passing data into model and for model testing and mapping of model sensitivity into boundary conditions and input parameters. The geomechanical reservoir model is used to integrate data sets into predictions of stress and pressure fields in the reservoir, then conditioned by testing against the responses measured by monitoring of surface deformations and induced micro-seismicity. The resulting output of each task constitutes the input of the next workflow step.*

Structure of this report:

This report serves as a summary of the major results pertinent to project metrics and to relate the products of the research to project milestones.

- **Analysis workflow**: Appendices document the detailed workflows, as modified since submission of the Phase 1 Stage-Gate Report. These details provide a clear definition of

the tasks involved in the analysis so that future work can revise and update the results of this study.

- **Software**: Software tools and supporting data are assembled on a team drive shared with all project members, including the industry partner ORMAT, enabling technology transfer. This ensures all critical materials can be accessed from a single, integrated location. Where possible, software tools are also published to distribution sites such as GitHub to make them widely available (eg., PyWCC and GiPhT), or other sites (e.g., DefMod, https://bitbucket.org/stali/defmod/src/master/). The seismological analysis incorporates a large number of open-source tools; instructions for obtaining these tools is detailed in the workflow. These tools are ready to use, but continue to require expert users to complete analysis updates as might be done on a consulting basis.
- **Data**: In addition, non-proprietary data is published to the Geothermal Data Repository (https://gdr.openei.org/search?q=Brady) in collaboration with the synergistic Brady EGS (DE-FG36-08GO18200) and PoroTomo (DE- EE0006760) projects. More extensive data sets are distributed to purpose-made data repositories (e.g., Winsar, the DOE) as described in the *Task Workflows* (See Appendices). PI Davatzes has also maintained an integrated data exchange with ORMAT via Co-I John Akerley (who took over as the representative of ORMAT from Peter Drakos), which has been incorporated in the Brady EGS final report.
- **Scientific Results**: Major scientific findings are summarized here as they relate to each project Milestone, but the reader is referred to published works for detailed technical documentation.

1.2 Milestones

In this project, we have successfully developed systematic analyses that improve the definition of the reservoir by investigating reservoir responses to pumping such as surface deformation and induced seismicity. Key advances include a clear relationship between injection pressures and seismicity, an unparalleled set of images detailing surface deformation with models of the geometry of the underlying reservoir and water-budget, low-cost measurements of the seismic velocity structure using either seismic interferometry or tomography, and assessment of the mechanisms of deformation governing volume changes in the reservoir. We have also implemented a template matching approach to detect small magnitude earthquakes (PyWCC) as well as identified long-duration, low frequency seismic noise related to reservoir activity.

1.2.1 Summary of Project Accomplishments

The project operated in two distinct Phases. The first phase develops the technology to constrain reservoir parameters from surface deformation, seismicity, and geologically sound boundary conditions. The second Phase formalizes the steps and supporting software tools developed in Phase 1 into a prototype toolbox allowing updates of the reservoir model.

Summarized below are the milestones for each Task related to (1) "Technical Metrics" that involve developing the workflow and software tools that allow analysis and integration of key data sets and (2) "Scientific Metrics" that represent the data products derived from these analysis steps. These Milestones are summarized immediately below. In appendices, we document the finalized workflows developed to analyze and integrate each data set. Similarly, the major scientific findings are summarized below, but the curious reader is directed toward the results section (section 3) of the Phase 1 Stage-Gate Report and to the peer-reviewed publications cited below.

The workflow, including data, software, and documentation are assembled in a cloud drive shared with all team members, including the industry partner ORMAT, effectively transferring the technology to the operator for continued use. Key elements of the software and data sets are independently available through on-line databases such as GitHub (see links below), software specific sites (e.g., links embedded in the Task 2 workflow) or the Geothermal Data Repository (GDR). Links to public sources of the software, example data sets, and supporting MATLAB® scripts to execute and visualize results of the analysis are provided as appropriate. Publication of data has been coordinated with synergistic projects including the POROTOMO and Brady EGS projects. Key findings are published in peer reviewed journals and are cited below. **As an example of technology transfer, Ali et al (2018) and Liu et al (2018) recently applied several of the approaches developed in this project to Raft River in Idaho and Reinisch et al (2020) applied these techniques to the Coso Geothermal System in California. PI Davatzes has discussed extending these techniques to Blue Mountain, Nevada with representatives of CYRQ Energy.**

1.2.2 Technical Metrics Met

Detailed workflows from the initial capture of raw data through data processing, model development and calibration, and delivery of data products have been developed. These workflows incorporate cutting edge techniques in InSAR and seismology including new tools developed within the scope of this project and also incorporates previously developed cutting edge tools most

of which are available as free ware or open-source software. The software also includes tools to format and pipe data between steps in the workflow.

The workflow includes three modules: (1) A module using the history of the surface displacement field to constrain the geometry and position of subsurface volume changes accompanying pumping (SOPO Task 1); (2) Analysis of seismicity including improved earthquake locations and determination of seismic attributes (SOPO Task 2); (3) Reservoir modeling that assesses the deformation induced in the reservoir and its corresponding impact on stress; these volume changes can be interpreted in terms of the key mechanisms of deformation in the reservoir compatible with the pumping records, surface deformation and seismicity and seismic tomography (SOPO Task 3).

The combined analysis serves to: (a) define the geometry if the reservoir and its volumetric change through time, (b) evaluate natural sources of recharge or fluid loss to the reservoir, (c) define the uncertainty in key model parameters, (c) develop conceptual models of the reservoir, and (d) assess the key physical processes governing the reservoir response to pumping and appropriate for forward modeling reservoir behavior. As implemented, the workflow successfully fulfills the requirement of the project based on software development and integration as detailed in the Task workflows.

The viability of the workflow is demonstrated by its application to the Brady Geothermal field and by the resulting scientific analyses published to meetings and peer reviewed journals. We have incorporated observations of surface deformation, a database of well characteristics, laboratory measured rock properties, a 3D geologic model, pumping records, SAR scenes, and seismicity.

- Existing InSAR data spanning 2004-2014 at Brady have been analyzed using inverse modeling to estimate the rate of volume decrease of the order of ~3 liters/second of a dislocation sink buried in an elastic half space.
- A new 1D seismic velocity model of Vp, Vs, and Qs was derived from ambient noise correlation. In parallel, a fully 3D seismic tomography model has subsequently been derived.
- Significant improvements in earthquake detection and locations are achieved including identification of new long period tremor associated with reservoir management activities.
- Established a clear correlation between pressure cycling in the reservoir and episodic seismicity (illustrated in Cardiff et al., 2018) critical to understanding intermittent seismicity in geothermal reservoirs.
- The improved database suggests that episodic seismicity is largely confined to the reservoir and establishes a clear correlation between pressure cycling in the reservoir and episodic seismicity.
- Data on pressure, temperature, production, and injection at Brady for the time interval 2004-2014 are being analyzed to distinguish between hydro-mechanical and thermo-elastic models. (shared with GDR, PoroTomo, Brady EGS)
- Results have yielded new constraints on the reservoir definition and its water budget (illustrated in Ali et al., 2016)
- GPS data at stations BRDY and BRAD for the time interval from 2009 through 2014 have been collected, archived, and analyzed to yield time series of daily estimates of relative, 3-dimensional position. (GDR, PoroTomo)

- Improved or new software tools including: GiPhT, SYNEF, PyWCC (licensing for scripts/codes is in place for technology transfer. (GitHub, NGDS/GDR, Team Cloud-share)
- Results have yielded new constraints on the reservoir definition and its water budget.
- Establish testable conceptual models of the mechanisms accommodating reservoir volume change (Ali et al., 2016; Reinisch et al., 2018) based on modeling volume changes using simple dislocations sources.

Specific project metrics are defined as Milestones in the SOPO document and the outcomes are briefly summarized here.

Task 1.0 Milestones

- *InSAR scenes from WINSAR archive* (see Subtasks 1.1 and 1.3)
  METRIC: Archived SAR scenes and new TerraSAR-X (TSX) scenes used in the analysis of surface deformations at Brady's are compiled into a database.
  RESULT: 96 archived ERS1, ERS2, Envisat, and ALOS scenes have been retrieved for the period from 1992 to 2010 have been acquired and processed. More than 125 TSX scenes have been purchased and processed from 2011 to present.
  DOCUMENTATION: The tools and workflow enabling these analyses are presented in Section 2.1; results are presented in section 3.1 of the Phase 1 report and published works (see listing below, e.g., Ali et al., 2016). This dataset is available in the GDR/NGDS.

- *Complete InSAR analysis of archived data* (see Subtasks 1.2)
  METRIC: InSAR scenes derived from SAR images are determined and compiled into a database.
  RESULT: Interferograms spanning various time intervals have been generated from acquired SAR scenes documenting surface deformations from 1992 to present. Annualized rates of surface deformation along the line of site of the satellites and associated uncertainties have been calculated.
  DOCUMENTATION: Examples of the completed analysis are presented in Section 3.1 of the Phase 1 Report and in peer reviewed publications listed below. This dataset is available in the GDR/NGDS.

- *Development of software tools to stream-line analysis* (see Subtask 1.6)
  METRIC: Software tools to port SAR data into GIPHT or to import analysis from other SAR analysis software are developed and ready for beta-testing. A workflow is established to lead the beta-user through interferogram generation.
  RESULT: Tools to enable analysis of SAR scenes and determination of surface deformations and corresponding subsurface deformation sources and volume changes using GIPHT have been developed.
  DOCUMENTATION: Details of the tools and workflow are presented in Section 2.1. The program can be downloaded from GitHub: https://github.com/feigl/gipht

Task 2.0 Milestones

- *Catalog of event locations with error estimates* (see Subtasks 2.1 and 2.2)

METRIC: MEQ event locations, relocations, and attributes including errors are compiled into a database.

RESULT: Improved MEQ locations have been determined using several methods to improve the velocity model and using relative relocation techniques.

DOCUMENTATION: Results of these analyses are presented in Section 3.2 of the Phase 1 report. The catalog was submitted to the GDR, and is hosted in the Northern California Earthquake Data Center, and the LBNL Induced Seismicity in EGS website (https://wellbore.lbl.gov/egs/bradys_hot_springs.html, see also: http://www.ncedc.org/egs/catalog-search.html). Davatzes et al. (2013) and Cardif et al. (2017) present these data.

- *Development of software tools to stream-line analysis* (see Subtask 2.4)

  METRIC: Software tools to port data from the different component analyses into the advanced earthquake detection analysis (Subtask 2.2) and focal mechanism calculation (Subtask 2.3) are developed and beta-tested by the science team.

  RESULT: (a) Tools to enable derivation of the velocity model and relocation of earthquakes have been developed. (b) Enhanced detection of micro-earthquakes by template matching (Templeton, 2017, https://www.osti.gov/biblio/1379475-python-waveform-cross-correlation) in triggered and continuous data to augment the catalog have been developed. The use of templates proved useful in identifying characteristic seismic noise using novel means; software and an example data set derived from Brady is available at GitHub. (c) In continuously recorded data, newly identified long period, low frequency events, have been detected; techniques to locate these earthquakes remain uncertain and should be considered for future research. (d) Although investigated, procedures for determining earthquake focal mechanisms and estimated stress drops were not fully developed because the number of earthquakes and aperture of the network was insufficient for these analyses.

  DOCUMENTATION: The tools and workflow enabling these analyses are presented in Section 2.2, including the numerous publicly available weblinks to these resources; these tools and their documentation are compiled on the cloud drive.

Task 3.0 Milestones

- *Complete Geologic and Reservoir Database* (see Subtask 3.1)

  METRIC: This is comprised of a database of the relevant well locations, rock mechanical attributes, pumping records, geologic model

  RESULT: A database has been assembled and visualized including: (1) well locations, (2) rock mechanical properties from testing of core, (3) pumping records from 2004 through 2014 including flow rate, line pressure, downhole pressure, and temperature, and (4) a 3D geologic model of stratigraphic layers and fault geometries.; (5) seismic tomograph; (6) earthquake catalog. MATLAB® scripts for interrogating and visualizing the data set have been supplied to the PoroTomo and Brady EGS projects; complete workflows are implemented and available via the cloud drive. These three projects have published key elements of the data to the NGDS/GDR (https://gdr.openei.org/search?q=brady, see summary of data table below), submission of the remaining data is the responsibility of ORAMT after review.

DOCUMENTATION: The tools and workflow enabling these analyses are presented in Section 2.3. Key findings are presented in four journal articles: Davatzes et al. (2013), Ali et al (2016), Cardiff et al., (2018), Reinisch et al. (2018), and was presented by Davatzes at the Gordon Research Conference for Rock Deformation (2018).

- *Development of software tools to stream-line analysis* (See Subtask 3.5)

  METRIC: Software tools to port seismicity and surface deformations from InSAR are developed beta tested by the science team. The basic codes necessary for Subtasks 3.4 to allow rapid update of models and re-running of model simulations are developed by subject area experts.

  RESULT: Tools to conduct geomechanical modeling of the reservoir have been developed. The model currently implements elastic and poroelastic rheologies. Elastic modeling of subsurface volume changes has turned out to be the most pertinent methodology; results of these analyses are used to assess the relative roles of poroelasticity, thermoelasticity, poroplasticity in the deformation observed at Brady.

  DOCUMENTATION: The tools and workflow enabling these analyses are presented in Section 2.3. Section 3.3 of the Phase 1 report summarizes early results. Key results are published by Ali et al. (2016). Cardiff et al (2018, and Reinisch et al (2018).

Milestone 4.0, submission of the **PHASE 1 Go/No-Go Stage Gate Report**. Completed in 2015.

Milestone 5.0, submission of final report and compilation of the software tools integrating findings of both project phases (this report). Submission of the completed key documentation, data sets and workflows to all team partners as technology transfer via a shared cloud drive.

Data sets: *protected*

Final report, programs, scripts: *protected*

Summary of Major scientific findings:

Crustal permeability can be strongly influenced by developing connected networks of open fractures. However, the detailed evolution of a fracture network, its extent, and the persistence of fracture porosity are difficult to analyze. Even in fault-hosted geothermal systems, where heat is brought to the surface from depth along a fault, hydrothermal flow is heterogeneously distributed. This is presumably due to variations in fracture density, connectivity, and attitude, as well as variations in fracture permeability caused by sealing of fractures by precipitated cements or compaction.

At the Brady Geothermal field in Nevada, we investigated the relationship between the modeled local stress state and the location of successful geothermal wells, hydrothermal activity, and seismicity. The local stress state is inferred from a geomechanical model locally perturbed by dislocations representing fault slip or volume changes in the geothermal reservoir constrained by surface deformation measured by InSAR. Permeability is favored in volumes that experience positive Coulomb stress changes and reduced compression, which together promote high densities

of dilatant fractures. Conversely, permeability can be inhibited in locations where Coulomb stress is reduced, compression promotes compaction, or where the faults are poorly oriented in the stress field and consequently slip infrequently. We integrate: (1) direct observations of stress state and fractures in boreholes and the mapped geometry of the fault network; (2) evidence of permeability from surface hydrothermal features, production/injection wells and surface deformations related to pumping history; and (3) seismicity to test the correlation between the reservoir geometry and models of the local stress state.

Our results indicate that over geologic time scales spanning the development of the fault system, these local stress states are strongly influenced by the geometry of the fault network relative to the remote stress driving slip (e.g., Laboso and Davatzes, 2016; Laboso 2016). Whereas at shorter time scales, changes in fluid pressure and thermal contraction within the fracture network constituting the reservoir cause elastic dilations and contractions (e.g., Ali et al., 2016; Cardiff et al., 2018; Reinisch et al., 2018).

1.2.3 Challenges

- *The EGS stimulation timeline of well 15-12ST1 was significantly delayed early in the project.* This required adjustment of the project timeline and rate of spending, but allowed acquisition of additional seismic and SAR data prior to stimulation and thus improved the characterization of the pre-stimulation conditions. This represents an minor increase in project scope conducted within the existing project budget.
- *During stimulation, no detectable seismicity was induced* despite significant flows and downhole pressures, nor was a connection to the reservoir established. In one sense this is in line with the goals of the project to provide alternative constraints, but nevertheless hampered the goal of using *multiple* constraints to resolve reservoir characteristics. However, this project was able to detect longer-term trends in reservoir behavior, including (a) month-scale volume changes attributed to thermal contraction (Ali et al., 2016; Reinisch et al., 2018); (b) daily to weekly responses to production activity associated with seismicity (Cardiff et al., 2018).
- *Low seismicity rates hampered initial analysis of seismicity, and only recently after a new swarm of seismic events has sufficient seismicity occurred to support robust analysis.*
- *Focal Mechanism analysis*: Focal mechanisms constrain the attitude of fault slip in an earthquake. This allows the stress induced by reservoir deformation to be resolved on the fault to determine if the deformation enhanced or inhibited slip tendency. Although tools have been developed to examine focal mechanisms at Brady and tested on synthetics, the limited aperture of the network combined with very low magnitude and a small number earthquakes prevents robust testing. As a result, this task is not included in the workflow.
- *The velocity model initially in use by LBNL to locate triggered seismicity at Brady was determined to be inadequate for the project, requiring derivation of a new model.* However, the low rate of seismicity and distribution of seismicity relative to the seismic network was inadequate to derive a robust velocity model. To address this issue, a new velocity model was derived from ambient noise to constraint earthquake locations since the original velocity model for the field was determined. This involved both the acquisition and processing of continuously recorded seismic data, both of which were beyond the original project scope. This represents an increase in project scope conducted within the existing project budget.

- *New low-frequency, long period seismic tremor associated with reservoir activities was detected in continuously recorded seismic data.* An effort has been made to investigate this behavior as it might provide additional constraints on reservoir properties. This represents an increase in project scope conducted within the existing project budget.
- *The* NGDS/GDR *was not able to accommodate complex data formats generated by this project.* For instance, although PDFs of interferograms can be generated, they lack quantitative information that would be useful to support research activities or implementation in the workflows developed by this project. However, quantitative data formats bundling the key metadata and phase changes defining the interferograms were not compatible with the NGDS/GDR data structures that primarily accommodate data table or excel style "deep data" (as opposed to PDFs). To address this discrepancy, we have worked with WINSAR which is set up to specifically archive these data formats and is also publically accessible, and are working to build a link between the NGDS/GDR and WINSAR. A similar approach was taken with regard to seismicity.
- *The majority of surface deformation correlates with relatively shallow structures that interact with the reservoir.* Nevertheless, the data provides very useful constraints on testing rheologic models appropriate to geothermal systems to explain surface deformation via volume changes at depth resulting from pumping. In addition, the data robustly illustrate the role of faults as conduits and barriers, and suggests that the EGS stimulation 15-12 well is in a distinct compartment.
- *The geomechanical reservoir model considered elastic, thermal, and poroelastic components.* The best fit for short-term response is thermal contraction. The effect is calculated, and the corresponding volume change is implemented using elastic dislocations. Dislocation provide a numerically efficient tool for exploring the parameter space resulting in useful geometric detail.

1.3 Results

We have successfully met the objectives of both project Phases to: (1) provide new constraints on the geometry and properties of a geothermal reservoir from seismicity and surface deformation induced by pumping at the Brady Geothermal Field; (2) develop a systematic procedure to support determination and updating of these constraints by defining analysis workflows supported by software tools to implement the workflow steps.

One potential example of a workflow loop using our software tools is to infer the deformation sources at depth from surface deformations detected by InSAR. GiPhT generates synthetic interferograms from the volume change of dislocations at depth; it iteratively compares different dislocation parameters to minimize the squared misfit between the synthetic interferogram and the observed interferogram from paired SAR images. The solution can be based on an independent assessment, or it can be applied using known discretized structures such as the geological fault model at Brady (as demonstrated by Ali et a., 2016; Reinisch et al., 2018).

Once obtained, the same dislocations can be used in SYNEF to calculate the stress change in the adjacent volume. (A similar analysis was performed with Poly3D, providing validation and additional flexibility. Scripts may be used with SYNEF or Poly3D with minor adjustments. Note that use of Poly3D requires permission or licensing from Schulmberger.)Alternatively, the finite element program DEFMOD (http://geoscience.wisc.edu/~stali/defmod/presentation.pdf; Ali, 2015; Meng 2016) could be used to model stress changes in the reservoir. Then the stress field change is compared to the distribution of seismic events in space and time using criteria such as

changes in the maximum coulomb stress or the slip and dilation tendency if the attitude of the structure is independently known.

This example illustrates a unidirectional series of independent analyses where the seismicity provides a test of the reservoir change detected from surface deformation. Looping this process to maximize the correlation between favorable coulomb stress and seismicity defines a loosely coupled, joint inversion. And collecting the results of these iterations defines the sensitivity and uniqueness of the analysis.

Note that this approach focuses on assessing the volume change at depth associated with deformation of the earth's surface regardless of mechanism. Testing these volume changes against the potential of each mechanism is a separate step. Subsidence consistent with volume loss may be associated with thermal contraction, poroelastic responses to fluid pressure reduction, dissolution, or compaction. Uplift consistent with volume gain may be associated with thermal expansion or pore pressure increase.

Brady demonstrates subsidence and volume loss both at the site of cool water injection and production. This volume loss may be explained by either fluid pressure reduction, thermal contraction, or dissolution. Taking into account the known injection rate, injection pressure, injection temperatures and the production temperature and water level, only thermal contraction provides a viable explanation (Ali et al., 2016; Reinisch et al., 2018). The location and timing of volume change indicate the response of the reservoir to the impulse from the production conditions, thus revealing the geometry of the connected reservoir (particularly well-illustrated by Reinisch et al., 2018).

Summary of Data Products

Task	Data Type	Data Product	Format	Archive Site	Comment	Status
1	InSAR	Raw SAR scenes	N/A	TerraSAR-X Archive (German Space Agency (DLR))	Raw data available for purchase ALOS data is available through WinSAR	Routinely Acquired through joint InSAR & MEQ + PoroTomo
1	InSAR	Line-of-Site surface displacement model	PDF	NGDS/GDR	Image files of InSAR scene time series as individual pairs	Published by Ali et al., 2016 and to GDR
1	InSAR	Line-of-Site surface displacement model	Grid Files	WinSAR	Example scenes in NGDS/GDR	Submited to NGDS/GDR by Feigl, PoroTomo
2	MEQ	Waveform Data: (1) triggered; (2) continuously recorded		LBL, NCEDC, NGDS/GDR	Final destination for these data products is in review by the team	Submited to NGDS/GDR by Feigl, PoroTomo
2	MEQ	Velocity Model 1D ANT model	Excel	NGDS/GDR	Raw waveform data is housed at LBNL, LLNL	Published to NGDS/GDR by Foxall
2	MEQ	Velocity Model 3D Vs from relocated earthquakes	Excel	NGDS/GDR	Raw waveform data is housed at LBNL, LLNL	Published to NGDS/GDR by Foxall
2	MEQ	Velocity Model	Excel	NGDS/GDR	Raw waveform data is housed at LBNL, LLNL	Published to GDR by Foxall

		3D Vp from relocated earthquakes				
2	MEQ	Catalog of Locations (triggered)	Excel	NGDS/GDR		Maintained by Berkely Group
2	MEQ	Catalog of Locations (enhanced)	Excel	NGDS/GDR	Simultaneous tomography and relocation: 2010-2015	Published to NGDS/GDR by Foxall
3	Pumping Records	Flow, Temp, Fluids	Excel	NGDS/GDR		Published to NGDS/GDR via PoroTomo synergistic project
3	Well Specs	Borehole location, deviation, open-hole	Excel	NGDS/GDR	Supports pumping records	Synergy with Brady EGS + PoroTomo
3	Borehole Geom.	Borehole image logs + analysis; constraints on remote stress tensor	PDF, ascii	ORMAT	Final Brady EGS reporting	Compiled in collaboration with Geothermex; Submitted in EGS final report
3	Geologic Model database	Fault and lithologic horizons	Excel	NGDS/GDR	Multiple geologic models developed by: E. Jolie and D. Siler working with ORMAT, Jim Faulds, Nick Hintz, and Inga Moeck	One version published in Egbert Jolie thesis.

Note that data products have been developed and submitted in coordination with the Brady EGS Project (ORMAT), the LBNL project to monitor seismicity at EGS experiments, and the PoroTomo Project (U. of Wisconsin). Minimum time period for final data products corresponds to 2010.5 to 2015.5. These data are readily available to the Team including the Industry Partner at ***Data sets:*** *https://drive.google.com/drive/folders/0BxjLnbxEAnM5VHNVdDd2M01NU2s?usp=sharing*

Final report, programs, scripts: *https://drive.google.com/drive/folders/1lgZvzTIboyA9_-H38WSK0aKrbXCEbvM8?usp=sharing .GDR = Geothermal Data repository, NGDS = National Geothermal Data System; NCEC = Northern California Earthquake Center; LBNL = Lawarence Berkeley National Lab; LLNL = Lawrence Livermore National Lab. Rather than using hardlinks, data sets in the NGDS/GDR are best located via keyword search.*

Published and Key Presentations (articles in review are not listed)

- Feigl (2020) PoroTomo Final Technical Report: Poroelastic Tomography by Adjoint Inverse Modeling of Data from Seismology, Geosdsy, and Hydrology; DE-EE0006760. 174 p. (Synergistic project with shared data and publication of data to GDR/NGDS)
- Ali, Syed T; Reinisch, Elena C; Moore, Joseph; Plummer, Mitchell; Warren, Ian; Davatzes, Nicholas C; Feigl, Kurt L (2018) Geodetic measurements and numerical models of transient deformation at Raft River geothermal field, Idaho, USA ISSN: 0375-6505 , 1879-3576; DOI: 10.1016/j.geothermics.2018.02.007, Geothermics , 2018, Vol.74, p.106-111
- Davatzes, NC (2018) What can heterogeneity in the brittle crust tell us about fracturing and fluid flow? Gordon Research Conference on Rock Deformation: Integrated Approaches to Rock Deformation: Observations, Experiments, and Models. August, 9-24, 2018, Proctor Academy, Andover, NH.
- Davatzes, NC, R.C. Laboso, C.E.Layland-Bachmann, K. Feigl, W. Foxall, A.R. Ali, R.J.

Mellors, D.C. Templeton, J. Akerley, (2017), T14C-05: Are Geothermal Systems Stressed Out? In T14C In Situ Stress: Observations, Uncertainties, and Modeling, Monday, 11 December 2017, 7:00 - 17:15; New Orleans Ernest N. Morial Convention Center - Poster Hall D-F in Fall Meeting American Geophysical Union, edited, New Orleans. https://agu.confex.com/agu/fm17/meetingapp.cgi/Paper/295699

- Reinisch, EC, M Cardiff, KL Feigl (2018) Characterizing volumetric strain at Brady Hot Springs, Nevada, USA using geodetic data, numerical models and prior information, Geophysical Journal International, p. 1501-1513
- M. Cardiff, D.D. Lim, J.R. Patterson, J. Akerley, Paul Spielman, J. Lopeman; P. Walsh; A. Singh; W. Foxall; Herbert F Wang, N.E. Lord, C.H. Thurber, Dante Fratta, R.J. Mellors, **N.C. Davatzes**, K.L. Feigl (2018) Geothermal production and reduced seismicity: Correlation and proposed mechanism. Earth and Planetary Science Letters, v 482, p. 470-477.
- Reinisch, E. C., K. L. Feigl, M. A. Cardiff, C. Morency, C. Kreemer, J. Akerley, and PoroTomo_Team (2017), NH31B-0232: Characterizing Volumetric Strain at Brady Hot Springs, Nevada, USA Using Geodetic Data, Numerical Models, and Prior Information Wednesday, 13 December 2017, 08:00 - 12:20; New Orleans Ernest N. Morial Convention Center - Poster Hall D-F in Fall Meeting American Geophysical Union, edited, New Orleans. https://agu.confex.com/agu/fm17/meetingapp.cgi/Paper/233618
- Cardiff, MA, KL Feigl, X Zeng, NE Lord, C Lancelle, L Parker, EC Reinisch, D Lim, ST Ali, D Fratta, CH Thurber, HF Wang, M Robertson, J Lopeman, C Kreemer, C Morency, **NC Davatzes**, P Team, T Coleman, DE Miller (2016) Overview and Preliminary Results from the PoroTomo project at Brady Hot Springs, Nevada: Poroelastic Tomography by Adjoint Inverse Modeling of Data from Seismology, Geodesy, and Hydrology. AGU Fall Meeting Abstracts, San Francisco, CA, December.
- Laboso, R.C. (2016) Spatial Heterogeneity of Permeability as Influenced by Stress States and Fault Slip, M.Sc. Thesis, Temple University, Philadelphia, 227 p.
- Laboso, R.C., **N.C. Davatzes** (2016), Fault-Controlled Damage and Permeability at the Brady Geothermal System, Nevada, USA, Proceedings, 41st Workshop on Geothermal Reservoir Engineering, Stanford University, Stanford, California, February 22-24, 16p.
- Ali, ST, EC Reinisch, KL Feigl, **NC Davatzes** (2016) Geodetic Measurements and Numerical Models of Deformation at Coso Geothermal Field, California, USA. American Geophysical Union Fall Meeting Abstracts, San Francisco, CA, December.
- Ali, S.T., J. Akerley, A. Baluyut, E.M. Cardiff, **N.C. Davatzes**, K.L. Feigl, W. Foxall, D. Fratta, R.J. Mellors , P. Spielman , H.F. Wang, E .Zemach (2016) Time-series analysis of surface deformation at Brady Hot Springs geothermal field (Nevada) using Interferometric Synthetic Aperture Radar, *Geothermics.* V. 61, p. 114-120.
- Feigl, K.L., The PoroTomo Team, including M.A. Cardiff, X. Zeng, N.E. Lord, C. Lancelle, D.D. Lim, L. Parker, E.C. Reinisch, S.T. Ali, D. Fratta, C.H. Thurber, H.F. Wang, M. Robertson, T. Coleman, D.E. Miller, J. Lopeman, P. Spielman, J. Akerley, C. Kreemer, C. Morency, E. Matzel, W. Trainor-Guitton, S. Jreij, **N.C. Davatzes** (2016) Overview and Preliminary Results from the PoroTomo project at Brady Hot Springs, Nevada: Poroelastic Tomography by Adjoint Inverse Modeling of Data from Seismology, Geodesy, and Hydrology. PROCEEDINGS, 42nd Workshop on Geothermal Reservoir Engineering Stanford University, Stanford, California, February 13-15, 2017 SGP-TR-212. 15 p.
- Ali, S.T., J. Akerley, E.C. Baluyut, **N.C. Davatzes**, J. Lopeman, J Moore, M. Plummer, P.

Spielman, I. Warren, and K.L. Feigl (2016), Geodetic Measurements and Numerical Models of Deformation: Examples from Geothermal Fields in the Western United States Proceedings, 41st Workshop on Geothermal Reservoir Engineering, Stanford University, Stanford, California, February 22-24, 7 p.

- Ali, S.: Defmod – Finite element code for modeling crustal deformation, 2015.
- Feigl, K.L., S.T. Ali, J. Akerley, E. Baluyut, M. Cardiff, **N.C. Davatzes**, William Foxall, Dante Fratta, Corné Kreemer, R. J. Mellors, C. E. Morency, J. Lopeman, P. Spielman, H. F. Wang (2015) Time-Dependent Deformation at Brady Hot Springs Geothermal Field (Nevada) Measured With Interferometric Synthetic Aperture Radar and Modeled with the Finite Element Method, American Geophysical Union National Meeting, San Francisco, CA, December 14-18, 2015.
- Ali, S. T., N. C. Davatzes, K. L. Feigl, H. F. Wang, W. Foxall, R. J. Mellors, J. Akerley, E. Zemach, and P. Spielman (2015), Deformation at Brady Hot Springs geothermal field measured by time series analysis of InSAR data [SGP-TR-204], paper presented at Proceedings, Fortieth Workshop on Geothermal Reservoir Engineering, Stanford University, January 26-28, 2015. https://pangea.stanford.edu/ERE/db/GeoConf/papers/SGW/2015/Ali.pdf
- Davatzes, N.C., Drakos, P., Feigl, K., Foxall, W., Kreemer, C., Mellors, R., Wang,H., Zemach, E., (2014) InSAR measurements and numerical models of deformation at Brady Hot Springs geothermal field (Nevada), 1995-2012. Proceedings, Thirty-Ninth Workshop on Geothermal Reservoir Engineering, Stanford University, Stanford, California, February 2-26, 2014, 14 p.
- Ali et al., InSAR measurements and numerical models of deformation at Brady Hot Springs geothermal field (Nevada), 1997-2012, In Proc. 39th Workshop on Geothermal Reservoir Engineering, Stanford University, Calif., 24-26 Feb, 2014.
- Ali, S. T., J. Akerley, N. Davatzes, K. Feigl, W. Foxall, R. Mellors, P. Spielman, H. F. Wang, and E. Zemach (2014), Deformation at Brady Hot Springs (Nevada) geothermal field measured by time series analysis of InSAR data (Abstract #41A-0468), AGU Fall Meeting.
- Ali, T., Davatzes, N.C., Mellors, R.J., Foxall, W., Drakos, P., Zemach, E., Kreemer, C., Wang, H.F., Feigl, K.L. (2013) InSAR measurements and numerical models of deformation at Brady Hot Springs geothermal Field (Nevada), 1995-2012. American Geophysical Union Annual Meeting Abstracts with Programs, San Francisco, California, USA. December 9-13.
- Ali, S. T., N. C. Davatzes, R. J. Mellors, W. Foxall, P. S. Drakos, E. Zemach, C. W. Kreemer, H. F. Wang, and K. L. Feigl (2013), InSAR measurements and numerical models of deformation at Brady Hot Springs geothermal field (Nevada), 1995-2012 (abstract #G33DA-05), paper presented at Fall Meeting Amer. Geophys. Un., San Francisco.
- Davatzes, N.C., Ali, T., Mellors, R.J., Foxall, W., Wang, H.F., Feigl, K.L., Drakos, P., Zemach, E. (2013) Contrasts between deformation accommodated by induced seismic and aseismic processes revealed by combined monitoring of seismicity and surface deformations: Brady Geothermal Field, Nevada, USA. American Geophysical Union Annual Meeting Abstracts with Programs, San Francisco, California, USA. December 9-13.
- Davatzes, N.C., Feigl, K.L., Mellors, R.J., Foxall, W., Wang. H.F., and Drakos, P. (2013) Contrasts between deformation accommodated by induced seismic and aseismic processes revealed by combined monitoring of seismicity and surface deformations: Brady's Geothermal Field, Nevada. Geothermal Engineering Integrating Mitigation of Induced Seismicity in Reservoirs (GEISER). *Sala del Capitolo, Convento di San Domenico*

Maggiore, Napoli, May 30-31, 2013.

References

(all sections, excluding references to project papers separately listed above)

Beyreuther, M., R. Barsch, L. Krischer, T. Megies, Y. Behr, and J. Wassermann, ObsPy: A Python Toolbox for Seismology, *Seismol. Res. Let*., May/June, 2010.,doi: 10.1785/gssrl.81.3.530

Cardiff, M. A., Kitanidis, P., 2008d. Effcient solution of nonlinear, underdetermined inverse problems with a generalized pde model. Computers and Geosciences 34, 1480-1491.

Cardiff, M.A. (2010) Data Integration and Inverse Methods for Characterization of Multicomponent Hydrologic Systems, Ph.D. Dissertation, Stanford University, 76 p.

Coolbaugh, M.F., Sladek, C., Kratt, C, and Edmondo, G. (2004) Digital Mapping of Strucrurally Controlled geothermal Features with GPS Units and Pocket Computers: Geothermal Resources Council Transactions, v. 28, p. 321-326.

Crotwell, H. P., T. J. Owens, and J. Ritsema, The TauP Toolkit: Flexible seismic travel-time and ray-path utilities, *Seismol. Res. Let.*, 70, 154–160, 1999.

Das, I and M. Zoback, Long-period, long-duration during hydraulic stimulation of shale tight-gas reservoirs – Part 1: Waveform characteristics, *Geophysics*, 78, KS107-KS118, 2013.

Davatzes, N.C., Hickman, S.H. (2009). Fractures, Stress and Fluid Flow Prior to Stimulation of Well 27-15, Desert Peak, Nevada, EGS Project. PROCEEDINGS: Thirty-Fourth Workshop on Geothermal Reservoir Engineering, Stanford University, Stanford, California, February 9-11, 2009.

Faulds, J. E., Hinz, N. H., Coolbaugh, M. F., Cashman, P. H., Kratt, C., Dering, G., Edwards, J., Mayhew, B., and McLachlan, H. (2011). Assessment of favorable structural settings of geothermal systems in the Great Basin, Western USA. Geothermal Resources Council Transactions, 35:777-783.

Faulds, J.E., and Garside, L.J., 2003, Preliminary Geologic Map of the Desert Peak – Brady Geothermal Fields, Churchill County, Nevada: Nevada Bureau of Mines and Geology, Open-File Report 03-27.

Faulds, J.E., Coolbaugh, M.F., Benoit, D., Oppliger, G., Perkins, M., Moeck, I., and Drakos, P. (2010) Structural Controls of Geothermal Activity in the Northern Hot Springs Mountains, Western Nevada: The Tale of three Geothermal Systems (Brady's, Desert Peak, and Desert Queen): Geothermal Resources Council Transactions, v. 24, p. 675-683.

Feigl, K. L. and Thurber, C. H. (2009). A method for modelling radar interferograms without phase unwrapping: application to the M 5 Fawnskin, California earthquake of 1992 December 4. *Geophysical Journal International*, 176(2):491–504.

Harris., D and D. Dodge, An autonomous system for grouping events in a developing aftershock sequence, *Bull. Seism. Soc. Am.*, 101 (2011), pp. 763–774, http://dx.doi.org/10.1785/0120100103.

Hickman, S.H., Davatzes, N.C. (2010). In-Situ Stress and Fracture Characterization for Planning of an EGS Stimulation in the Desert Peak Geothermal Field, Nevada. PROCEEDINGS: Thirty-Fifth Workshop on Geothermal Reservoir Engineering, Stanford University, Stanford, California, February 1-3, 2010.

Hutchings L., S. Jarpe, K. Boyle, G. Viegas, and E. Majer, Inexpensive, automated micro-earthquake data collection and processing system for rapid, high-resolution reservoir analysis. Trans. Geothermal Res. Council 2011 Annual Meeting, San Diego, CA.

Hutchings, L., A. Singh, B. Bonner, S. Jarpe, H. Philson, and K. Boyle, Micro-earthquake analysis for reservoir properties for injection wells at The Geysers, California geothermal field, submitted *J. Geophys. Res*., 2015.

Jolie, E., Faulds, J., and Moeck, I. (2012). The development of a 3D structural-geological model as part of the geothermal exploration strategy - a case study from the Brady's geothermal system, Nevada, USA. In Proc. 37th Workshop on Geothermal Reservoir Engineering (Stanford University, CA) .

Jolie, E. (2014) Detection and Characterization of Permeable Fault Zones by Surface Methods in the Basin and Range Province, USA [Dissertation]: der Technischen Universität Berlin, 132 p.

Lutz, S.J., Hickman, S., Davatzes, N., Zemach, E., Drakos, P., Robertson-Tait, A. (2010). Rock Mechanical Testing and Petrologic Analysis in Support of Well Stimulation Activities at the Desert Peak Geothermal Field, Nevada. PROCEEDINGS: Thirty-Fifth Workshop on Geothermal Reservoir Engineering, Stanford University, Stanford, California, February 1-3, 2010.

Lutz, S.J., Zutshi, A., Robertson-Tait, A., Drakos, P., and Ezra, Z. (2011) Lithologies, Hydrothermal Alteration, and Rock Mechanical Properties in Wells 15-12 and BCH-3, Brady's Hot Springs Geothermal Field, Nevada: GRC Transactions, v. 35, p. 469-476.

Massonnet, D. and Feigl, K. L. (1995). Discrimination of geophysical phenomena in satellite radar interferograms. *Geophysical Research Letters*, 22(12):1537–1540.

Massonnet, D. and Feigl, K. L. (1998). Radar interferometry and its application to changes in the earth's surface. *Reviews of Geophysics*, 36(4):441–500.

Massonnet, D. and Rabaute, T. (1993). Radar interferometry: limits and potential. *Geoscience and Remote Sensing, IEEE Transactions on*, 31(2):455–464.

Meng, C. (2016) Benchmarking Defmod, an open source FEM code for modeling episodic fault rupture, Computers & Geosciences, 100, 10 – 26, https://doi.org/https://doi.org/10.1016/j.jngse.2016.02.058, DOI: 10.1016/j.cageo.2016.11.014

Mogi, K., 1958, Relations between the eruptions of various volcanoes and the deformations of the ground surfaces around them: Bull. Earth. Res. Inst., v. 36, p. 99–134.

Morris, J., Y. Hao, W. Foxall, and W. McNab, 2011. A study of injection-induced mechanical deformation at the In Salah CO_2 storage project. *Int. J. Greenhouse Gas Control*, ***s***, 270-280.

Myers, S.C., G. Johannesson, and W. Hanley, A Bayesian hierarchical method for multiple-event seismic location, *Geophys. J. Int.*, **171**, 1049-1063, 2007.

Myers, S.C., G. Johannesson, and W. Hanley, Incorporation of probabilistic seismic phase labels into a Bayesian multiple-event seismic locator, *Geophys. J. Int.*, **177**, 193–204, 2009.

Okada, Y. (1985). Surface deformation due to shear and tensile faults in a half-space. *Bulletin of the Seismological Society of America*, 75(4):1135–1154.

Okada, Y. (1992) Internal deformation due to shear and tensile faults in a half-space, *Bulletin of the Seismological Society of America*, v. 82, p. 1018-1040.

Ramirez, A., and W. Foxall, 2014. Stochastic inversion of InSAR data to assess the probability of pressure penetration into the lower caprock at In Salah. *Int. Jo. Greenhouse Gas Control,* **27**, 42-58.

Reimisch, E.C. (2016) Graph Theory for Analyzing Pair-Wise Data: Applications to Interferometric Synthetic Apertre Radar Data, MS thesis, University of Wisconsin, Madison, 90 p.) https://gdr.openei.org/files/1075/ReinischEC_MS_thesis_20160728.pdf

Thurber, C., Earthquake locations and three-dimensional crustal structure in the Coyote Lake area, central California, *J. Geophys. Res.*, *88,* 8226-8236, 1983.

Waldhauser F. and W.L. Ellsworth, A double-difference earthquake location algorithm: Method and application to the northern Hayward fault, *Bull. Seism. Soc. Am.*, **90**, 1353-1368, 2000.

Waldhauser, F., HypoDD: A computer program to compute double-difference earthquake locations, *USGS Open File Rep.,* 01-113, 2001.

Zhang, H. and C. Thurber, Double difference tomography: Method and application to the Hayward fault, California, *Bull. Seismol. Soc. Am.*, 93, 1875, 2003.

APPENDICES

APPENDIX - SOPO

APPENDIX – Analysis Workflows

The primary goal of this study is to develop tools to better constrain reservoir properties and how these properties evolve through time. Constraints are derived from surface deformation (Task 1), seismicity (Task 2), and incorporated into a geomechanical model of a reservoir (Task 3). Conducting each of these analyses requires a series of steps beginning with acquisition of the raw data and transformation of this data into products that constrain the reservoir model (Figure 1.1-2).

For each of the three major tasks, the SOPO defines subtasks to address the key technical issues enabling the analysis. In addition, a separate subtask is defined to assemble these technical steps into an integrated workflow. This section presents the workflow that corresponds to each major task, and clearly identifies: (1) the tools that enable data analysis, (2) the input and output data associated with each step in the analysis, and (3) how each subtask supports a comprehensive geomechanical model of the reservoir.

APPENDIX B: Updated Section 2.1:

APPENDIX - Summary of Software and Data Resources

APPENDIX - Updated Section 2.1: InSAR Analysis

APPENDIX - Updated Section 2.2: Seismicity

APPENDIX - Updated Section 2.3: Reservoir Modeling

APPENDIX - PyWCC Description

APPENDIX - SOPO

STATEMENT OF PROJECT OBJECTIVES

PI: Nicholas Davatzes, Temple University
Co-PIs: Kurt Feigl[1], Herb Wang[1], Rob Mellors[2], Bill Foxall[2], **Co-I:** Peter Drakos[3]
[1]University of Wisconsin–Madison; [2]Lawrence Livermore National Laboratory, [3]ORMAT

Development of tools for coupled InSAR and Seismicity monitoring of EGS reservoir development and management

A. PROJECT OBJECTIVES

This project will:

- Develop software tools to streamline interferometric synthetic aperture radar (InSAR) measurement of surface deformations
- Develop software tools to streamline advanced analysis of micro-earthquakes (MEQ) and enhance MEQ detection
- Develop software tools for poroelastic modeling of reservoir dynamics to account for the integrated pumping, seismic and InSAR data constraints
- Test the relationship of induced seismicity to pore pressure changes resulting from pumping and stimulation
- Use seismicity and surface deformations to jointly constrain the short- and long-term evolution of the stimulated reservoir.
- Develop a prototype framework to monitor stimulation and reservoir management by combining pumping, seismic, and geodetic data with the poroelastic models

B. PROJECT SCOPE

This project will develop an integrated set of tools to monitor the evolution of permeability and fluid flow within an enhanced geothermal system (EGS) during both the stimulation and production phases. The goal is to infer the location, geometry and pore pressure distribution within the subsurface fracture network. This information can be used to guide decisions regarding injection pressures and flow rates during simulation and production. This will enable optimization of long-term field management and aid in locating additional wells as the field is developed. First, we will characterize the time history of surface deformations using interferometric synthetic aperture radar (InSAR) and seismicity using advanced processing techniques. Second, the surface deformation and seismicity will be modeled as a response to pumping history using poroelastic modeling.

Subsequently, we will develop software tools to measure, model and integrate innovative analysis of recorded microseismicity with inversion of surface displacement fields measured by InSAR. The toolbox will correlate spatio-temporal development of the fracture network and pore pressure field derived from these analyses with injection and production records by poroelastic modeling of the reservoir response to well pressures and flow rates. This will lead to increasing production efficiencies per well and hence lower the levelized cost of electricity (LCOE).

This project will meet the objectives of the DOE Geothermal Technologies Program and funding announcement DE-FOA-0000522 by:

- Providing rapid development of technology to monitor and guide stimulation during the development of enhanced geothermal systems (EGS)
- Providing tools to enhance the use of seismicity in monitoring stimulation or production activity through better data processing
- Providing tools to define the geometry of the geothermal reservoir and measure fluid pressure fluctuations correlated to pumping activity

- Integrating these tools into a data collection framework facilitating increased efficiency of geothermal energy production and EGS success
- Developing an integrated data set of pumping records, seismicity, and surface deformations associated with fracture-hosted fluid flow prior to, during, and post stimulation

C. TASKS TO BE PERFORMED

PHASE 1

Phase I of the project consists of three components that will be conducted in the first 2 years: (1) acquisition and analysis of InSAR images at Brady's, (2) analysis of seismicity data acquired in the vicinity of Brady's and (3) poroelastic modeling of the correlation between pumping and surface deformations revealed by InSAR and pore pressure changes that can be correlated to seismicity.

Task 1.0 InSAR Analysis

Surface displacements associated with the Brady's geothermal field will be monitored using InSAR. These will act as a constraint on poroelastic modeling (Task 3.0) of subsurface deformation and pressure fluctuations caused by production/injection during both normal reservoir operation and stimulation. The results of Task 1 will be processed of InSAR time series of surface displacements and the corresponding modeled sub-surface deformation, and software tools/workflows to streamline processing and analysis.

Subtask 1.1 Acquire archived SAR data

Archived data (C-band and L-band) covering the Brady's site in various archives, such as the WINSAR archive, will be acquired and processed, and the derived products made available to the research team as a database.

Subtask 1.2 Time series analysis of archived SAR data

Time series analysis of the archived SAR images will be used to derive InSAR scenes that map the evolution of surface deformations at Brady's. This analysis will provide a pre-stimulation deformation history spanning 1992 to 2009 for which corresponding pumping records are available.

Subtask 1.3 Acquire TerraSAR-X images

New SAR scenes will be tasked and collected during the period of the research project. The new generation of satellites (e.g., TerraSAR-X) increases the spatial sampling density to over 10^4 pixels per km^2 and the observation frequency to almost one pass per week.

Subtask 1.4 Time series analysis of TerraSAR-X images

SAR data will be analyzed using DIAPASON, GIPhT, GAMMA and/or GMTSAR. This analysis will measure surface deformations spanning pre-, co-, and post-stimulation timeframes.

Subtask 1.5 Inverse modeling of InSAR data using GIPhT

Surface deformations measured using InSAR are modeled as a response to deformation sources at depth in the reservoir. This analysis will estimate the possible subsurface deformations consistent with observations of surface deformation measured by InSAR.

Subtask 1.6 Tools to streamline InSAR processing

GMTSAR and GIPHT will be adapted so that interferograms produced by GMTSAR can be fed directly into GIPHT for time series analysis and inverse modeling to provide a streamlined workflow from the raw SAR data to estimates of model parameters. This workflow will: (i) generate interferograms between pairs of SAR images, (ii) compare InSAR images from multiple pairs of epochs and estimate model parameters.

Task 1.0 Milestones

- *InSAR scenes from WINSAR archive* (see Subtasks 1.1 and 1.3)
  Archived SAR scenes and new TerraSAR-X scenes used in the analysis of surface deformations at Brady's are compiled into a database.

- *Complete InSAR analysis of archived data* (see Subtasks 1.2)
  InSAR scenes derived from SAR images are determined and compiled into a database.
- *Development of software tools to stream-line analysis* (see Subtask 1.6)
  Software tools to port SAR data into GIPHT or to import analysis from other SAR analysis software are developed and ready for beta-testing. A workflow is established to lead the beta-user through interferogram generation.

Task 2.0 Seismological Analysis

Earthquakes occurring in and around the Brady's geothermal field will be analyzed using advanced processing techniques to improve location accuracy, estimate location error, calculate focal mechanisms, and model earthquake stress drop as inputs into the poroelastic modeling of Task 3.0. This task will result in improved earthquake locations, focal mechanism solutions, earthquake stress drop estimates, and software tools/workflows to streamline analysis.

Subtask 2.1 Acquire seismic data and apply advanced detection methods

Download from LBNL data recorded by the Brady's-Desert Peak seismic network since 2010. Gather and evaluate data from the Nevada Regional seismic network. Apply empirical matched filter analysis on the relevant data subsets to increase the number of events detected.

Subtask 2.2 Locate earthquakes with Bayesloc/hypoDD

Improve location accuracy of microearthquakes (meqs) using the hypoDD and Bayesloc relative location methods along with Bayesian error estimation to create probabilistic estimates of earthquake source locations and location errors. This analysis will be supplemented where possible by improved phase picks from cross-correlation of meq waveforms.

Subtask 2.3 Compute focal mechanisms and stress drops

Analysis of MEQ focal mechanisms/moment tensors will be performed to determine the orientations of fractures undergoing seismic slip with respect to the in-situ stress field. Similarly, earthquake slip vectors and stress drops will be analyzed to infer source and stress field characteristics.

These results will be compared to the predictions of the Coulomb failure criterion, which are initially based on rock strength from laboratory triaxial deformation experiments and a borehole stress model in EGS experiments, as well as independently to the poroelastic stress model (Task 3 below).

Subtask 2.4 Tools to streamline seismological analysis

Integrated software tools will be constructed to automate enhanced earthquake detection, location, source mechanism methods and error estimation techniques.

Task 2.0 Milestones

- *Catalog of event locations with error estimates* (see Subtasks 2.1 and 2.2)
  MEQ event locations, relocations, and attributes including errors are compiled into a database.
- *Development of software tools to stream-line analysis* (see Subtask 2.4)
  Software tools to port data into the different components into the advanced earthquake detection analysis (Subtask 2.2) and focal mechanism calculation (Subtask 2.3) are developed and can be beta-tested by the science team.

Task 3.0 Poroelastic Modeling

Seismicity and deformation are closely related consequences of pumping, so that *joint* analysis of the two data sets will maximize the constraint on the short- and long-term evolution of the stimulated reservoir. In addition, poroelastic modeling provides a bridge between the impulse derived from injection or production of fluid and the response which is the time-delayed microseismicity and deformation observed by InSAR.

Subtask 3.1 Compile database of reservoir properties and impulse-response time series

Previous work at the Brady's site and related operational data site will be assembled into a database accessible to the research team to constrain the modeling efforts. These data includes pumping histories (injection/production volumes, rates, locations, and times), a 3-D stress model, rock mechanical properties, detailed surfaced mapping of structures and a 3-D fault model, borehole measurements of fracture distributions and attitudes, seismic wave speeds, chemical tracers, microseismicity, gravity measurements, electromagnetic self-potential, well logs, temperature profiles, and down-hole samples. These data forms the basis for constructing the poroelastic models.

Subtask 3.2 Forward impulse-response modeling

Poroelastic models of the geothermal field will be constructed incorporating the parameters and constraints aggregated in the database in Subtask 3.1. These models will predict two time-dependent fields: vector displacement and tensor stress that will be compared to surface deformation measurements from InSAR and the distribution and focal mechanisms of seismic events. Through systematic variation of the model parameters we will perform a sensitivity analysis to define the relative impact of different model parameters on the displacement field and stress tensor evolution.

Subtask 3.3 Inverse modeling constrained by InSAR and seismicity

Seismicity and surface deformations will be correlated to injection/production using inverse modeling. The modeling combines an approximate solution to the forward problem with stochastic inversion. The result is a model of the spatial evolution of fluid pressure constrained by the surface deformations and the seismicity.

Subtask 3.4 Tools and workflow to streamline data transfer and model updates

Successful models established in sub-tasks 3.1-3.3 will be modified to produce updatable poroelastic models of pore pressure distribution due to pumping constrained by surface deformations and seismicity. A workflow and tools to readily port the necessary data into the model will be developed. The result of this effort will be a model of fluid flow in the reservoir constrained by the combination of pumping records, surface deformations from InSAR, and MEQs.

Subtask 3.5 Test Coulomb Stress Change against earthquake locations and focal mechanism solutions

The poroelastic models will predict time-dependent changes in the stress field. Thus, with constraints from pumping records, the 3D stress model, and rock strength we will compare predicted failure based on the Coulomb failure criterion with earthquake locations and focal mechanisms.

Task 3.0 Milestones

- *Complete Geologic and Reservoir Database* (see Subtask 3.1)
  This is comprised of a database of the relevant well locations, rock mechanical attributes, pumping records, geologic model
- *Development of software tools to stream-line analysis* (See Subtask 3.5)
  Software tools to port seismicity and surface deformations from InSAR are developed and ready for beta testing by the science team. The basic codes necessary for Subtasks 3.4 to allow rapid update of models and re-running of model simulations are developed.

Task 4.0 Stage Gate Report

A comprehensive report outlining the results of Tasks 1, 2, and 3 in PHASE 1 including the development of key databases and tools. The purpose of this report is to demonstrate the transition from the research phase of the project to the development of a prototype workflow and software that allows monitoring of reservoir dynamics via pumping records, surface deformations, seismicity, and poroelastic modeling.

Task 4.0 Milestones

- *Submit Stage-Gate Review*

PHASE 1 Go-No-Go Decision Point based on the review of the Task 4.0 Stage Gate Report and satisfactory achievement of the Tasks 1, 2, and 3 Milestones.

PHASE 2

Phase II consists of applying the tools to the data set collected from the Brady's EGS experiment to validate the integrated component technologies in a field application. Other tasks include continued data collection and integration into the analysis to date.

Task 1.0 InSAR Analysis - Continued

PHASE I tasks related to InSAR data acquisition and analysis continue in support of PHASE II prototype development.

Subtask 1.3 Acquire TerraSAR-X images

Subtask 1.4 Time series analysis of TerraSAR-X images

Subtask 1.5 Inverse modeling of InSAR data using GIPhT

Task 2.0 Seismological Analysis - Continued

PHASE I tasks related to seismicity data acquisition and analysis continue in support of PHASE II prototype development.

Subtask 2.1 Acquire seismic data and test detection

Subtask 2.4 Tools to streamline seismological analysis

Task 3.0 PoroElastic Modeling - Continued

PHASE I poroelastic modeling continues in support of PHASE II prototype development.

Subtask 3.1 Update database of reservoir properties and impulse-response time series

Subtask 3.3 Inverse modeling constrained by InSAR and seismicity

Subtask 3.4 Tools and workflow to streamline data transfer and model updates

Subtask 3.5 Test Coulomb Stress Change against earthquake locations and focal mechanism solutions

Task 5.0 Develop Prototype

A prototype combining software tools developed for the coupled analysis of InSAR, seismicity and pumping via poroelastic modeling will be incorporated into a workflow for application to monitoring Brady's. This workflow will provide a technology for continued monitoring of the evolving pore pressure distribution by incorporating updated InSAR scenes and seismicity acquired during the PHASE 2 budget period. The workflow and tools form the basis for the application of this technology to other EGS.

Task 5.0 Milestones

- *Complete Prototype* (see Task 5.0)
  A working prototype capable of being updated with new SAR, MEQ, or pumping record data is developed for use by the operator.

Task 6.0 Project Management and Reporting

Reports and other deliverables will be provided in accordance with the Federal Assistance Reporting Checklist following the instructions included therein.

APPENDIX – Summary of Software and Data Resources

Data analysis and visualization

- Geological Model (MATLAB)
- Visualization of impulse-response: pumping records and temperature (MATLAB)
- Construction of fault and deformation source meshes (MATLAB)

Data sets: *protected*

Final report, programs, scripts: *protected*

Matlab Wrappers

- Task 1: Impulse-Response visualization
- Task 2: (data is primarily handled outside of Matlab, all programs available in cloud drive)
- Task 3: Reservoir deformation: (a) SYNEF; (b) Poly3D

Task1: Surface Deformation (Software + example data set)

- GMTSAR:
  - http://topex.ucsd.edu/gmtsar
  - https://github.com/gmtsar/gmtsar/wiki
- GiPhT: https://github.com/feigl/gipht
  - Note that the PoroTomo team has further developed the Matlab toolkint for interfacing with GiPhT. Contact Co-I Feigl for most recent toolkit.

Task2: Micro-seismicity (Software + example data set)

- REMAS, Tomography and double-difference relocation (Jarpe, LBNL): available from LBNL under a licensing agreement, release pending
- IRIS/PASSCAL: http://www.passcal.nmt.edu/ftp/software/passoft
- VTK: http://www.vtk.org
- ANT Analysis: http://www.eas.slu.edu/eqc/eqccps.html.
- Baysloc: https://missions.llnl.gov/nonproliferation/nuclear-explosion-monitoring/bayesloc
- TauP toolkit: http://www.seis.sc.edu/TauP
  - https://wci.llnl.gov/simulation/computer-codes/visit/download
- hypoDD: http://www.ldeo.columbia.edu/~felixw/hypoDD.html
- SimulCR: contact Lawrence Hutchings at Lawrence Berkeley National Lab (software copy and example input/output files are provided in the cloud drive)
- PYWCC, matched field processing (https://github.com/templetond/pywcc.git) (PYTHON)
  - Procedure: https://www.osti.gov/biblio/1379475-python-waveform-cross-correlation
  - Dependencies: Python, ObsPy, numpy, and scipy:
    - install Python (anaconda, free academic license from company, Python 2) + some supporting libraries

        - http://docs.obspy.org/index.html
- GMT (visualization): http://gmt.soest.hawaii.edu/projects/gmt/wiki/Download

Relevant Data

- Brady Triggered Data: *http://fracture.lbl.gov/Bradys/process/evtfiles*.
- Northern California Earthquake Data Center (NCEDC) (http://www.ncedc.org/)
- SAC format files from:*http://fracture.lbl.gov/Bradys/process/sac_files*.

Task3: Reservoir Modeling (Software + example data set)

- DEFMOD (Fortran 95) (Tabrez Alo: https://bitbucket.org/stali/defmod/wiki/Home; subsequently developed software: https://github.com/Chunfang/defmod-swpc) (useful supporting tools git clone https://bitbucket.org/stali/defmod-utils.git)
- SYNEF, Elastic reservoir deformation (LBNL) (FORTRAN): contact Wiliam Foxall at Lawrence Berkeley National Lab (software copy and example input/output files are provided in the cloud drive)
    - fortran compiler g77 —> gfortran: https://gcc.gnu.org/wiki/GFortranBinaries
    - download a .dmg installation package for Mac
    - Note that this is a Fortran 95 compiler, also incorporating several features from the 2005 and 2008 standards. It is also compatible with f77, whic is really a subset of Fortran 95. SYNEF is written in Fortran 95. You will also need to install Xcode and associated Command Line tools from Apple.
- Poly3D, Elastic reservoir deformation (Schlumberger) (C): copy of the academic software matlab toolbox with supporting explanations in Laboso (2016) are provided in the cloud drive (see above)

Accessory freeware to aid visualization:

- ParaView (https://www.paraview.org/)

APPENDIX: Updated Section 2.1: InSAR Analysis

2.1 InSAR (SOPO Task 1)

InSAR reveals surface deformations that result from volume changes at depth in response to pumping activities, thus providing important constraints on reservoir geometry and properties. This section describes SOPO Subtasks 1.1, 1.2 1.3, 1.4, and 1.5 which together comprise the streamlined InSAR analysis (Subtask 1.6).

2.1.1 Workflow Outline

Task 1 constrains reservoir behavior through surface deformations revealed by InSAR. This task results in two critical products: (1) data sets to constrain reservoir deformation including surface displacement fields and estimates of attributes of contracting/expanding volumes at depth and (2) tools to automate that analysis for use in the workflow.

The inference of the sources of volume change at depth from the surface displacement field evident by comparing SAR scenes is conducted via the software GiPhT and is already implemented in Matab® through support from this project and PoroTomo. GIPhT is available at https://github.com/feigl/gipht.

We have submitted the results of a simulation to the GDR at https://gdr.openei.org/submissions/939. These files contain the output of a model calculation to simulate the pressure and temperature of fluid at Brady Hot Springs, Nevada, USA. The calculation couples the hydrologic flow (Darcy's Law) with simple thermodynamics. The epoch of validity is 24 March 2015. Coordinates are UTM Easting, Northing, and Elevation in meters. Temperature is specified in degrees Celsius. Pressure is specified in Pascal.

The workflow begins with acquisition of SAR scenes documenting the surface topography and proceeds to data products supplied to the geomechanical model (Figure 2.1-1). Each step of the workflow involves use of software. URL's for the source code are included in the descriptions. These include implementation of software developed independently of this project, but incorporated into the analysis, as well as newly developed software for data analysis or for passing data between steps.

InSAR analysis:

Step 0: Downloading of SAR data (Subtask 1.1 and 1.3)

Step 1: Processing of SAR data (Subtask 1.2 and 1.4)

Step 2: Inverse modeling of SAR data using simple semi-analytical models (Subtask 1.5)

Step 3: Time series analysis (Subtask 1.2 and 1.4)

Geomechanical analysis:

The InSAR analysis feeds directly into the Geomechanical analysis of the reservoir, which is addressed in Section 2.3 below.

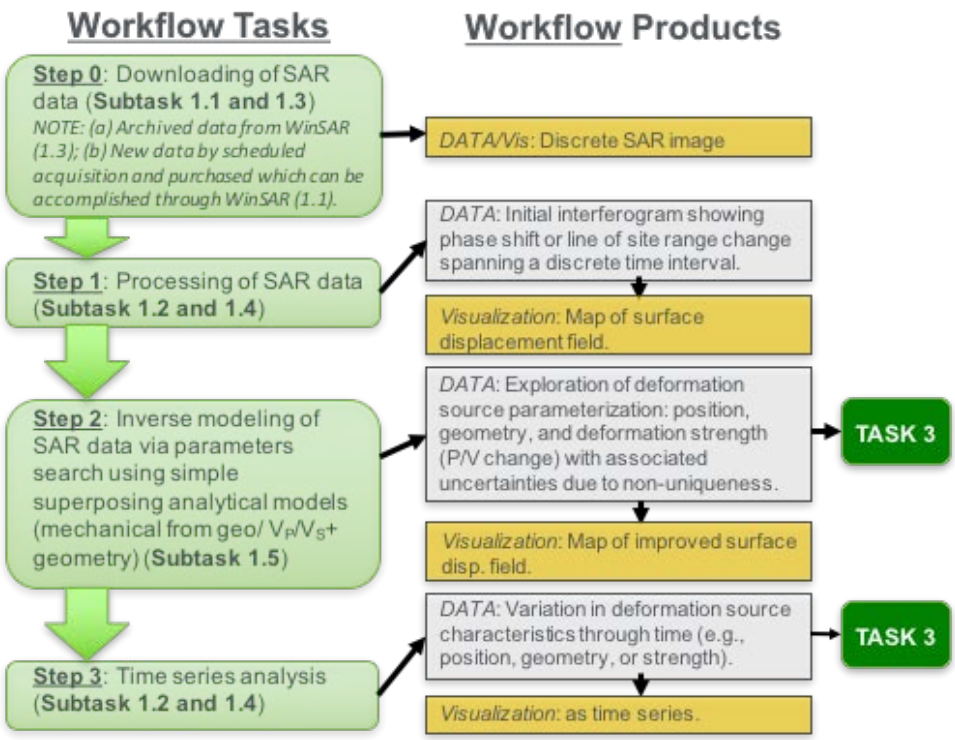

Figure 2.1-1: *Summary of steps in the workflow leading from raw SAR scenes to interpreted interferograms of surface deformations compatible with subsurface volume (or pressure) changes.*

2.1.2 Workflow Description

Step 0 (Subtask 1.1 and 1.3) - Download SAR Data: The synthetic aperture radar (SAR) scenes can be downloaded from UNAVCO's WinSAR facility (https://winsar.unavco.org) using a simple web based tool as shown in the figure below (Figure 2.1-2):

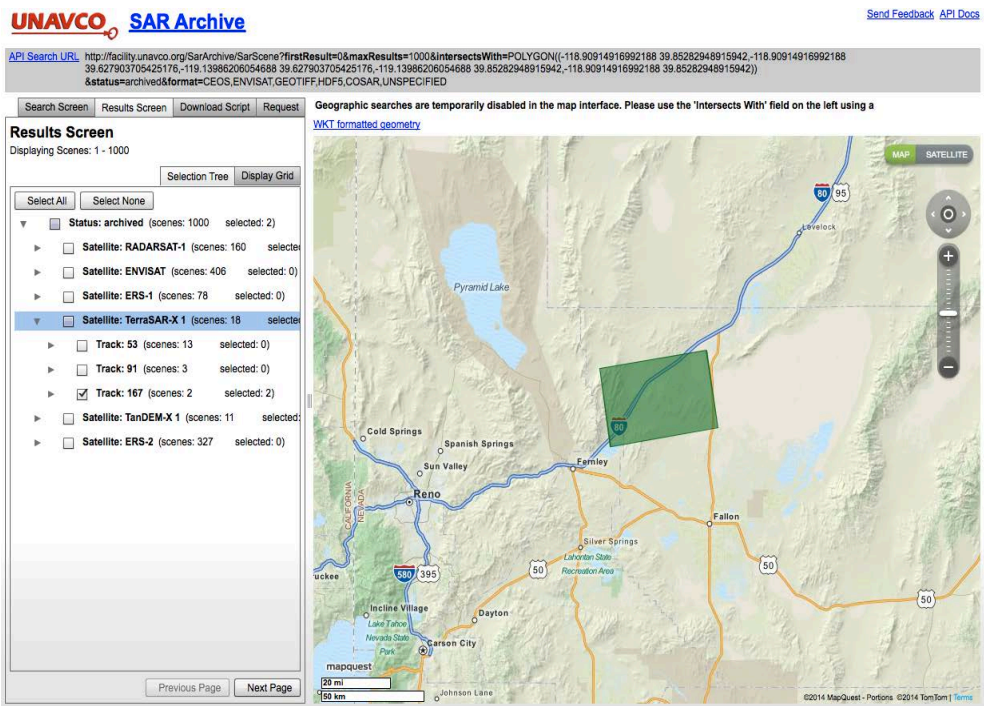

***Figure 2.1-2**: Screenshot of the WinSAR portal for downloading data.*

Note: A user must first register with WinSAR to search and download the data. All ERS/ENVISAT and TSX scenes from this project are archived by WinSAR. ALOS images must be downloaded from NASA's Alaska Satellite Facility (ASF) which has a similar interface as the one shown above. Interferograms can only be made from two scenes that are in the same "Track", have a reasonable overlap in space, a reasonable baseline and were acquired using the same "beam". Both WinSAR and ASF support bulk downloading of images.

Synthetic Aperture Radar data from the TerraSAR-X and the TanDEM-X satellite missions operated by the German Space Agency (DLR) were used under the terms and conditions of Research Project RES1236. In accordance with the FAIR principles (Stall et al., 2017; Stall, 2018), InSAR and GPS data for this work are available publicly on the Geothermal Data Repository (Reinisch, 2017; Kreemer, 2018). Data products derived from InSAR and GPS and used in the analysis presented within this work are available publicly (Reinisch, to be submitted upon acceptance of manuscript, currently hosted at *ftp://roftp.ssec.wisc.edu/porotomo/PoroTomo/DATA/InSARforGDR*). See discussion and application in Reinisch et al, 2020, http://dx.doi.org/10.1029/2019jb017816)

Step 1 (Subtask 1.2 and 1.4) - Processing of radar data and creation of interferograms: Interferograms represent the change in line of sight between a satellite derived from SAR images at two distinct times. Thus they can document the relative movement of the earth's surface within the time period spanned by the two SAR images as a shift in radar phase, which can be converted (unwrapped) to a change in the distance between the satellite and the surface. Extensive discussions are provided in Massonnet and Rabaute (1993), Massonnet and Feigl, (1998), and Feigl, K. L. and Thurber, C. H. (2009). Various tools for this processing are available such as GMTSAR, DIAPSON, and GiPhT).

For processing SAR scenes and creation of interferograms either DIAPASON (code developed by the French Space Agency CNES and available through Altamira) or GMTSAR (freely available

at http://topex.ucsd.edu/gmtsar and built on top of Generic Mapping Tools or GMT) can be used. Both codes can easily be installed on any *NIX machine with standard conforming C/C++/Fortran compilers and are relative simple to use. Familiarity with Unix scripting however is necessary. In addition, GiPhT (Feigl and Thurber, 2009) can also be used to interpret the displacement field directly from the phase shift while avoiding unwrapping.

GMTSAR also comes with a number of example datasets for different satellites (e.g., ERS, ENVISAT and ALOS). A sample data-set, containing two TSX scenes for Brady and the scripts to create and unwrap the interferogram are available from https://temple.box.com/s/q77k156uw0mzwf5jk6lemndjeehaafrl. Detailed instructions are available in the README file.

After processing and unwrapping the beta user should be able to plot the phase and range change as shown in Figure 2.1-3, left and center panels, respectively using GMT. The values, plotted in latitude-longitude coordinate system can be easily converted to UTM coordinates programs available in GMT. Descriptions of the SAR data at the Brady's site including metadata (e.g., dates, look angle, geographic coverage) have been uploaded into the Geothermal Data Repository.

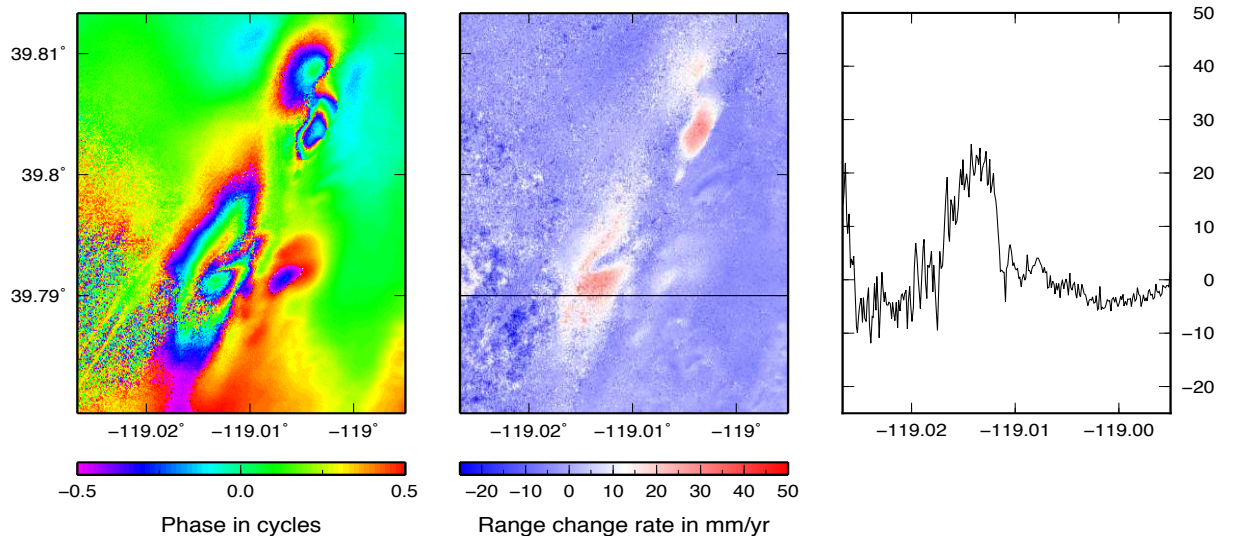

Figure 2.1-3*: Left: TSX interferogram from Track 53, spanning 352 days, between 26th Jan 2012 and 12th Jan 2013, showing phase values in cycles (1 cycle = 15.5 mm). Center: Rate of range change in mm/year calculated by 'unwrapping' the phase and dividing it by the time interval. Right: Range change rate in mm/yr along the cross-section shown by the black line in the center figure. Note: An increase in range change means the distance between the satellite and ground has increased.*

Step 2 (Subtask 1.5) - Inverse modeling: Once we have the observable quantity, i.e., wrapped or unwrapped range change values from Step 1 (Fig 2.1-3.), we can perform inverse modeling to estimate model parameters such as the depth and geometry of the sources that are causing the deformation observed in the interferograms. Typically, semi-analytical models (Okada, 1992 or Mogi, 1958) are used for the initial inversions, as they are computationally inexpensive to run. These models simulate the deformation caused by expansion or collapse of finite rectangular or point sources embedded in elastic half-space. Other relatively simple and fast approaches such as boundary elements can be similarly implemented. The advantage of this approach is an efficient exploration of the sensitivity of predicted surfaces displacements to the parameter space that: (1) provides first-order analysis, (2) improves conversion of phase shift to line-of-site displacement,

and (3) informs more complex modeling such as in Task 3. The inversion procedure is essentially the same when more complex finite element modeling is conducted.

The starting point for the inversions are x, y coordinates (e.g., in UTM coordinate system), unwrapped range change values (e.g., shown in Figure 2.1-3) and the look angle of the satellite. The source code that we have developed to perform the non-linear inversion along with a sample data file is available at: http://defmod-utils.googlecode.com/ (within the inversion/non-linear sub-directories; update see: https://bitbucket.org/stali/defmod-utils/src/master/). A working example containing data from Brady is available at: https://temple.box.com/s/q77k156uw0mzwf5jk6lemndjeehaafrl.

The code supports both global as well as local optimizations. For semi-analytical models (e.g., Okada, 1992 or Mogi, 1958) either can be used. However, for computationally expensive fully numerical poroelastic or thermoelastic models described later, local optimization is more appropriate.

The parameter file 'params.txt' contains the initial estimates (for Okada (1992) and/or Mogi (1956) based models). The file 'data.txt' contains the coordinates, the observable and the look angle (represented by 3 numbers between -1.0 and 1.0). A beta user can perform the inversion by running the commands in the README file. After the inversion, the final estimate of the parameter values can be used to plot the modeled range change, using GMT, as shown in Figure 2.1-4.

It should be noted that in this implementation (and thus results immediately below), the fitting function or 'forward model' used for calculating the displacements is based on semi-analytical solutions given by Okada (1992) and Mogi (1958). Additional sources can be added simply by modifying the template 'fmdl.f90'. The fitting function ‘fmdl’ can also be replaced by any code, e.g., a finite element code (as we show later) that incorporates more physics.

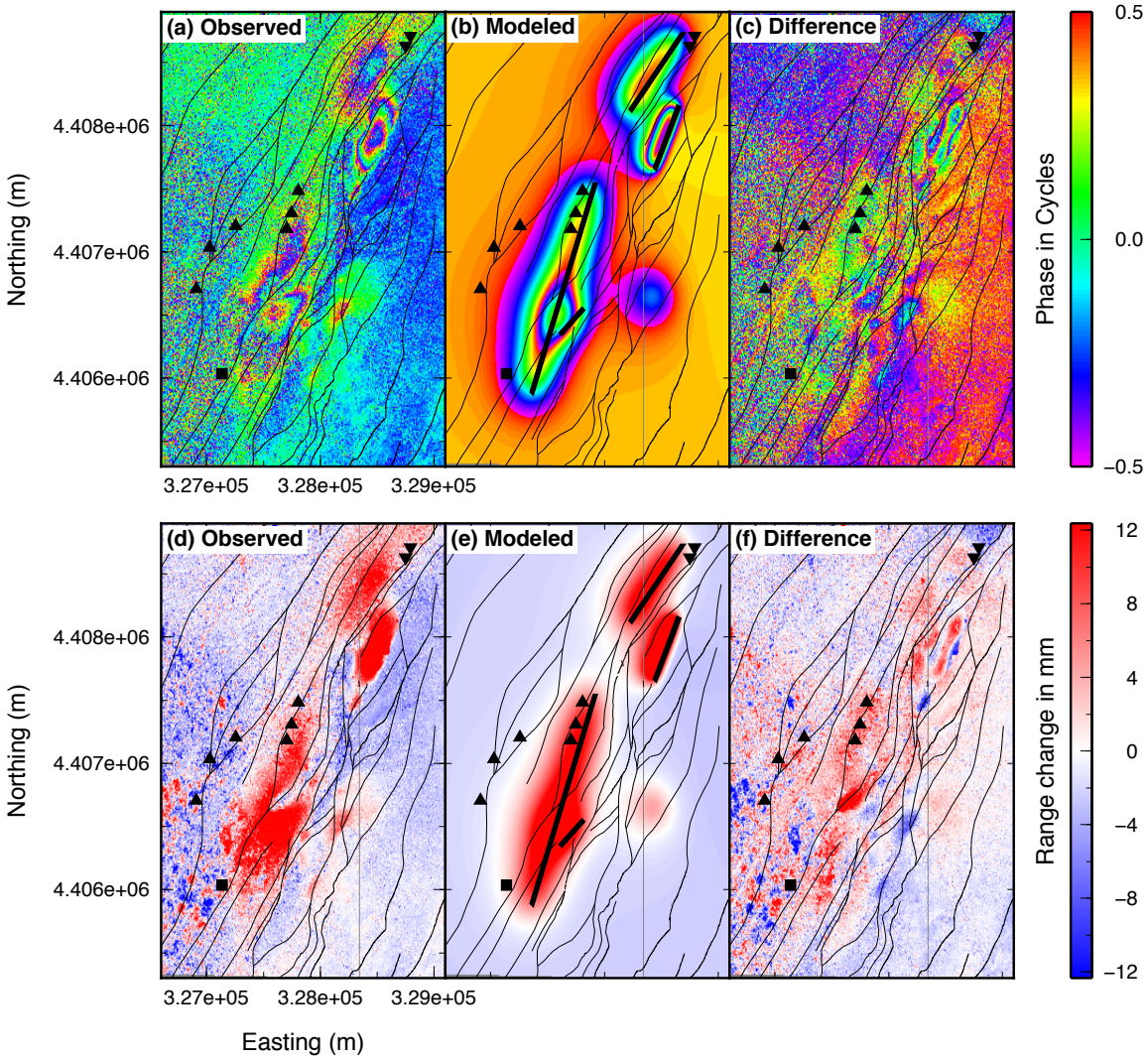

***Figure 2.1-4**: (a) Interferogram showing observed values of wrapped phase change for a pair of TSX images in Track 53, spanning the 363-day interval from May-13-2013 to May-11-2014. One colored fringe corresponds to one cycle of phase change, or 16 mm of range change. (b) Modeled wrapped phase values calculated from the final estimate of the parameters in the elastic model. (c) Residual values of the phase, calculated by subtracting the modeled values from the observed values. (d), (e) and (f) show the corresponding range change values in mm.*

The estimated parameters can also be used to plot other quantities of interest such as the total volume change during the observation period defined by the interferogram. For example, the total volume change estimated for the pair shown in Figure 2.1-4 is -21290.696 +/2129.0 m^3/year. The total volume change provides a convenient scalar quantity that is especially useful when comparing different interferograms.

Step 3 (Subtask 1.2 and 1.4) - Time series analysis with temporal adjustment: Once we have estimates of the model parameters (e.g., rate of volume change and its uncertainty) from multiple pairs, spanning different time intervals, we can perform time series analysis. The time series analysis is helpful in understanding the behavior of the deformation sources over time. Time series analysis is discussed in detail by Ali et al. (2016) and section 3.1 of the Phase 1 Stage Gate Report

The input file used in the analysis simply contains the dates spanned by the interferometric pair and the volume estimate along with its uncertainty. For example, the volume estimates (rates in m^3/year) for 354 pairs, spanning the 2004-2014 time interval are shown in the top plot in Figure 2.1-5.

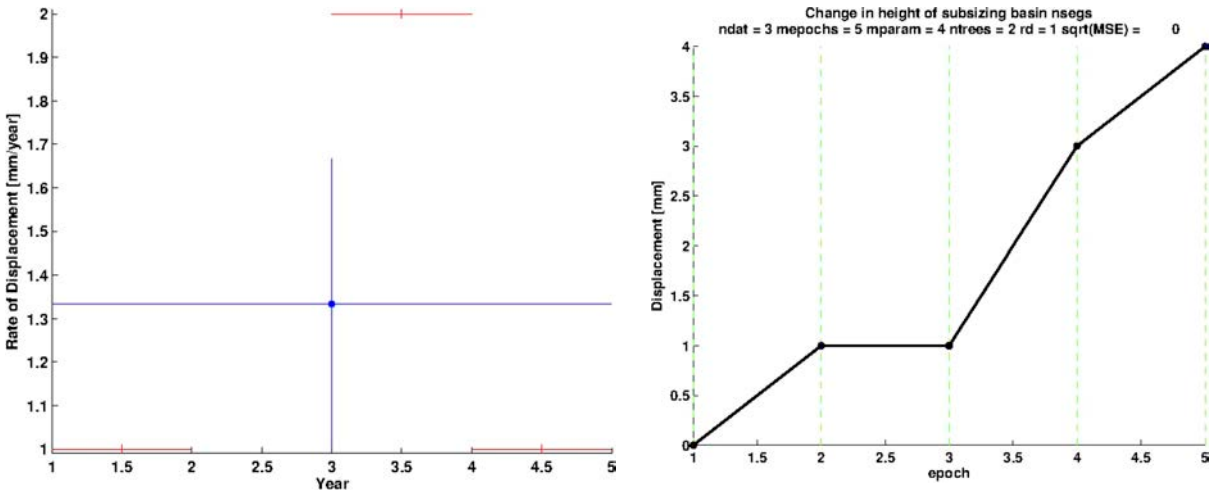

Figure 2.1-5*: (Left) Rate of volumetric change estimated from each interferometric pair individually. For each pair the horizontal bar indicates the time interval spanned by the interferogram. The vertical bar indicates the uncertainty of the estimate, as determined by bootstrap resampling. (Right) Volume change as a function of time estimated from the time series analysis. Line segments between black dots show result for each individual. The parametrization is a piecewise linear function of time (Y axis).*

The beta user can then perform the temporal adjustment revealing the variation in a deformation characteristic illustrated in the right-hand plot in Figure 2.1-5. The algorithm for temporal adjustment is named GraphTreeTA and described by Reinisch (2016, https://gdr.openei.org/files/1075/ReinischEC_MS_thesis_20160728.pdf). The 2015 MATLAB code is available at ***protected***.

The input to the GraphTreeTA code is a file consisting of four columns, i.e., T1 (decimal year), T2 (decimal year), Estimated rate (in m^3/year) and its uncertainty (in m^3/year). A sample file is included with the source code along with instructions. A number of time functions are available and can be specified by the user (e.g., piecewise linear, exponential, polynomial etc.).

The temporal adjustment reveals how deformation, as well as the characteristics of the deformation source, evolves over time. In themselves, these variations provide first-order insight into the evolution of reservoir characteristics. Comparing these results to independent constraints from pumping histories, temperature change, or seismicity allows hypothesis testing of the mechanisms governing reservoir behavior.

APPENDIX: Updated Section 2.2: Seismicity

2.2 Seismicity (SOPO Task 2)

Accurate hypocentral locations and a complete catalog of earthquake activity is essential to deducing the relationship between pumping, stimulation, and the reservoir. In addition, focal mechanisms provide important insights into the structures sustain slip induced by these activities and reflective of the reservoir structure. In this section we outline the workflow to improve location accuracy and improve earthquake detection. To accomplish these tasks, we have also implemented new tasks to improve the velocity model through various techniques.

This section describes SOPO Subtasks 2.1, 2.2 and 2.3, which together comprise the streamlined seismological analysis presented here (Subtask 2.4).

2.2.1 Workflow Outline

Task 2 constrains reservoir behavior through subsurface deformations manifesting as seismicity. It has combined development of a 3D velocity model with earthquake relocations and advanced detection of micro-earthquakes. The workflow for the analysis of seismic data is split into two distinct paths. One path is for triggered data and a second path is followed for the analysis of continuously recorded data (Figure 2.3.1). Accordingly, in the steps documented below, these are presented as two distinct paths.

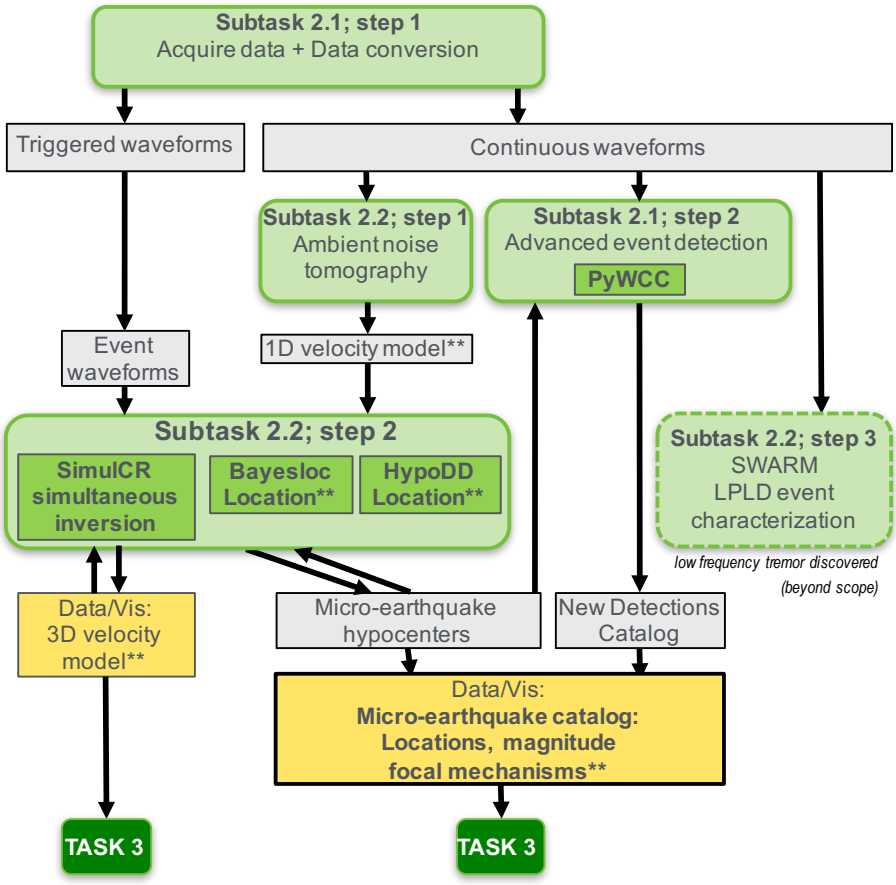

Figure 2.3.1: *Summary of steps in the workflow leading from either triggered or continuously recorded seismic data to data products including velocity models, event location catalog, and earthquake properties such as focal*

mechanism solutions.

2.2.2 Workflow Description

Step 0: Download Data: Subtask 2.1

Continuous data

Acquire continuous seismic data recorded by the Brady's seismic network from LBL. The data are delivered in either Reftek raw format or Nanometrics Taurus Yfile format. Reftek data are converted to mseed format using the Reftek utility *rt_mseed* and then to Seismic Analysis Code (SAC) format using *ms2sac*, which can be downloaded as part of the IRIS/PASSCAL software package from: *http://www.passcal.nmt.edu/ftp/software/passoft* .

Yfile format data are converted to SAC using either software provided by Nanometrics or the LLNL program Yfile2sac. Hour-long SAC files for each sensor component are saved in directories arranged by day/station.

Triggered data

Download *.evt files for triggered events detected by the Brady's telemetered network from: *http://fracture.lbl.gov/Bradys/process/evtfiles*.

*.evt are binary format files used in LBNL's REMUS earthquake data processing package (see Subtask 2.2 below). Each file contains all the recorded traces for one event in binary format converted from Taurus Yfile format. Filenames are in the form *yyMMddhhmmss*.evt, in which *yy* is the last two digits of the year, *MM*, *dd*, *hh*, *mm*, *ss* are month, day, hour, minute, second, respectively. Waveform data in the *.evt files can be converted to SAC using the code ***** contained in the REMUS package. In addition to the waveform data, each *.evt files contains P- and S-wave arrival time picks and an initial hypocentral location resulting from automated near real-time analysis. The *.evt files are contained in an MySQL (open source) database. LBNL are in the process of making the entire database available for public access at the Northern California Earthquake Data Center (NCEDC) (http://www.ncedc.org/).

Alternatively, download SAC format files from:

http://fracture.lbl.gov/Bradys/process/sac_files.

Each tar/zip file contains individual SAC trace files for each event from all network stations. Filenames are in the form Bradys.*yyMMddhhmmss*.tar.bz2, in which the date-time string is the same as for *.evt files.

Step 1: Advanced Detection (Subtask 2.1)

Objective: Detect earthquakes and other signals such as tremor using matched filters.

Required: Continuous seismic data and station meta-data.

Result: List of detections with a measure of robustness. Note: Does not necessarily include picked arrival times.

The analysis is carried out in the following steps:

1.1. Inputs are continuous data in SAC format created as described above. SAC file headers including station location and component metadata must be correctly filled out. The SAC files are copied into directories organized by day.

1.2. Load data files into the Oracle database using the script *SacFileLoader*. This script is run at a directory level above the directory containing the SAC files.

1.3a. Automated detection: Create initial template configuration files using the script *ConfigCreate*. Edit the configuration files *stalata_parma.txt* and *STREAMS.txt* to match the data and to produce the desired processing stream. The following is an example configuration for the Brady's data.

```
.StaChanList
BPRT1 HHZ
.EndList
detectorType = STALTA
threshold=50.000000
blackoutPeriod=10
offsetSecondsToNominalPick = 0.0
STADuration=1
LTADuration=10.0
gapDuration=1.5
enableSpawning=true
```

stalta_params.txt: Select STA/LTA parameters appropriate to short signals; STA/LTA = 1/10 and an STA/LTA threshold of 50 (shown in red).

```
StreamName = STREAM1
Passband          = 0.500000 5.000000
PreprocessorFilterOrder = 4
DecimatedBlockSize = 4000
DecimationRate = 4
# New subspace detectors created from detections will be created using these parameters
SubspaceThresholdValue  = 0.600000
SubspaceBlackoutPeriod  = 3.0
EnergyCaptureThreshold  = 0.9
# If UseConfigFileThreshold is true then retrieved subspace detectors will use threshold in this file.
UseConfigFileThreshold  = true
# To specify detectors using user-supplied templates use a line like the following where
/some/absolute/path is the name of the file with the specification file list.
#DetectorSpecificationFileList = /some/absolute/path
SpawnCorrelationDetectors = true
# If next line is true, then although spawners will run, they will not produce triggers.
TriggerOnlyOnCorrelators = false
LoadCorrelatorsFromDb = true
# To view and classify power detections as they are created, set to true.
ViewDetections = false
# SNR Trigger Screening----------
# Lengths are in seconds
SnrThreshold = 3.0
# Duration Trigger screening ----------
# events must be at least this long in seconds to be a valid trigger
MinEventDuration = 0.5
```

STREAMS.txt: This is a complex file, and here we show selection only the most significant parameters.

1.3b: User-defined template pattern: Set up an initial template configuration using *ConfigCreate* and edit the configuration files as described in Step 3a. Then select an example of the desired template signal from the waveform data. Extract the sample in

a SAC window and place it in the directory STREAMS/templates/template0 created by *ConfigCreate*. Edit the template.txt file also created by *ConfigCreate* as required.

1.4. Run the detection algorithm

1.5. Examine the detection results using the *Start_Builder* program GUI (Figure 2.3-2 and 2.3-3).

1.6. Extract the detections from the database using the program *sqlplus* to compile a table containing the beginning (epoch) time and duration of the signal (secs) and a statistic indicating the quality of the detection.

TIME	STATISTIC	SIGNAL DURATION
1330197838	.540468454	11.12
1330197840	.523714721	13.064
1330197839	.53042984	12.712
1330198490	.518522978	11.184
1330198854	.502693892	10.264
1330199457	.516030908	11.392

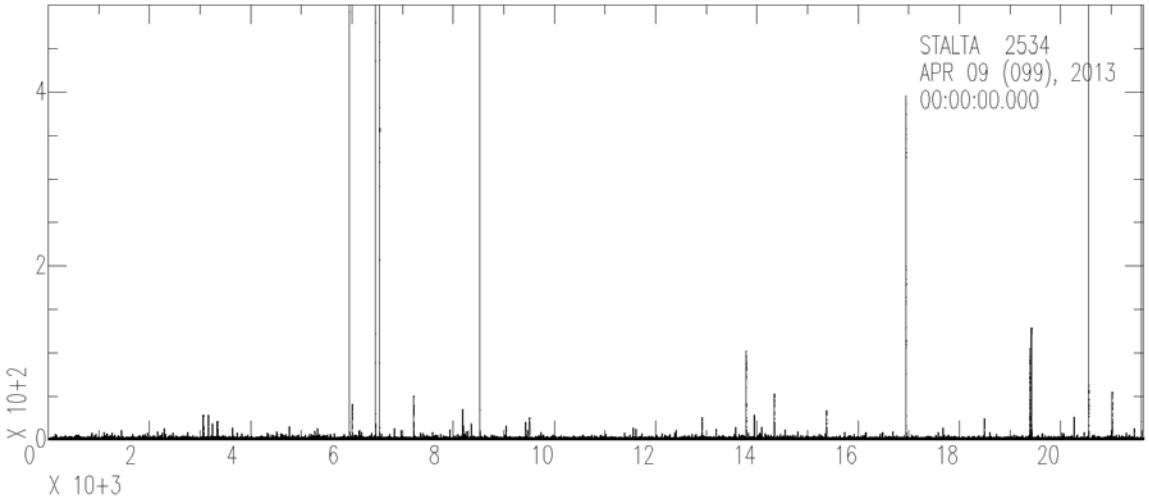

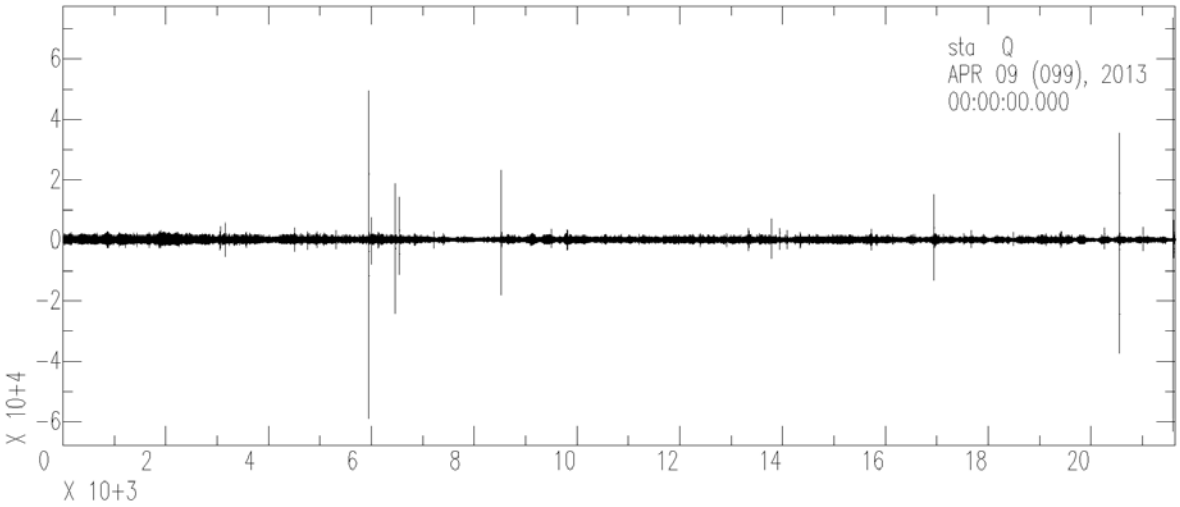

Figure 2.3-2: *(Top) Example of detections at one station using the standard STA/LTA component of the detection routine. (Bottom). The original raw data showing the detected events.*

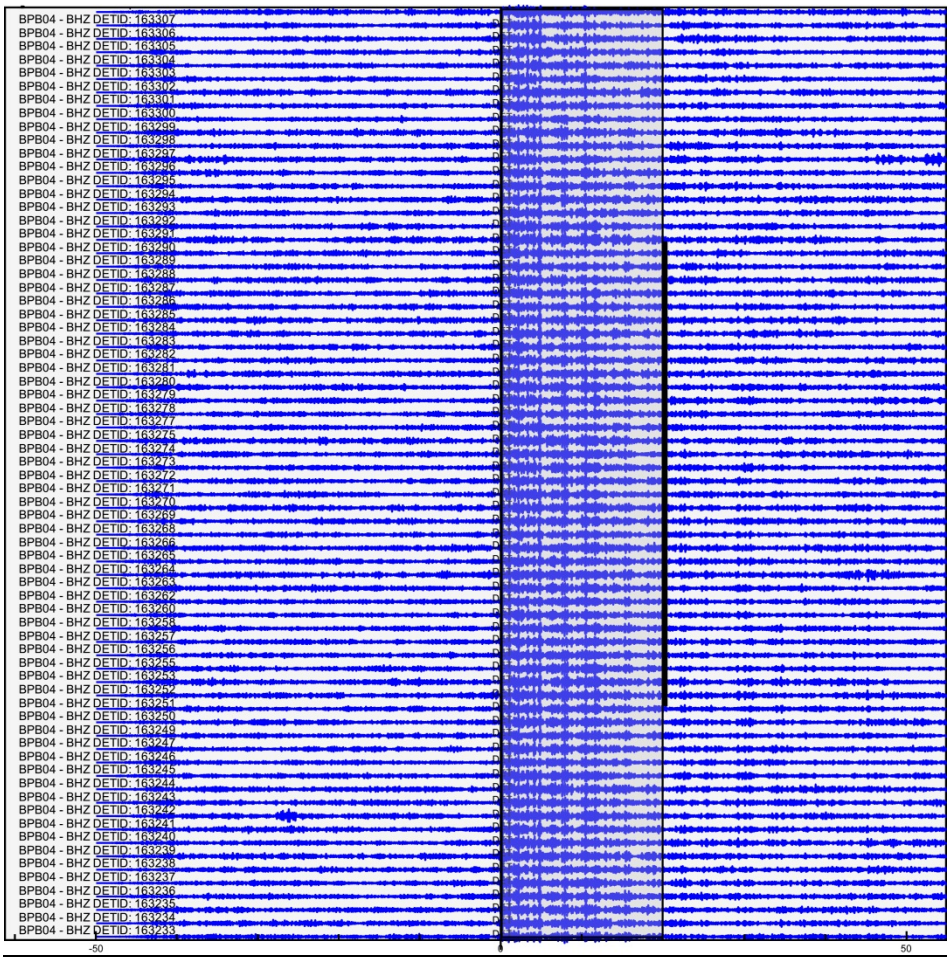

Figure 2.3-3*: Example detections of an unknown signal recorded at BPB04 BHZ, days 2013:113 – 2013:248. 1732 different events were automatically detected, each with similar characteristics.*

To streamline this process, a new tool PyWCC, written by Dennse Templeton was written in Python (taking advantage of the modules ObsPy, numpy, and scipy). The software tool employs the same scheme of advanced detection by interrogating continuous data and comparing it to known, triggered earthquakes. The program package includes documentation on how to configure and run the code, a short tutorial, and a worked example with associated test dataset based on the permanent Bradys seismic network data. The program package is released for outside distribution through LLNL review and release procedures (https://www.osti.gov/biblio/1379475-python-waveform-cross-correlation). The software is publicly available at https://github.com/templetond/pywcc.git. Required inputs to the program include the continuous data, a station text file, a master template text file, and a program input text file.

Step 2. Earthquake Locations (Subtask 2.2)

The determination of hypocentral locations requires two important elements. First a reliable velocity model must be established. Second, locations can be derived. In the case where only a small number of earthquakes are available, they may be inadequate to constrain seismic velocity. In this case continuous recordings can be used to derive a velocity model from ambient noise.

(Step 2.A) Ambient noise velocity model

P- and S-wave velocity models are derived from ambient noise tomography using the Computer Programs for Seismology toolkit developed by R. Herrmann and his colleagues at St. Louis University. The processing here is based on the ambient noise processing scripts available in the tutorial section. The toolkit can be downloaded from http://www.eas.slu.edu/eqc/eqccps.html.

The steps in the ambient noise analysis are as follows:

2.A.1. Assemble continuous data in SAC format and metadata including instrument response files (if all the stations have the same sensor, then it is possible to process without correcting for the instrument response). Put data into correct directory structure following the format in the *NOISE* example. Edit the *DOITALL* script to match the data:

- Change the 'YEAR", "FREQLIMITS", and "BASE". (If response files are not available, comment that section of the script out.)
- Edit *DOSTACK* for the correct year

2.A.2. Run the *DOITALL* script to compute stacked cross-correlations between all pairs of stations. An example of stacked cross-correlations is shown in Figure 3.1-4.

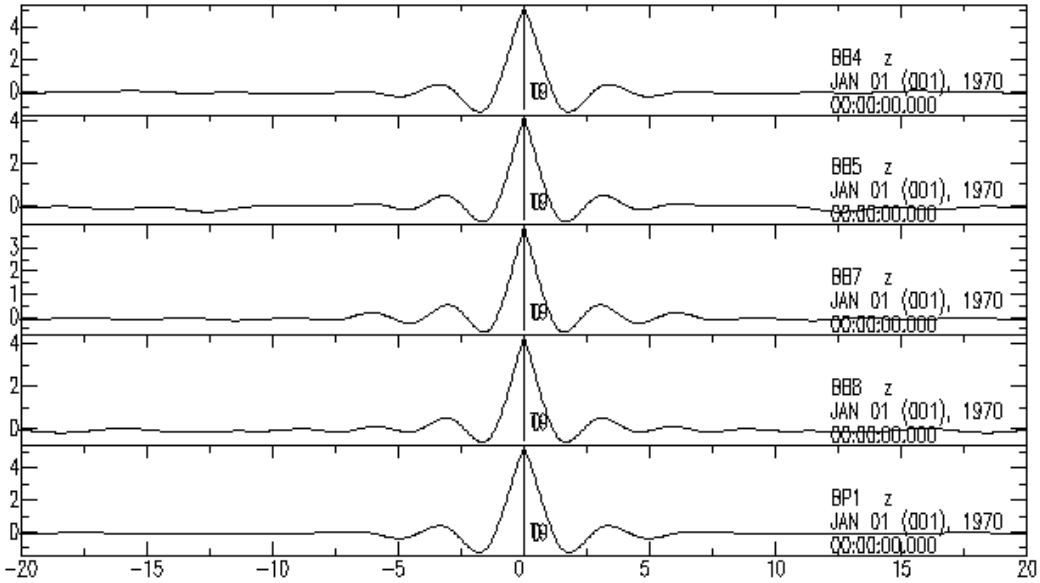

Figure 3.1-4*. Examples of stacked cross-correlations for 5 paths using one month of data from the Reftek sensors.*

2.A.3. Calculate and pick dispersion curves: In the STACK directory there will be a set of files named STA1CHANSTA2CHAN.WSTK (e.g., BPRT1HHZBPRT3HHZ.WSTK, BPRT2HHZBPRT3HHZ.WSTK, BPRT3HHZBPRT4HHZ.WSTK)

The number of pairs depends on the number of stations; for the 5-station Reftek network 10 correlations will be generated.

Run the *do_mft* script; i.e. *do_mft *.WSTK*

This brings up a window showing the file names. Adjust relevant parameters; alpha (size of filtering kernel), minimum and maximum periods and velocities. Pick dispersion curve from multiple filter display. The default parameters are designed for larger events and longer distances and must be modified to fit the short high-frequency surface waves recorded by a local network. This is the most challenging part in order to avoid picking higher order surface waves.

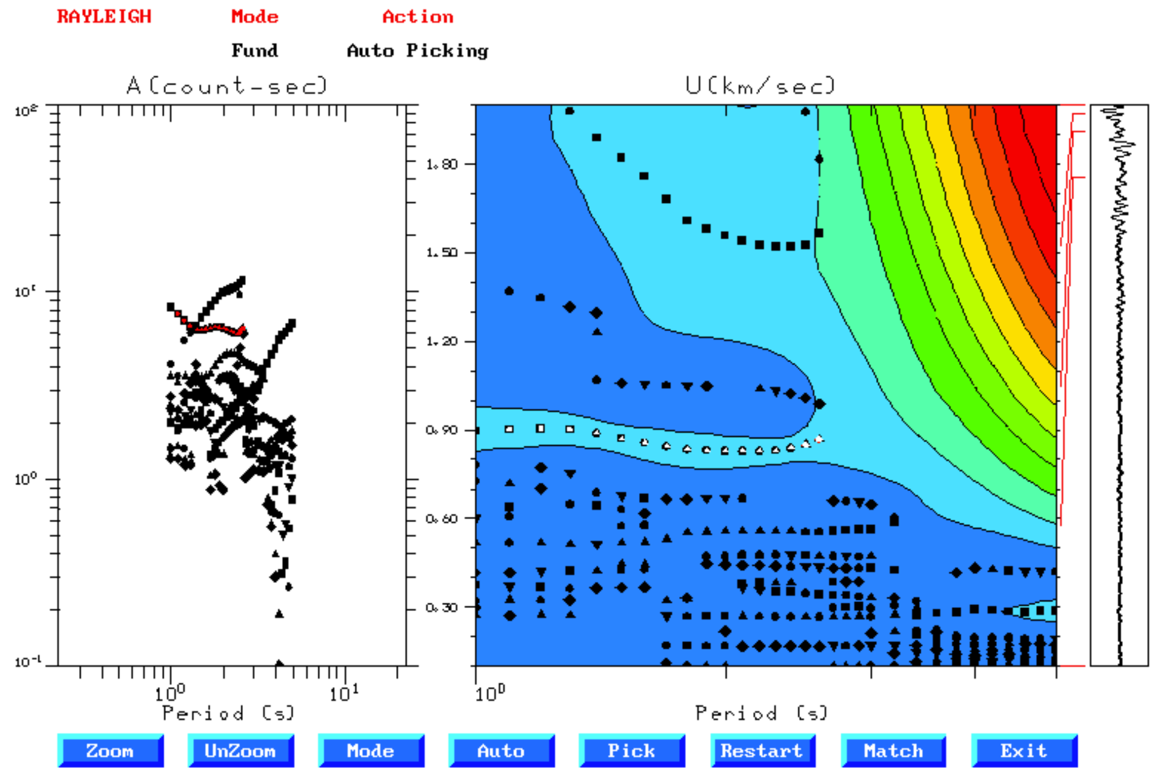

Figure 3.1-5*: Example of picking dispersion curve for Rayleigh (Z) between stations BRPT5 and BPRT1. The left shows possible dispersion automatically generated automatically while the right-hand side displays the same information overlaid on power plotted as a function of period (x axis) and time (y axis). The preferred dispersion curve is then picked manually (white dots on right; red on left).*

2.A.4. Inversion for body wave velocity structure: Convert the dispersion curve to SURF96 format. Note: In this example only one dispersion curve is inverted for simplicity. Edit sobs.d and the starting model file, start.mod

Starting model (half-space):

H (KM)	VP (KM/S)	VS (KM/S)	RHO (GM/CC)	QP	QS	ETAP	ETAS	FREFP	FREFS
1.0000	3.0000	1.7000	2.3000	0.118E-02	0.167E-02	0.00	0.00	1.00	1.00
1.0000	3.0000	1.7000	2.3000	0.118E-02	0.167E-02	0.00	0.00	1.00	1.00
1.0000	3.0000	1.7000	2.3000	0.118E-02	0.167E-02	0.00	0.00	1.00	1.00
1.0000	3.0000	1.7000	2.3000	0.118E-02	0.167E-02	0.00	0.00	1.00	1.00
1.0000	3.0000	1.7000	2.3000	0.118E-02	0.167E-02	0.00	0.00	1.00	1.00
0.0000	3.0000	1.7000	2.3000	0.377E-02	0.592E-02	0.00	0.00	1.00	1.00

2.A.5. Run the surf96 program to invert for the final P- and S-wave velocity and attenuation models. The output also includes a fit of the model to the data as shown in Figure 3.1-6 which compares the starting and the ending velocity models.

Ending model (half-space):

H (KM)	VP (KM/S)	VS (KM/S)	RHO (GM/CC)	QP	QS	ETAP	ETAS	FREFP	FREFS
1.0000	1.7988	1.0192	2.3066	0.118E-02	0.167E-02	0.00	0.00	1.00	1.00

1.0000	2.4577	1.3929	2.4151	0.118E-02	0.167E-02	0.00	0.00	1.00	1.00
1.0000	2.4408	1.3829	2.4126	0.118E-02	0.167E-02	0.00	0.00	1.00	1.00
1.0000	2.5715	1.4572	2.4308	0.118E-02	0.167E-02	0.00	0.00	1.00	1.00
1.0000	2.7191	1.5408	2.0940	0.118E-02	0.167E-02	0.00	0.00	1.00	1.00
0.0000	2.8612	1.6213	2.1223	0.377E-02	0.592E-02	0.00	0.00	1.00	1.00

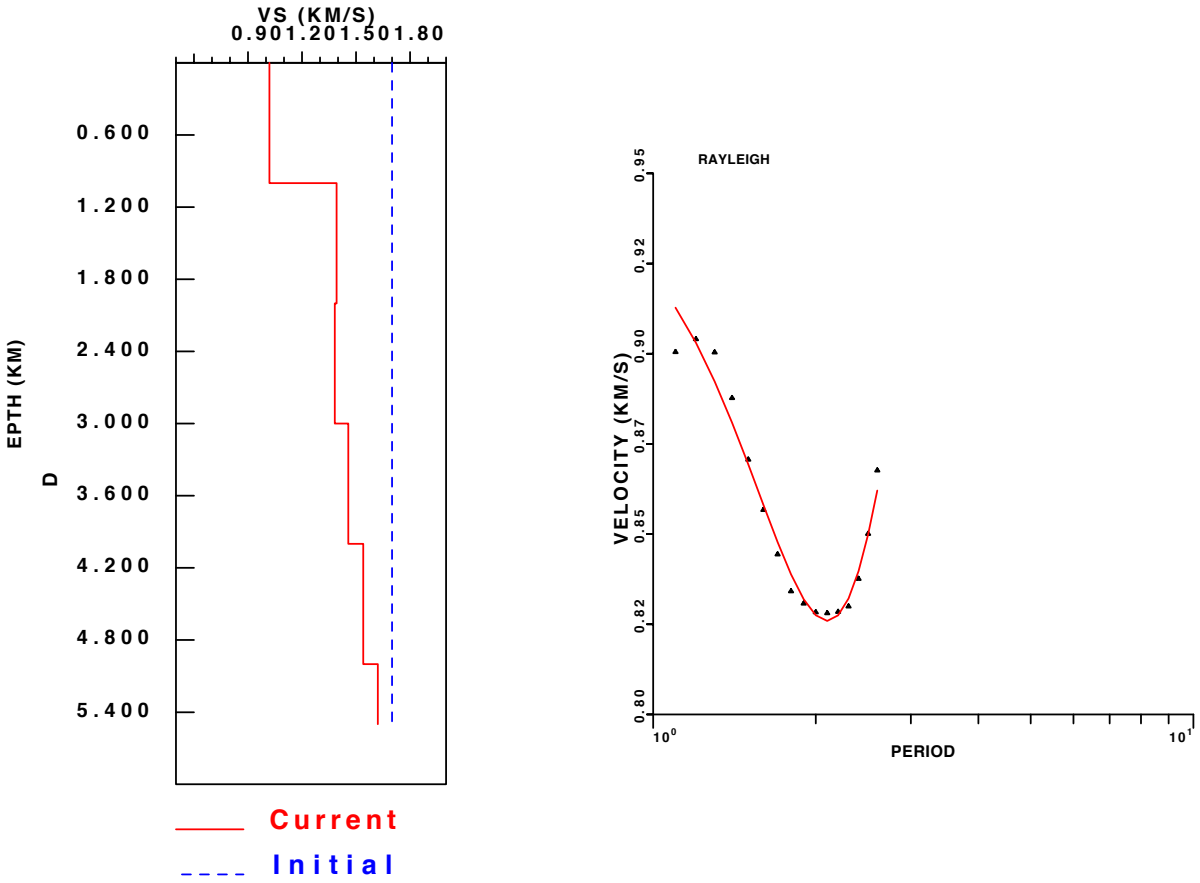

Figure 3.1-6:. *Example output showing end model (red) with starting model (blue) and the fit of the model dispersion curve (red) with the picked points (black).*

(Step 2.B) Hypocenter Location

Once a velocity model is established, there are *three alternative* methods for locating micro-earthquakes included in this workflow. These are Baysloc, hypoDD and SimulDD. The reason for considering alternative methods is that each is appropriate for application to particular sets of available data and for producing particular types of output, as outlined below. Baysloc and hypoDD are discussed individually in the following sections, while SimulDD is discussed as part of the LBNL integrated REMUS analysis package.

Step 2.B-1 – *Baysloc*

Bayesloc is a Bayesian-based location program. While capable of both single and multiple locations, its primary advantage is that it generates realistic error bounds. These include the effect of travel time errors stemming from uncertainties in velocity models as well as arrival time and other errors. The current widely-available implementation used so far was designed for

locating regional/teleseismic events, but a version for locating local microearthquakes is under development [Myers et al., 2007; 2009]. Bayesloc is available from

https://missions.llnl.gov/nonproliferation/nuclear-explosion-monitoring/bayesloc

The Bayesloc processing steps are as follows:

2.B-1.1. Metadata: Construct a station file giving the location for each seismic station (Figure **) and a configuration file specifying processing parameters (Figure 3.1-7).

```
sta  id lat     lon       elev
BP01  39.797889 -119.005917 1.264
BP02  39.782889 -119.008444 1.236
BP03  39.778611 -119.012833 1.261
BP04  39.777167 -119.021833 1.204
BP05  39.781444 -119.021556 1.204
BP06  39.776444 -119.039917 1.231
BP07  39.791000 -119.028972 1.202
BP08  39.795083 -119.023250 1.201
BPB3  39.778750 -119.013111 1.218
BPB4  39.777028 -119.019917 1.153
BPB5  39.781444 -119.021556 1.147
BPB7  39.791028 -119.028833 1.144
BPB8  39.795194 -119.023361 1.149
```

Figure 3.1-7*: Example station file.*

2.B-1.2. Travel-time file: The TauP toolkit developed by Crotwell et al. (1999) is used to generate a file containing P- and S-wave travel time tables (Figure 3.1-8) from a 1D ambient noise (or other) velocity model. The TauP toolkit can be downloaded from http://www.seis.sc.edu/TauP.

```
# Bradys travel time for phase: P
10 Number of depth samples at the following depths (km):
 0.00  0.10  0.20  0.30  0.40  0.50  0.60  0.70  0.80  0.90

10 Number of distance samples at the following distances (km):
0.00  0.01  0.02  0.03  0.04  0.05  0.06  0.07  0.08  0.09
# Travel time at depth =  0.0 km
0.000
0.370
 0.741
1.111
1.482
1.852
2.222
2.593
2.963
```

```
// arrival data and station
Data:
{
 arrival_file = "Brady.arrival.dat";
 station_file = "Brady.station.dat";
};
TravelTimeModel:
{
 phase = ["P","S"];
 tt_prefix = "Bradys.";
};
TravelTimeError:
{
 use_tte = true;
};
Output:
{
 level = "medium";
};
```

***Figure 3.1-8**: (top) Travel time file for Bayesloc (bottom) Input control file*

2.B-1.3. Steps 1 and 2 need to be done once for each network and do not have to be revised unless a new velocity model is constructed or new stations are added.

2.B-1.4. Phase arrival picks: P arrivals may be picked automatically and then reviewed for accuracy and revised as necessary using the LBLN REMUS package described below. Alternatively a phase picker such as that provided in the SAC toolkit can be used. Phase arrivals are converted into Bayesloc input format (Figure 3.1-9).

```
ev_id sta_id phase time
   68   BP01  P     1296802936.90536
   68   BP08  P     1296802937.06761
   68   BP07  P     1296802937.22505
   68   BP02  P     1296802937.19981
   68   BP03  P     1296802937.32360
   68   BP04  P     1296802937.46181
   68   BP05  P     1296802937.35004
   68   BP06  P     1296802937.67934
   68   BP01  S     1296802937.28230
   68   BP08  S     1296802937.71379
   68   BP07  S     1296802938.07354
   68   BP02  S     1296802938.11903
   68   BP06  S     1296802938.90686
```

***Figure 3.1-9**:. Example phase file.*

2.B-1.5. Run Bayesloc: The output is in a directory named output. This contains log files replicating the input data as well as a file named origins.out that contains the possible locations for the events and plotted in Figure 3.1-10.

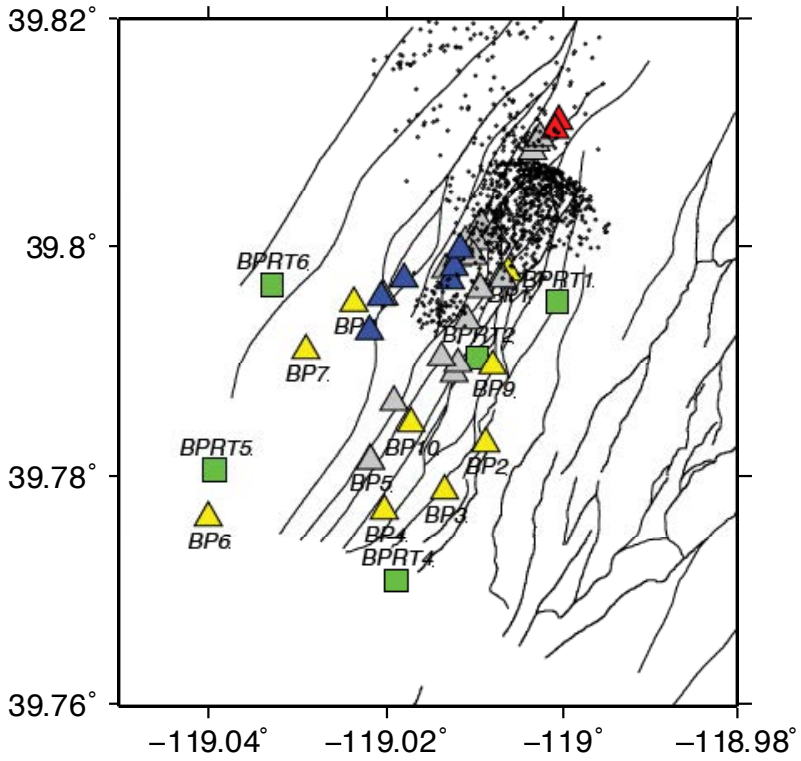

Figure 3.1-10*: Possible locations an earthquake assuming various realizations of the input data (e.g. velocity model and phase pick errors).. Note that the locations are constrained by the northernmost station, as expected.*

Step 2.B-2 – *HypoDD*

hypoDD is a standard double-difference location algorithm that yields accurate relative locations (Waldhauser and Ellsworth, 2000; Waldhauser, 2001) that are useful for defining trends that can be used, for example, to identify fault planes or volumes perturbed by injection/production. However, absolute locations may include systematic biases. hypoDD can be downloaded from: *http://www.ldeo.columbia.edu/~felixw/hypoDD.html*

The HypoDD processing steps are as follows:

2.B-2.1. Data are converted from the arrival data using the LLNL Python script make_hypo.py, which creates an input file to program ph2dt. ph2dt is downloaded and installed along with hypoDD and is run to generate the hypoDD input phase file hypoDD.inp.

2.B-2.2. hypoDD is then executed with hypoDD.inp as the argument.

2.B-2.3. Download obspy from: http://docs.obspy.org/index.html

Step 2.B-3 – *SimulDD: Data Processing using LBNL integrated package REMAS with locations via SimulDD*

The REMAS automated micro-earthquake processing system (Hutchings et al., *Proc. GRC Ann. Meeting,* 2011) is a Python software package that includes:

- Initial earthquake location from automated arrival time picks of P and S phases.
- Automatic seismic moment and magnitude determination.

- Graphical user interface (REMAS waveform plotter) to enable verification of automatic phase arrival time picks and manual re-picking as required.
- Automatic generation of phase pick files and meta-data files (phases.dat), for input to simultaneous inversion for velocity and hypocenter location, and for attenuation and source mechanism analyses.
- Earthquake location, simultaneous inversion, attenuation and source mechanism codes.

REMAS will be available from LBNL under a licensing agreement in the near future.

The REMAS (SimulDD) processing steps are as follows:

3.1. Preliminary processing and phase arrival picking:

Initial earthquake locations from automated P- and S-phase picks are already stored in downloaded *.evt files (see Subtask 2.1 above). All downloaded *.evt files are stored in one directory and Python script reprocessing.py in the REMAS package is executed with the directory path as the argument. This allows a user to tune the picking parameters for a specific region to improve automated picks. After automated picking, the picks can be verified and re-picked manually if necessary using the REMAS waveform plotter GUI. (Fig. 3.1-11). The final arrival time picks are saved in the original *.evt file for each event.

The .evt files are loaded into the MySQL database (see Subtask 2.1) using the script loaddb.py. The phase file, phases.dat (Figure 3.1-11) is extracted from the database using script getphasedotdatfile.py. Both the scripts take the path of the directory containing .evt file as the argument.

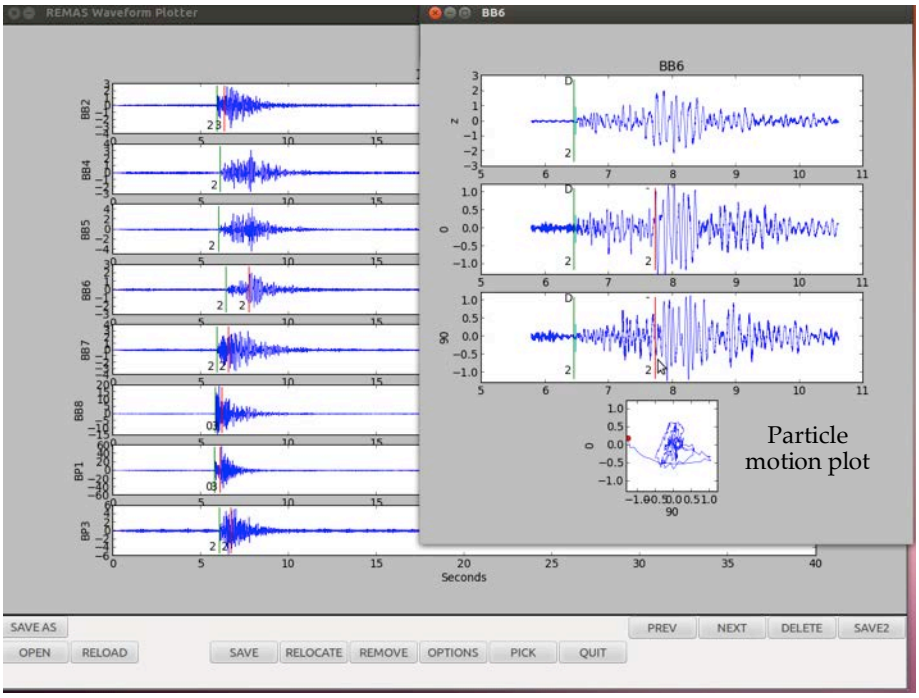

***Figure 3.1-11**: REMAS waveform plotter and picker GUI*

3.2. Simultaneous Inversion for 3D P and S velocity models and hypocenter locations.

SimulCR (Hutchings, et al., 2012) (formerly SimulDD) is a modified version of the FORTRAN code SimulPS (Thurber, 1983) that performs double-difference tomography and earthquake locations simultaneously. Instead of finding just events located close to one another - and thereby eliminating a term in the travel time equation by assuming waves from both events travel the same paths to the receivers (e.g. Zhang and Thurber, 2003). SimulCR identifies events that have overlapping rays to the same station, i.e. "common rays", and utilizes the full travel paths from the events. Therefore, the first advantage of using SimulCR is that it not only provides relative event locations but also simultaneously finds the absolute locations, hence reducing the potential bias in conventional double-difference locations like those obtained from hypoDD. The second advantage is, of course, that it computes 3D P and S velocity structures in the crustal volume traversed by source-receiver paths. These are compared with the 1D or 3D models constrained by ambient noise tomography as an independent check and to assess the uncertainties in the derived velocity structures.

The input files for performing simultaneous inversion are:

- phases.dat
- stations.dat
- text file containing a 1D or 3D starting velocity model
- control.dat

Examples of phase, station and control files are shown in Figures 3.1-12 to 3.1-14. In addition to station names and locations, the station.dat file gives a local reference origin. The control.dat file provides parameters such as convergence criteria that control the inversion. The initial starting velocity model is constructed from prior information. Explanations of the input and output file formats and commands are given in the main program code (simul.f). All the input files are stored in one directory and the code SimulCR is run in the same directory with control.dat as the argument.

Outputs of SimulCR are text files containing 3D P- and S- wave velocity models with measures of resolution, hypocenter locations and diagnostic statistics.

```
# 2010 12 10 08 26 22.546  39.80372 -118.99423  -0.114  0.65 0.000    0.0 0.000 2200022
5BBB8  1.250 0.50 P D 0.019 0.000 0.000
5BBB8  2.036 0.50 S - -0.000 0.000 0.000
5BBB6  1.846 0.50 P U 0.013 0.000 0.000
5BBB6  3.336 0.50 S - -0.000 0.000 0.000
5ABP2  1.368 0.50 P U 0.023 0.000 0.000
5ABP2  2.072 0.50 S - -0.000 0.000 0.000
# 2010 12 10 10 43 45.135  39.80743 -118.98940   1.714  1.28 0.000    0.0 0.000 2200568
5BBB8  1.113 0.25 P U 0.035 0.000 0.000
5BBB8  1.943 0.25 S - -0.000 0.000 0.000
5BBB7  1.309 0.25 P D 0.021 0.000 0.000
5BBB7  2.263 0.25 S - -0.000 0.000 0.000
5BBB6  1.919 0.25 P D 0.027 0.000 0.000
5BBB6  3.127 0.25 S - -0.000 0.000 0.000
5BBB5  1.465 0.50 P U 0.043 0.000 0.000
5BBB5  2.500 0.50 S - -0.000 0.000 0.000
5ABP2  1.237 0.50 P U 0.027 0.000 0.000
5ABP2  2.293 0.50 S - -0.000 0.000 0.000
# 2010 12 15 13 54 07.738  39.79927 -119.00080   0.552  1.21 0.000    0.0 0.000 2200024
5ABP1  0.815 0.75 P U 0.019 0.000 0.000
5ABP1  1.181 0.25 S D 0.023 0.000 0.000
5ABP3  1.099 0.50 P U 0.025 0.000 0.000
5ABP3  1.811 0.50 S - -0.000 0.000 0.000
5BBB8  0.838 1.00 P D 0.035 0.000 0.000
5BBB8  1.491 0.50 S - -0.000 0.000 0.000
5BBB7  0.939 0.50 P D 0.045 0.000 0.000
5BBB7  1.818 0.50 S - -0.000 0.000 0.000
5BBB6  1.340 0.25 P U 0.013 0.000 0.000
5BBB6  2.584 0.50 S - -0.000 0.000 0.000
5BBB5  1.050 0.50 P D 0.021 0.000 0.000
5BBB5  2.395 0.50 S - -0.000 0.000 0.000
5BBB4  1.234 0.50 P D 0.025 0.000 0.000
5ABP2  0.984 0.75 P U 0.029 0.000 0.000
5ABP2  1.563 0.50 S - -0.000 0.000 0.000
```

***Figure 3.1-12**: Example of phases.dat file*

```
39 46.5866   -119 -2.395   0.0
27
5ABP1   39   47.8278  -119   -0.3550  1262
5BBP1   39   47.8278  -119   -0.3550  1228
5ABP2   39   46.9733  -119   -0.5066  1271
5BBP2   39   46.9733  -119   -0.5066  1237
5ABP3   39   46.7167  -119   -0.7700  1255
5BBP3   39   46.7167  -119   -0.7700  1221
5ABB4   39   46.6300  -119   -1.3100  1243
5BBB4   39   46.6300  -119   -1.3100  1209
5CBB4   39   46.6217  -119   -1.1950  1153
5DBB4   39   46.6217  -119   -1.1950  1243
5EBB4   39   46.6217  -119   -1.1950  1228
5ABB5   39   46.8866  -119   -1.2933  1238
5BBB5   39   46.8866  -119   -1.2933  1204
5CBB5   39   46.8866  -119   -1.2933  1148
5ABB6   39   46.5866  -119   -2.3950  1265
5BBB6   39   46.5866  -119   -2.3950  1231
5ABB7   39   47.4600  -119   -1.7383  1236
5BBB7   39   47.4600  -119   -1.7383  1202
5CBB7   39   47.4600  -119   -1.7383  1145
5ABB8   39   47.7050  -119   -1.3950  1239
5BBB8   39   47.7050  -119   -1.3950  1205
5CBB8   39   47.7050  -119   -1.3950  1149
5BBP9   39   47.3784  -119   -0.4584  1264
5BB10   39   47.0767  -119   -1.0166  1053
5BB11   39   47.1738  -119   -1.1388  1246
```

***Figure 3.1-13**: Example of station.dat file*

```
400  0   0   0  3  0  1  0  2    *** NEQS NSHT NBLS WTSHT KOUT KOUT2  KOUT3 KOUT4 KOUT5
10  0.02  0.02  -0.70 1.0 2.0 4.0 -2.0 *** NITLOC EIGTOL RMSCUT ZMIN DXMAX ANWR BNWR MXMag
10 0.25 0.25 6.31 39.81 1 .1       *** NHITCT DVPMX DVSMX VPDAMP VSDAMP DLDMP STEPL
  1  2  100  0   0.01  0  18       *** IRES I3D NITMAX IHOMO RMSTOP IFIXL MAXSKIP
 15.00 20.00   0.05 0.15          *** DEL1 DEL2 RES1 RES2
  5  0  0.15  0.1  0.1 0.5       *** NDIP ISKIP SCALE1 SCALE2 SCALE3 SCALE4
 1.4  0.002  8  18               *** XFAC TLIM  NITPB1 NITPB2
  1   1   0                   *** IUSEP ISUES INVDEL
  0   0   0   0  0.5  0           *** IQVEL IQTAU IQPUL IQSPC QCST IGMTX
```

***Figure 3.1-14**: Example of control.dat file*

3.3. Visualization

The hypocenter and 3D velocity model output files from SimulCR are converted to VTK format (see *http://www.vtk.org)* using the REMAS Python script *proc_SimulPS.py*, and input to the GUI-driven visualization package VisIt to visualize 3D velocity structures and hypocenter distribution. Seismic station locations, well trajectories, and digitized faults and geology are can also be converted to VTK and included in the 3D visualizations. Examples are shown in Figures 3.1-15 and 3/1-16. VisIt is freely available from:

https://wci.llnl.gov/simulation/computer-codes/visit/downloads

Microearthquake location maps and vertical sections (Fig. 3.1-17) are also created using the mapping tools package GMT5, freely available from:

http://gmt.soest.hawaii.edu/projects/gmt/wiki/Download

GMT5 is run from a set of Unix C-shell scripts and outputs postscript plots.

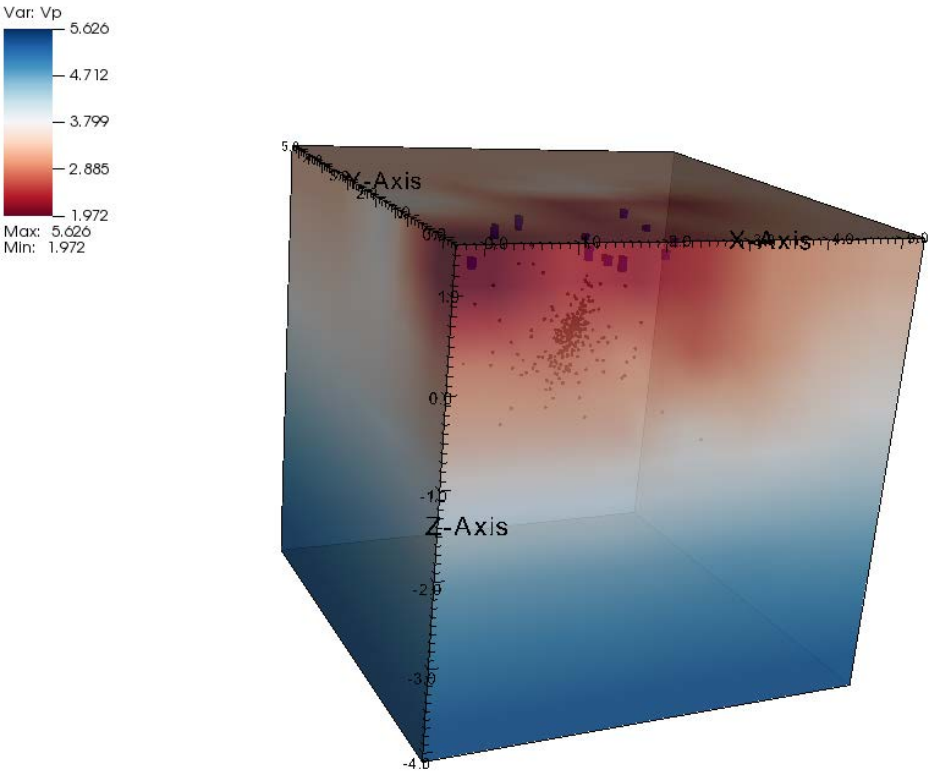

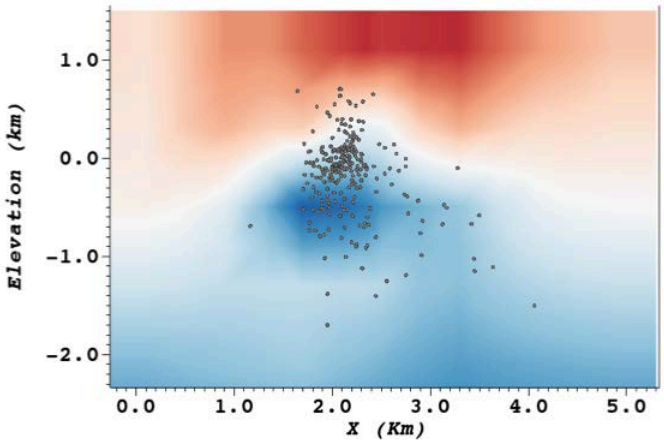

Figure 3.1-15*: (Top 3) D view of V_p velocity model and relocated seismicity using VisIt. (Bottom) Cross-section through the reservoir volume sustaining seismicity (cross-section position is illustrated in Figure 3.1-17 (bottom).*

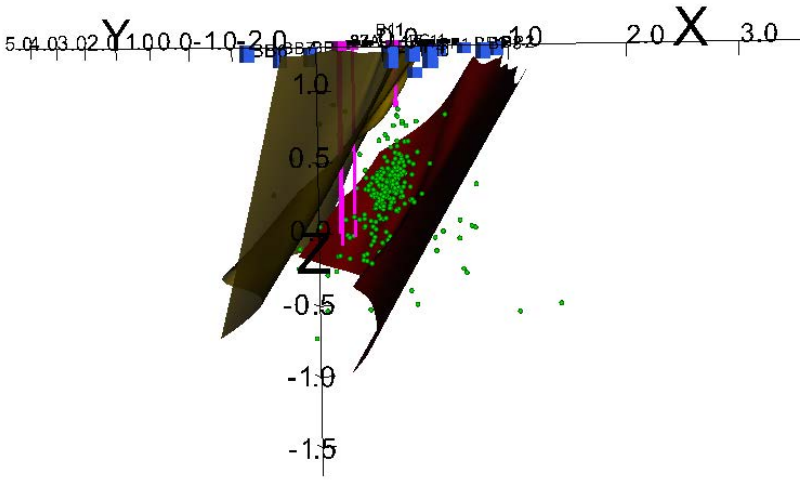

Figure 3.1-16*: SW-NE along-strike (top) 3D perspective views showing the relationship of SIMULDD microearthquake locations to the Brady's fault.*

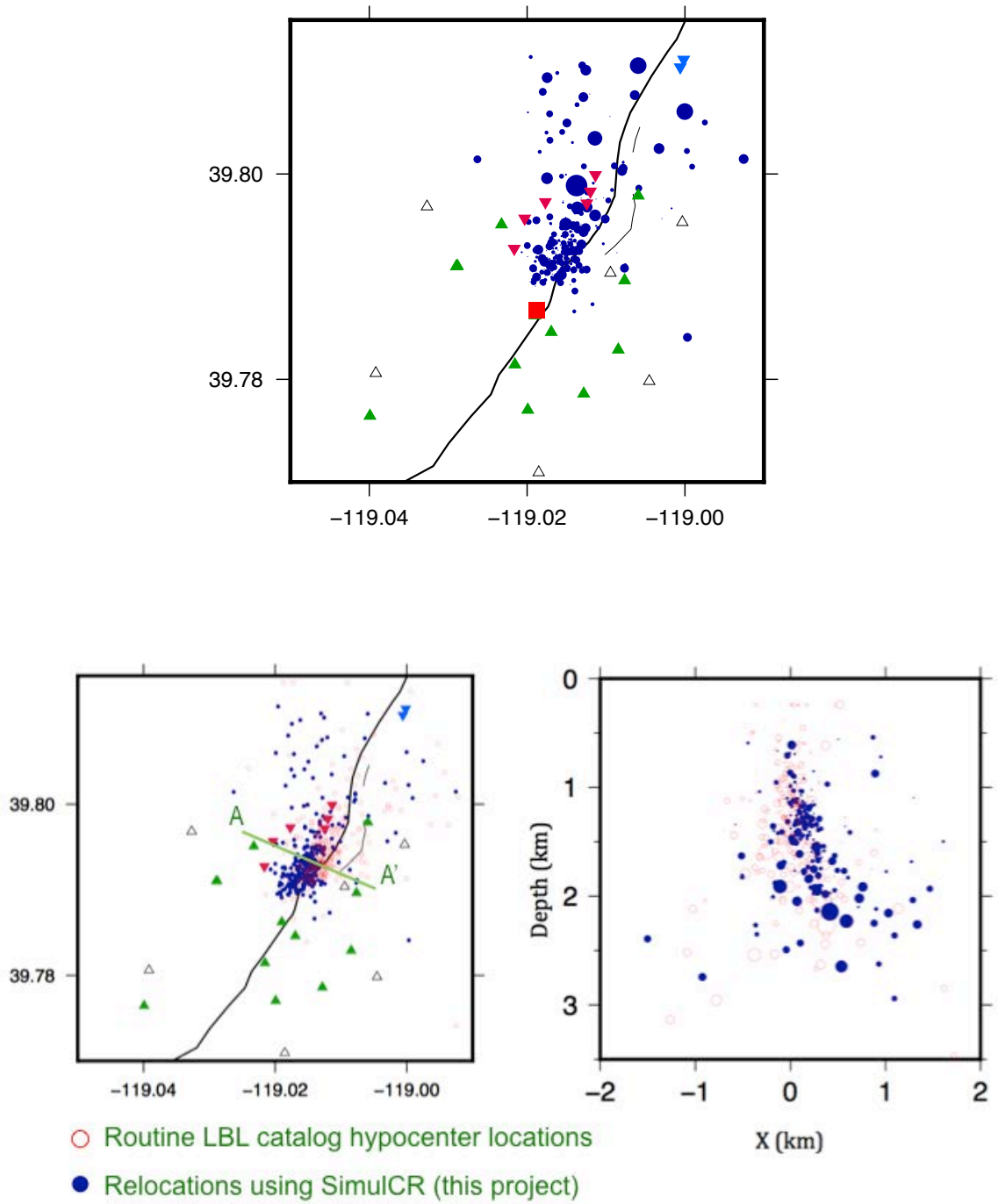

***Figure 3.1-17**: (top) Map view plot using GMT5 of microearthquake locations for the period December 2010 - June 2014 from a simultaneous inversion for 3D velocity structure and hypocenter location using the program SIMULDD. Earthquakes are scaled by magnitude. (bottom) Comparison of original hypocentral locations versus relocated MEQ catalog.*

Step 3: Compute Focal Mechanisms and Stress Drops (Subtask 2.3)

Focal Mechanism by Waveform Modeling: We use the package mtinvv3.0.3 to model the waveforms using a semi-analytic approach. While fast, this method requires a layered velocity model, which may not be adequate for the Brady's structure at the frequencies required to match small (magnitude < 3) earthquakes. This presents a substantial problem and impacts the results.

Rather than using a standard inversion, a grid search is performed over all possible combination of strike, dip, rake, and depth for each component using a location from the previous step (Step 2, Subtask 2.2). This approach makes uses the programs mkgrnlib to generate the Green's functions for a range of distance and depths and grnlib2sac to generate a particular synthetic. A misft (L2 norm) is calculated between the bandpass filtered recorded data and the synthetic. It is also possible to include first motion data. The automatic creation of the synthetic, the grid search, and the comparison is conducted by a python program named *grid_mom.py*.

The focal mechanism analysis is conducted in the following steps:

3.1. Create the velocity model by extending the 1D model derived from ambient noise tomography to deeper layers based on a regional model.

3.2. Select an earthquake having a well-constrained location inside the network and that was recorded on all three-components with high signal-to-noise.

3.3. Extract a window of data around the event.

3.4. Create Green's function for the distance and depths to each station.

3.5. Run the grid search which calculates all possible focal mechanisms and compares the synthetics with the observed data (Figure 3.1-19) and plot the focal mechanism (Figure 3.1.20). Results are written out as a text file with strike, dip, and rake and the associated error.

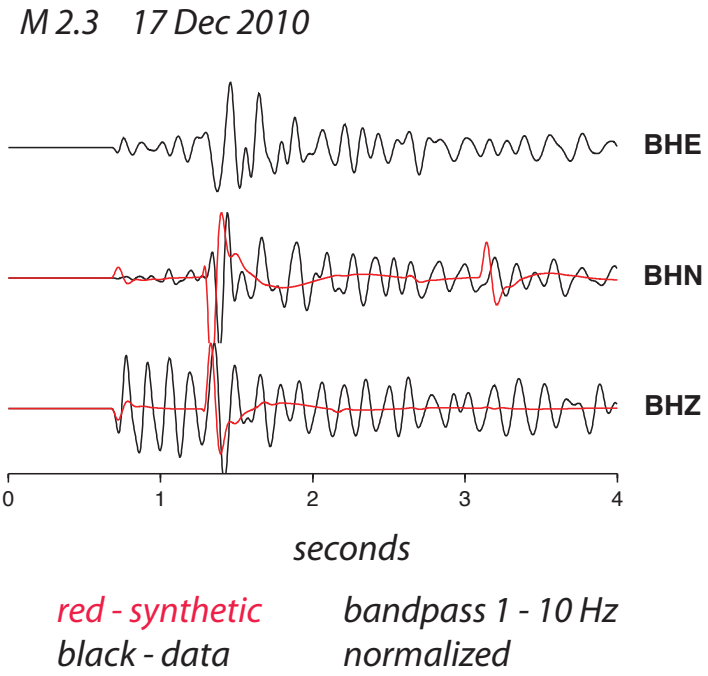

Figure 3.1-19: *Data (black) and synthetic (red) for best-fitting model (strike:320, dip:70, rake:20).*

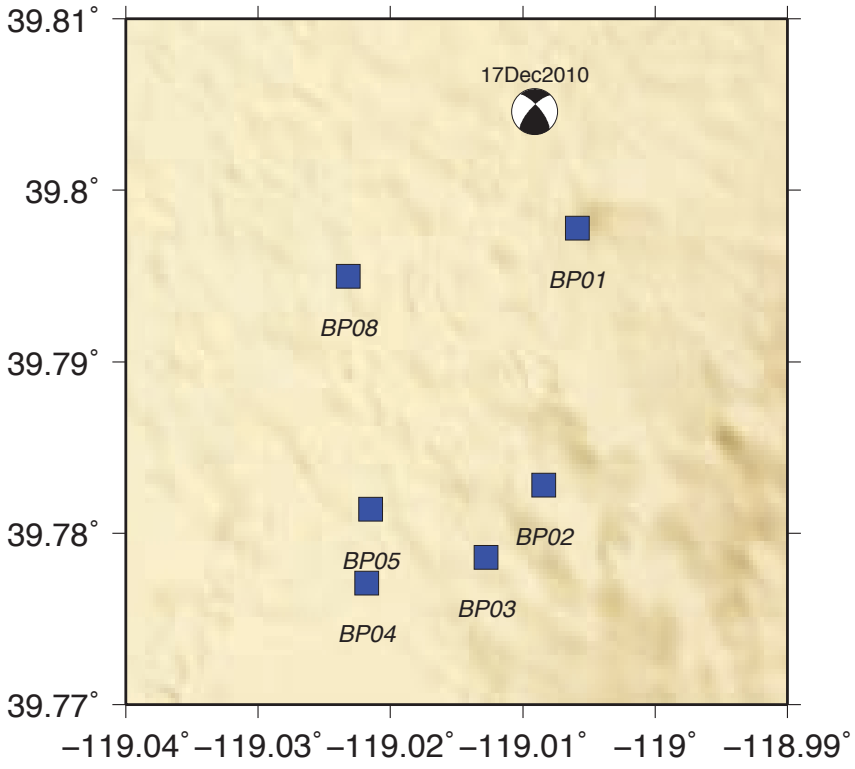

Figure 3.1-20: *Map showing focal mechanism.*

Finite difference synthetic seismograms: In an attempt to resolve the problem with the simple layered model we also used a more complicated model and a finite difference algorithm to generate synthetics but this is impractical for a grid search. Although not implemented here, this algorithm can handle 3D variations in velocity. The synthetics did appear more similar to real data at high frequencies (Figure 3.1-21), applied to the same event as in Figure 3.1-19 and 3.1-20) but the velocity model at the time of the analysis is too crude for accurate representation at high frequencies.

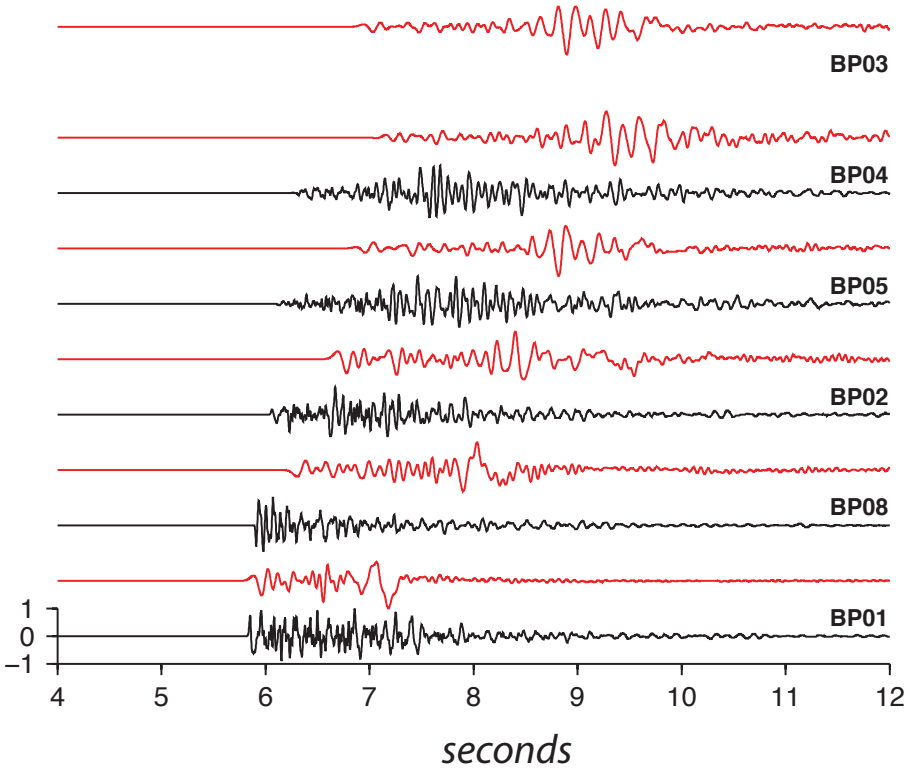

***Figure 3.1-21**: Synthetic seismograms calculated using the finite difference algorithm compared with recorded data.*

APPENDIX: Updated Section 2.3: Reservoir Modeling

2.3 Reservoir Modeling (SOPO Task 3)

Task 3 models subsurface reservoir characteristics constrained by the surface deformation field (Task 1), subsurface deformation evidenced by microearthquakes (Task 2) and the pumping history in conjunction with geological constraints.

Surface deformation and seismicity result from stress changes at depth induced by the dynamic response of the reservoir to pumping. The intent of the geomechanical model is to infer the parameters to define such a model consistent with constraints from pumping records, surface deformations, and seismicity.

This section describes SOPO Subtasks 3.1, 3.2, and 3.3, which together comprise the streamlined geomechanical modeling (Subtask 3.4).

In developing the software tools and applying them to the geothermal field at Brady Hot Spring Nevada, the key observations to explain are: (1) the localized surface subsidence in the vicinity of both production and injection wells and (2) position of seismicity. Additional constraints are obtained from the time history of pumping and temperature records indicating net fluid and heat loss, respectively, from the reservoir. Inspection of these compiled data sets indicate that the timing of swarms of seismicity roughly correlate with observed fluid pressure fluctuations in the reservoir in their vicinity. Our primary goal is to improve the definition of the permeable reservoir, including identifying necessary connections among geologic structures and wells. The primary result of this assessment is the location and magnitude of volume change at depth corresponding to the reservoir volume perturbed by pumping activities. A secondary goal is to relate this improved reservoir model to the seismicity to better understand how seismicity correlates to regions of fluid flow, which in this case are regions that experience pressure change (or volume change). The second requires an improved rheologic characterization of the reservoir.

To start we evaluate the correlation between subsidence and the geometry and volume change of a reservoir at depth by building on the results of Task 1 (Figure 2.1-1). We use the simplest geomechanical model assumption of a homogeneous elastic half space in which deformation results from a rectangular dislocation with defined position, length, width, strike, dip, and volume change. This parameterization is implemented for modeling individual interferometric pairs (Step 2 of InSAR work flow; SOPO Sub Task 1.5). The elastic model fits the InSAR data to within several millimeters per year, as measured by the RMS scatter of the residual rates of range change. This approach serves two purposes: (1) it improves the assessment of the surface displacement field (as described in the workflow of Task 1) and (2) provides an initial basis for assessing the poroelastic, thermoelastic, or other behavior of the reservoir consistent with the surface deformations. In particular, the simple model enables efficient exploration of a wide range of the parameters defining the reservoir volume. Sensitivity to these parameters and thus the uniqueness of the best fitting model model is defined by the RMS residual between the model and the observed surface displacement field.

In the prototype software, this elastic modeling module (Step 2 of Task 1 above) can be interpreted as a zeroth order approximation of a more general theory of poroelasticity or thermoelasticity. For example, in the poroelastic case, one could apply the following scaling relation [from equations (2) and (3) from *Lu et al.*, 2002]

$$\Delta V \cong \Delta P_f V c_m$$

where ΔV is the change in volume from elastic modeling, ΔP_f is the fluid pressure change, V is the poroelastic volume affected, and c_m is a poroelastic modulus, a rock mechanical property that is approximately equal to the compressibility. The same volume change is produced in a poroelastic medium by the product of the three terms on the right-hand side of the equation.

Essentially, the equation provides a means of assessing the consistency of the observed behavior with a poroelastic or thermoelastic coupling.

Downstream in the work flow, forward modeling in "the physics of the forward modeling module" in Step 3 (Subtasks 3.2 and 3.4) and "inverse modeling module" in Step 4 (Sub Task 3.3) will typically require geomechanical models that implement coupling between the mechanical stress field and the fluid pressure and/or temperature fields or between volume loss and chemical dissolution to explain the observed deformations and satisfy the geologic boundary conditions of a particular reservoir. The prototype software tool can be used to calculate the 3-dimensional stress tensor at any location in the geothermal field, and thus evaluate the Coulomb failure criterion on fault planes known from: (1) structural geology/borehole observations (Subtask 3.1), (2) stress models (Subtask 3.1), and/or (3) the earthquake hypocenters (Subtask 2.2) and focal mechanisms (Task 2.3). In the future seismic tomography such as that derived from the analysis of ambient noise could also be compared to results from the poroelastic model.

We have developed and applied both elastic (dislocation) and poroelastic (finite element) modeling tools. The elastic tools have been rigorously applied to model the surface displacements and are appropriate to model both the time-history of subsurface volume change in the Brady test case based on the resolution of the data; they are also appropriate to model the deformation outside a confined reservoir volume undergoing deformation. Deformation in the volume can be approached through poroelastic finite element.

Our results primarily implement elastic solutions, as this allows us to efficiently address three critical issues: (a) the geometry of the reservoir volume (Ali et al., 2016, Reinisch et al., 2018); (b) to test several plausible alternative hypotheses for the source of subsurface volume change (Ali et al., 2016, Reinisch et al., 2018); (c) seismicity associated with reservoir management (Cardiff et al., 2017). The approach is to solve for subsurface volume changes necessary to explain surface deformations, then test the viability of different mechanisms for generating the necessary volume change in an otherwise elastic half-space. Therefore, we have chosen to use the term "geomechanical" modeling in this report to generalize the "poroelastic" modeling described in the SOPO.

2.3.1 Workflow Outline

Steps in this analysis build directly on the constraints derived from surface deformations revealed from InSAR (Task 1) and summarized in Section 2.1. As a result, the steps in the workflow are a progression of the InSAR (Figure 2.1-1). This reflects the use of spatially and temporally rich data set provided by InSAR that in concert with geologic and pumping data provides strong constraints on reservoir characteristics. Additional constraints from seismicity (Task 2) summarized in Section 2.2 provide a post-assessment of fit of the geomechanical model and the basis for model revision.

Geomechanical analysis:

Following results generated by the InSAR analysis:

Step 1*: Assemble geological and rock mechanical constraints (Subtask 3.1)*

Step 2*: Geomechanical modeling (Subtask 3.2) including testing the best-suited rheological models for the behavior observed at Brady Elastic (Poroelastic/Thermoelastic)*

Step 3*: Inverse modeling of SAR data using elastic models (Subtask 3.3 and 3.4).*

Step 4*: Coulomb stress change calculation/analysis (Subtask 3.5).*

***Step 5**: Integrate surface deformation + MEQ as test*

Steps 3 to 4 to 5 can be assessed iteratively to improve the model fit or test the deformation mechanisms critical to describing the behavior at Brady.

Each step of the workflow involves use of software. URL's for the source code is included in the descriptions.

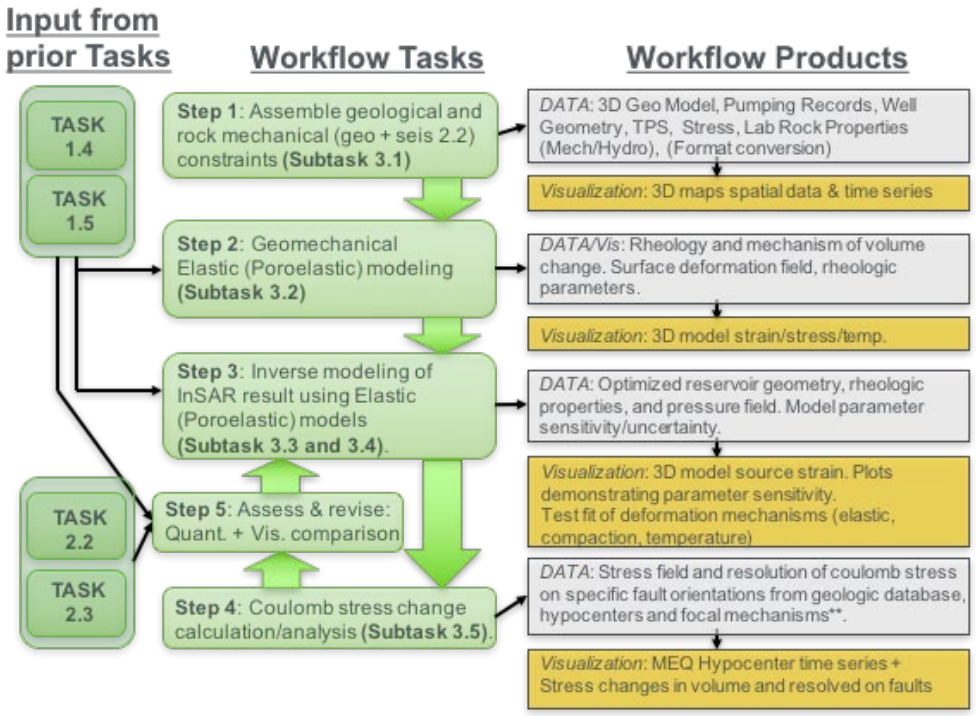

***Figure 2.3-1:** (a) Summary of steps in the workflow starting with the geologic constraints and analysis of deformation in Tasks 2 and 3 to a geomechanical model compatible with pumping records.*

2.3.2 Workflow Description

Step 1 (Subtask 3.1) - Assemble Geologic and Reservoir Database

Several distinct data sets are assembled to constraint the geologic, mechanical, and hydrologic properties of the Brady geothermal field to inform the geomechanical model. These data provide model boundary conditions, as inputs such as initial estimates of mechanical or hydrologic properties, and as tests of model predictions.

- A geologic model developed in EarthVision by Egbert Jolie in collaboration with Jim Faulds and Inga Moeck (Jolie, 2014; Jolie et al., 2012, has been incorporated into the project. This database includes a 3D fault and stratigraphic model (Figure 2.3-2). Additional data on hydrothermal features is also available.

- The local digital elevation model has been built for the study area.
- The Great Basin Center for Geothermal Research (pers comm. Jim Faulds, 2011) has shared ArcGIS data that documents the faults and stratigraphic units as mapped by Jim Faulds and others (Faulds and Garside, 2003; Faulds et al., 2010; Faults et al., 2011) and surface hydrothermal features (Coolbaugh et al., 2004). In addition, ORMAT has shared details of the wells associated with the reservoir (Figure 2.3-3).
- As part of this project, ORMAT has provided a comprehensive record of daily pumping activity from 2004 through 2014 including line pressure, flow rate, temperature, and some downhole pressure recordings for both injection and production wells (Figure 2.3-3).
- This project has worked in close coordination with the Bradys EGS project to stimulate well 15-12ST1 in 2013. The database developed as part of that project has been incorporated here and includes well surveys limited geophysical logs, rock mechanical/hyrdrologic/mineralogic/thermal properties from corehole BCH-3 (Lutz et al., 2011) as well as cuttings from other wells, and a stress model derived in 15-12ST1 from image logs, geophysical property logs, a mini-frac, and an update based on stimulation behavior (Figure 2.3-4).
- Similar data are also available from the nearby Desert Peak Geothermal Field and EGS site of well 27-15 just 5 to 7 km east, which is hosted in a similar structural and geologic setting (e.g., Davatzes and Hickman, 2009; Hickman and Davatzes, 2010; Lutz et al., 2010).

These data have been assembled within a cloud database accessible to all project participants, and file formats appropriate to each workflow are available. In addition, scripts have been written to convert data formats and enforce common datum and reference frame among spatial data sets. Matlab scripts are used to import these data files from their native formats and visualize the resulting data (maps, 3D volumes, time series) or convert them to formats necessary for workflows in Tasks 1, 2, and 3; these plots and data files can be updated by simply inserting updated source data files. Additional visualization is accomplished via EarthVision as well as the open-source ParaView (http://www.paraview.org) softwares. Directories for the Seismic and SAR data are also established.

The Matlab tools developed to: (a) import and analyze the reservoir data; (b) visualize the geological data; (c) import and optimally mesh the fault model outputting formats to feed SYNEF (or Poly3D); (d) resolve tractions onto the fault model from stress fields generated by Task 3.4; (e) import and visualize surface deformation from Task 1; (f) import and visualize earthquake distribution from Task 2; (g) import and visualize deformation or stress field from SYNEF (or Poly3D) model outputs. These tools are provided as two distinct modules in the workflow and both tools have been passed to ORMAT as part of the compiled BradyEGS database; ORMAT has released essential data sets to the GDR. (Note that a parallel set of tools been derived and extended from this work by the PoroTomo project who has submitted many modules to the GDR).

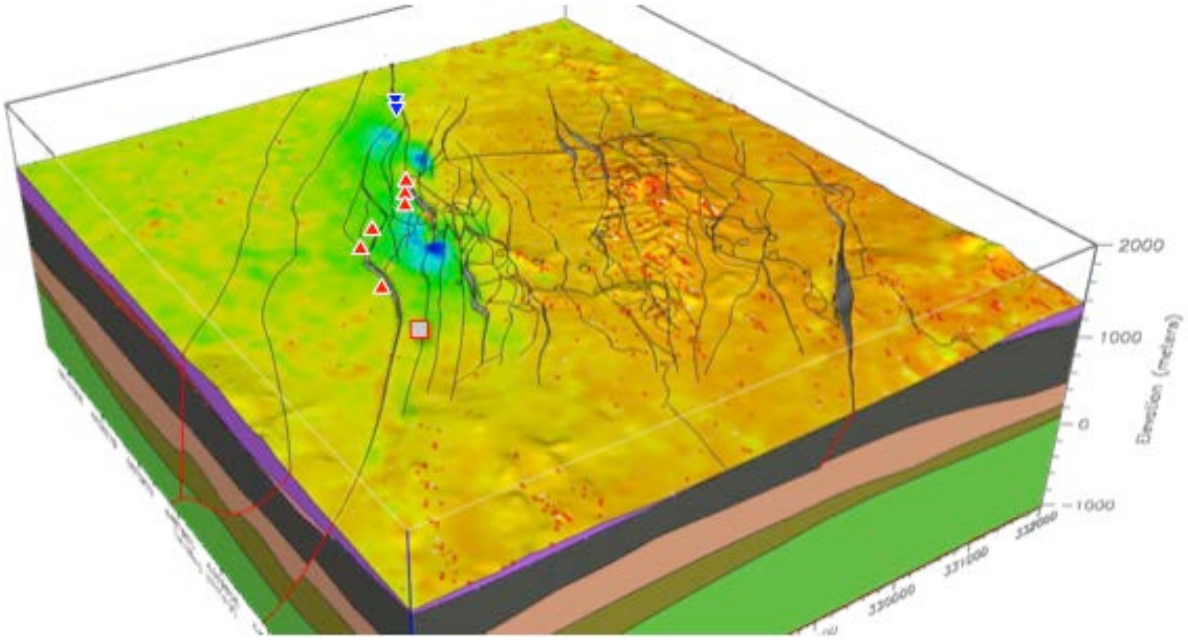

Figure 2.3-2: *3D geologic model including faults and rock formations and wells based on work by Jolie (2014).*

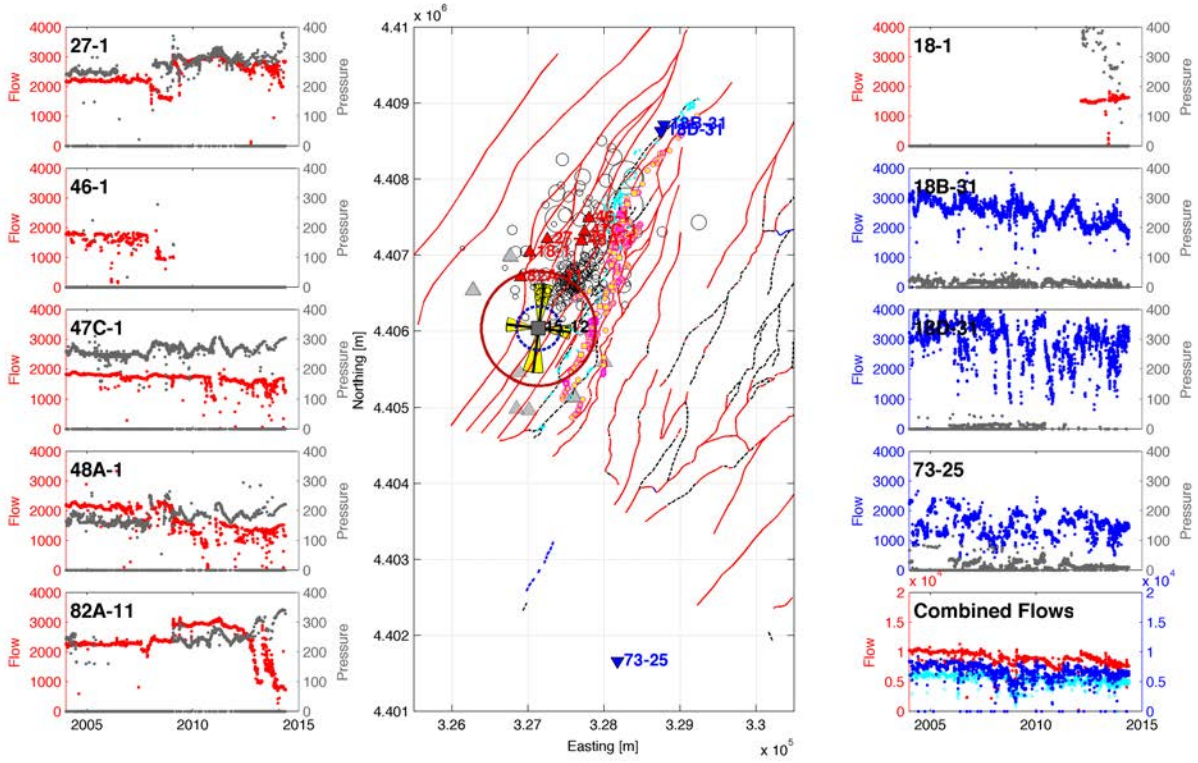

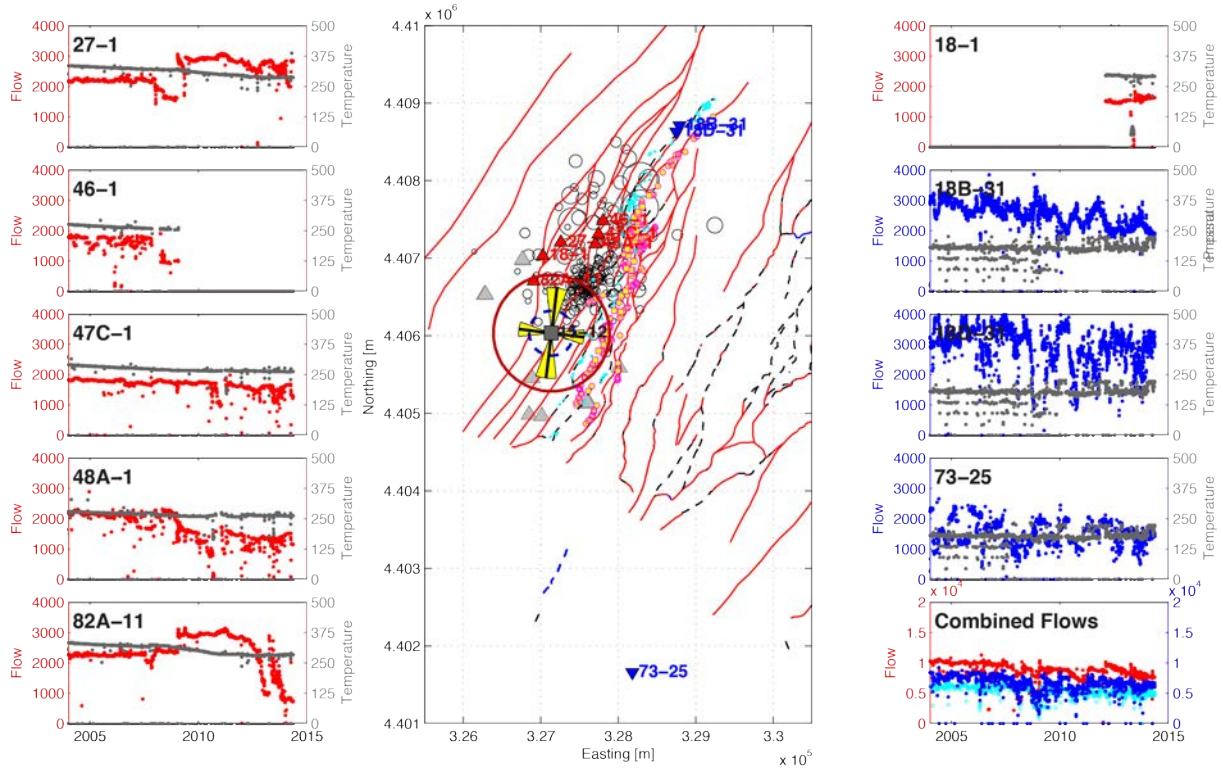

Figure 2.3-3: *Assembled pumping records including well position (production = red triangles, injection = blue triangles), seismometer stations (gray triangles), geologic faults (red and black lines), the stress model for 15-12 and 15-12ST1 (at gray square: outer red circle = Sv, inner blue circle Pf/Sv, and inner black lines the azimuth+/- one standard deviation and relative magnitudes of SHmax/Sv and Shmin/Sv respectively), hydrothermal features (red bordered yellow squares), and seismicity scaled to magnitude (black circles). (top) Plot showing the timeline of pressure and flow rate by well. (bottom) Plot showing the timeline of temperature and flow rate by well.*

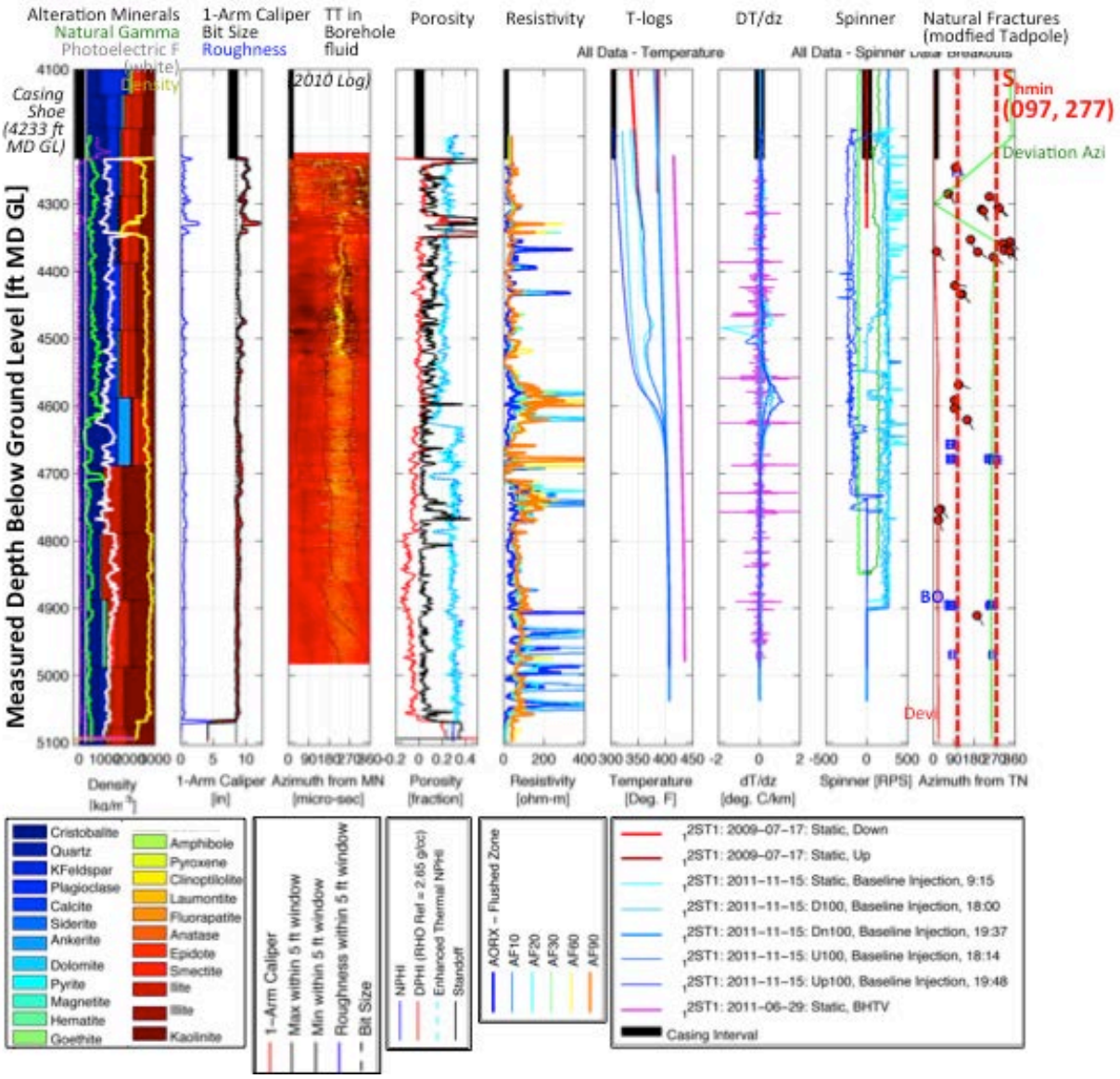

Figure 2.3-4: *Example Borehole Data, panels from left to right are: (1) Cuttings mineralogy with natural gamma and density overlain, (2) 1-arm caliper log, (3) borehole televiewer amplitude log, (4) porosity logs, (5) resistivity logs, (6) temperature surveys, (7) local temperature gradient derived from temperature surveys, (8) spinner, (9) and natural fractures (where the dots are the dip direction and the tails the dip angle from horizontal), induced structures interpreted from the image log (note that this well is deviated so the position of induced structures is complexly related to the borehole deviation and the remote stress tensor), and the average azimuth of Shmin.*

Step 2 (Subtask 3.2) Geomechanical Forward Impulse and Response Modeling - Geomechanical modeling due to coupled poroelastic or thermoelastic processes: In order to simulate deformation, following injection and extraction of fluids we have extended an in-house, fully unstructured, parallel finite element code for modeling crustal deformation due to earthquake and volcanoes. The code is open source and can be downloaded from http://code.google.com/p/defmod. The current version includes support for elastic, viscoelastic, poroelastic and poroviscoelastic rheologies. It allows a user to simulate deformation due to pressure changes following injection and/or extraction of fluids from saturated subsurface

reservoirs. Because the thermoelastic problem is exactly analogous to the poroelastic problem (e.g., see Wang, 2000), the code can also be used to simulate deformation due to cooling or heating of rocks, by simple scaling of variables. Both problems in essence are 'deformation-diffusion' problems.

To use the code, the beta user must first create a mesh, ideally from a geologic model, assign poroelastic (or thermoelastic) material properties for all elements, impose mass (or heat) flow rates, boundary conditions etc. This information must be specified in an input file. A sample file is available with the source code. Once the input file is ready the simulation can then be performed.

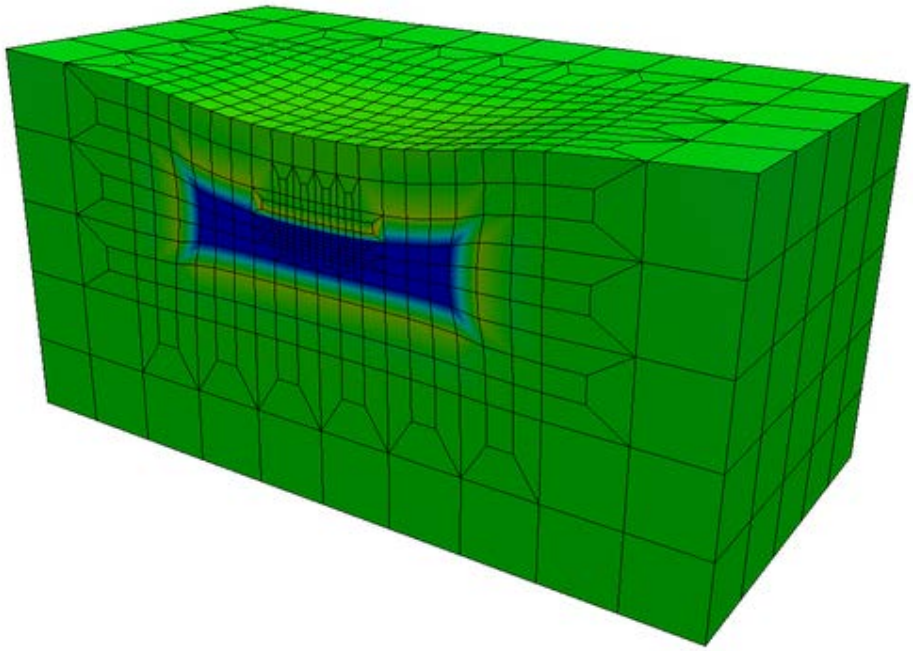

Figure 2.3-5*: Reservoir compaction, following extraction of fluids from a confined reservoir. The deformation has been greatly exaggerated.*

For example, Figure 2.3-5 above shows deformation and pore pressure change (in color) due to extraction of fluids from an idealized, confined, reservoir. For thermoelastic problems the color would represent change in temperature. The most appropriate geomechanical model to assess stressing and pressure change in the reservoir depends on the mechanism of volume change contributing to the surface deformations revealed by InSAR, and thus will vary on a case-by-case basis. This issue is further addressed in Section 3 concerning the scientific results derived from analysis of InSAR. A goal of this project is to develop geomechanical modeling framework that address key physical processes. In Phase II, we will add implementation of thermoporoelasticity.

Step 3 (Subtask 3.3 and 3.4) - Inverse modeling of InSAR data using fully numerical geomechanical models: The inverse modeling procedure described in Step 2 of Task 1, used computationally inexpensive, semi-analytical models (Okada, 1992; Mogi, 1958). These models can very easily be replaced by fully numerical poroelastic or thermoelastic models such as one described in Step 4.

However, because the fully numerical models are computationally expensive, the number of parameters that can be estimated are typically less then 10-20. For a large number of parameters, methods based on adjoint state theory (e.g., Cardiff and Kitanidis, 2008; Cardiff, 2010) are more appropriate. In either case, the optimization will also provide information on the relative uncertainty and importance of key model parameters.

For example, Figure 2.3-6 shows the optimized model that reproduces two of the largest subsidence bowls observed in the interferogram shown in Step 2. In this example, the only free parameters in the model are those associated with the geometry of the reservoir; the only observations used are those from InSAR. For a thermoelastic problem the deformation will be due to temperature changes instead of pressure change.

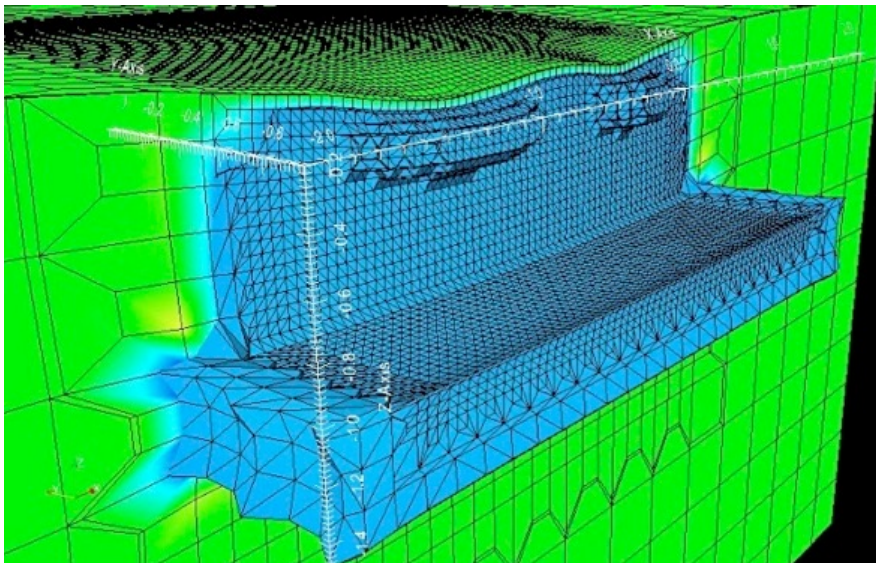

Figure 2.3-6*: Optimized model for Brady Hot Springs showing pressure change (color) and the (deformed) mesh (black line). Deformation occurs due to pressure drop both in shallow and deep reservoirs that are connected by an vertical fault. The deformation has been greatly exaggerated. The pressure or temperature change required to cause the deformation depends on the mechanical properties of the rock. For example, pressure required to deform a rock with shear modulus of 30 GPa will be ten times lower for a rock that has a modulus of 3 GPa.*

Step 4 (Subtask 3.5) – Relate deformation field to earthquakes and geological structures: SYNEF (with alternative, poly3d) and DefMOD.

We have explored three different software tools to model deformation in and outside the reservoir. **SYNEF** is an open-source tool that implements elastic dislocations. It is used to derive the stress and deformation field around the deformation sources inferred from GiPhT in Task 1, and is the primary tool utilized in our workflow. An alternative implementation with a full suite of supporting scripts has been implemented for Poly3D (Thomas, 1999). In addition to modeling the resulting dislocation sources from GiPhT, this tool has been applied to model slip on the Brady Fault system and as well as tractions resolved on these faults (detailed documentation is provided in the Appendices to Laboso, 2016). Poly3D is available for academic use, but for commercial applications it is owned by IGEOS, a Schlumberger Subsidiary. Finally, DefMod (Ali, 2015; Meng, 2016) is a multiphysics finite element tool suitable for modeling deformation in the reservoir. Although developed and freely available, this tool turned out to be less useful for understanding the reservoir-scale deformation field hosted within the quasi-planar fault system at Brady.

DefMod: Coulomb stress change calculations: Once we have a calibrated model (either elastic, poroelastic or thermoelastic) we can use it to calculate Coulomb stress changes on fault planes. These calculations are useful for studying induced seismicity. The code for calculating Coulomb stress changes is available from: http://defmod-utils.googlecode.com.

Instructions on how to model deformation and calculate the stress changes are available in the README file.

For example, Figure 2.3-7 shows Coulomb stress changes from an Okada model. However, results from finite element models described in Step 4 can also be used. A user simply specifies a stress tensor (Eij,Ekk), friction coefficient and the receiver fault orientation, such as that derived from the geologic model (Subtask 3.1) or focal mechanism solution (Subtask 2.3) to the calculator. Typically MEQ focal mechanisms are used for orientations. However Coulomb stress changes can also be calculated at "optimally oriented" faults.

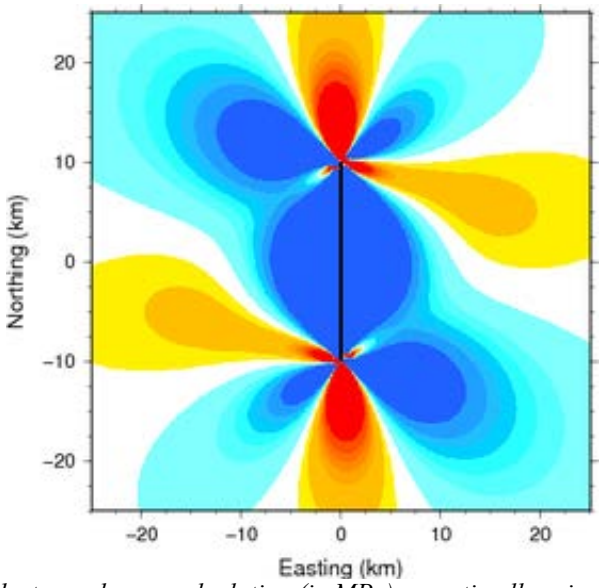

***Figure 2.3-7**: Sample Coulomb stress change calculation (in MPa) on optimally oriented faults.*

SYNEF is a general-purpose Fortran code that was originally developed to model displacements and tilts at the surface and in the interior of a linear elastic half-space caused by point or finite volumetric (dilatation/contraction), opening/closing crack (Mode I) and shear dislocation sources (e.g. Ramirez and Foxall, 2014). In addition to specifying volume change or opening displacement, respectively, volumetric and Mode I source deformations can also be driven by pressure changes using a poroelastic formulation. (Temperature effects are not presently considered, but a thermoelastic formulation could similarly be implemented.) The code uses the linear elastic half-space Green's functions developed and programmed as Fortran subroutines by Okada (1985, 1992). In addition to displacements at specified points in the half-space, the subroutines output displacement gradients, from which the full elastic strain tensor can be calculated.

In the extension of the code, the stress tensor is calculated from the strains at points on fault planes having specified geometries (strike and dip) using estimated local elastic moduli. The stress tensor at each fault point is transformed to principal stress coordinates, and the

changes in shear and normal stresses resolved on the fault plane having defined strike, dip and rake (slip vector direction). From these calculations the Coulomb stress can be determined as

$$\Delta\sigma_c = \Delta\tau + \mu\Delta\sigma_{\text{eff}},$$

where $\Delta\tau$, $\Delta\sigma_{\text{eff}}$ are the changes in the shear and effective normal confining stresses, respectively, resolved on the fault, and static friction, μ. According to this definition, an increase in Coulomb stress will move the fault closer to shear failure; i.e. closer to slipping. In the present application, the stress changes at the fault are induced by remote sources of deformation, and the shear displacement is assumed to be manifest as microseismicity. Therefore, all else being equal, we would expect that increased microearthquake activity would be most likely to occur along segments of a fault where remote activity increases the Coulomb stress. As of this report, this implementation including an example data set is available to team members in the cloud drive, but has not been made freely available via GitHub.

At Brady, the code is used to calculate Coulomb stress changes on faults within the Brady fault zone caused by Mode I deformation modeled during Phase I as the sources of surface displacements measured by InSAR (Ali et al. (2016). At present, time-dependent poroelastic effects are not considered in computing changes in effective confining stresses at the faults. The resulting changes in Coulomb stress are mapped in 3D within the fault zone, and compared with the microearthquake locations to assess the possible contribution of remote stressing effects to slip-related changes in flow within the fault zone/reservoir.

The calculated stress changes are induced by deformation in the shallow subsurface resulting from physical processes within the geothermal reservoir, as described by Ali et al. (2016). SYNEF also calculates the full stress tensor in global (east, north, up) coordinates and principal stresses throughout the 3D elastic half-space surrounding the reservoir, from which hypothetical fault orientations that are most favorable for shear slip – and hence the most likely sources of microearthquakes – can be derived at arbitrary locations. During Q4 we incorporated the Ali et al. (2016) deformation sources and estimates of local elastic and fault frictional parameters in the input. Fault geometries will be added and the full stress simulations will be completed in FY18 Q1. The calculated Coulomb stress changes on defined faults (and at other locations) will then be compared with microearthquake locations. The primary objective is to assess the possible contribution of stressing effects from reservoir-related deformation to slip-related changes in flow within the fault zone and elsewhere within the reservoir.

We note here that synergistic work on this project has extended these methodologies and also demonstrate effective transfer of the technology. Ali et al (2018) and Liu et al (2018) recently applied several of the approaches developed in this project to Raft River in Idaho. Reinisch et al. (2018) and Reinisch et al (2020) extended the dislocation approach to approximate volume loss three orthogonal directions defining voxel-like elements and using a grid of these elements to map volume losses at the Brady Geothermal field and the Coso Geothermal System in California. Finally, Meng (2016) have used Defmod to model episodic fault rupture with multiphysics, including rupture related to induced earthquakes.

Step 5: Assessment and Revision of Model Predictions/Hypotheses: Once the model results are generated and visualized, they can be compared to independent constraints from Task 1, 2 or Subtask 3.1 (e.g., Figure 2.3-8) or relate the modeled local stress state accompanying reservoir deformation and resolving it onto faults in the reservoir (e.g., Figure, 2.3-9). This evaluation is particularly relevant to assessing what mechanism of deformation, and thus rheology, is most

appropriate to characterize the reservoir response to pumping. In addition, other model constraints such as the mechanical properties, the geologic units, and model complexity can be updated as well as updates from additional data. This assessment and adjustment step is also particularly relevant as model predictions can guide acquisition of new data, drilling of new wells, or stimulations, which further test the model predictions and could require model revision. Both the assessment steps and the visualizations of these assessments are provided via a toolbox of purpose-made MATAB® scripts. Example workflows to conduct the model and visualize these results have been built (e.g., Figures 2.3-8 and 2.3-9).

In this step, the seismic response of the reservoir is particularly important. The correlation between the geomechanical model and seismicity is partly addressed in Step 7 through the considerations of hypocenters and focal mechanisms relative to modeled stresses. In addition, seismic tomography either inverted from the MEQ catalog or through the ambient noise analysis can be considered for compatibility. We also consider both the *occurrence* and *absence* of MEQs, especially as the discrepancy between areas predicted to be stressed to seismic failure and the absence of seismicity is significant.

These tests and comparisons will require updating of the geomechanical model to improve correlation between the model and the available constraints.

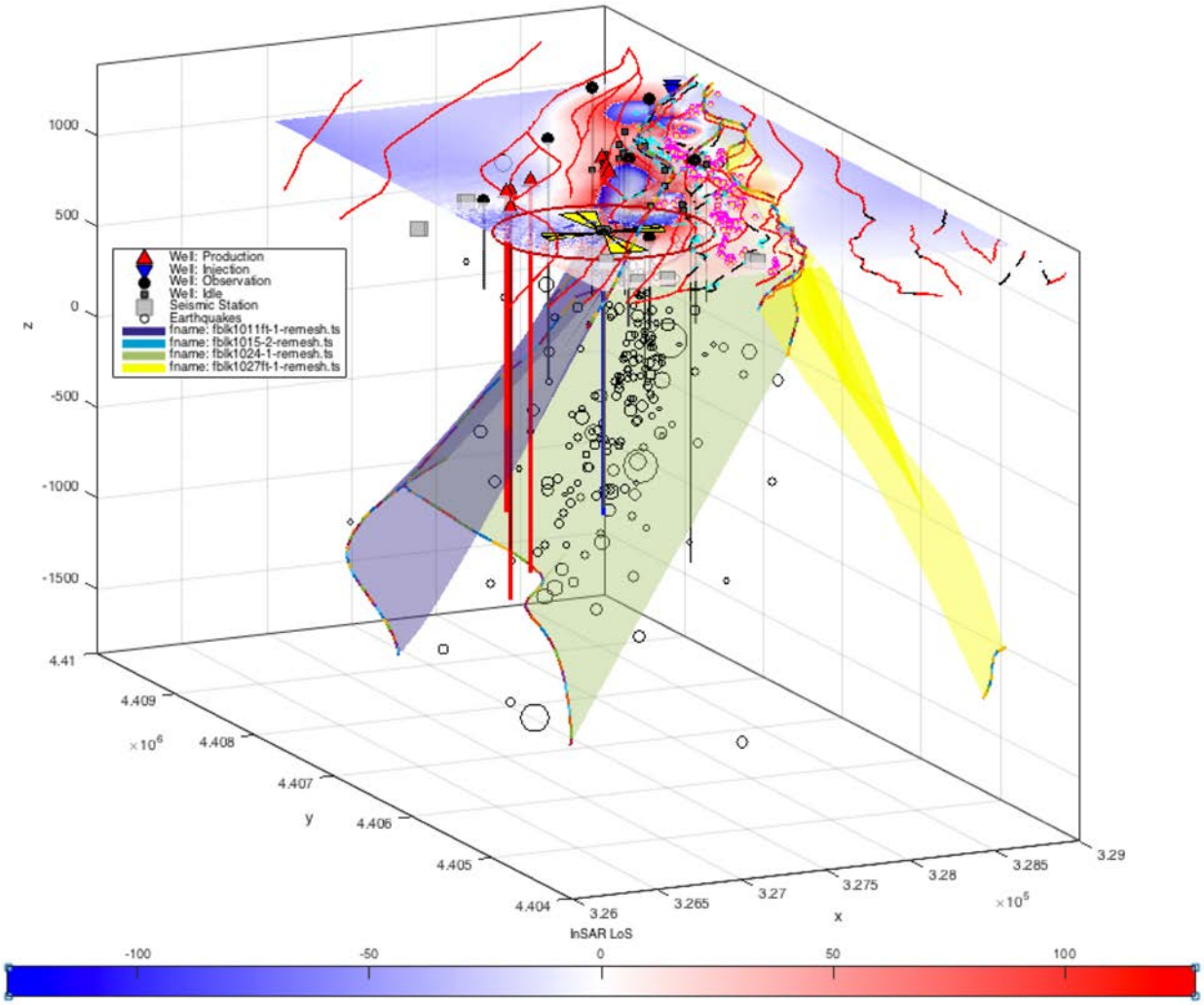

Figure 2.3-8: *Compilation of geologic data (Subtask 3.1) including wells, surface displacement field (Task 1 result), relocated seismicity (Task 2 result), surface hydrothermal features (magenta, yellow-filled squares), mapped faults and selected faults from the geologic model by Jolie (2014) that bound or coincide with seismicity and the distribution of wells.*

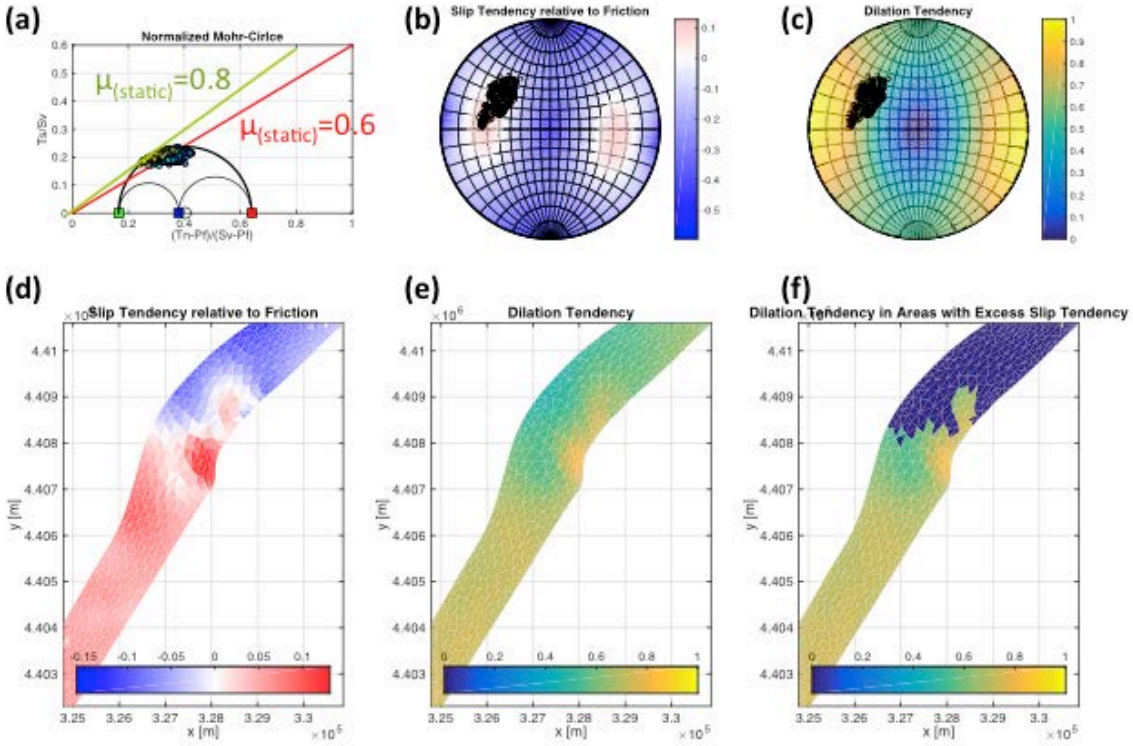

Figure 2.3-9: *A simple analysis using the stress model from 15-12ST1 from subtask 3.1 suggests these faults are critically stressed for friction coefficients up to ~0.8. (a) Mohr-Coulomb plot of tractions resolved on elements defining the fault surface. (b) Equal angle stereonet of slip tendency defined as ST=Ts/(Tn-Pf). This plot is modified to show the anomaly defined by ST-0.6, so that positive values indicate attitudes stressed to failure for a coefficient of static friction of 0.6. (c) Equal angle stereonet of dilation tendency defined as DT=(σ_1-Tn)/(σ_1-σ_3). (d) Variation of slip tendency on the fault surface. (e) Variation of dilation tendency on the fault surface and (f) dilation tendency on fault surface where slip tendency exceeds the static frictional strength of 0.6. This tool allows any stress state sampled at the element centroids to be assessed and visualized.*

APPENDIX: PyWCC Description

Subtask 2.1-2.2: Advanced detection via template matching:

The catalog of microearthquake location derived from simultaneous inversion of triggered waveform data for the period November 13, 2010 to March 24, 2015 was finalized in July, 2015 and uploaded to the GDR as one of the Porotomo project submissions. In coordination with LLNL, we finalized a format for the Brady earthquake catalog that accommodates hypocenter location data from both LBNL simultaneous inversions and from LLNL PyWCC analysis (see below). Absolute horizontal and vertical hypocenter location uncertainties from the simultaneous inversions are now included in the catalog.

A database was created at Lawrence Livermore National Laboratory (LLNL) with a common directory structure, file naming convention and metadata header information for the combined Brady Hot Springs Taurus (11-station) and Reftek (6-station) seismic networks. The data currently available at Lawrence Berkeley National Laboratory (LBNL) and LLNL is documented in Table 1. Although there is some overlap in time, data can be conceptually subdivided into Generation 1 and Generation 2 seismic networks. For correlation purposes, the data between the 1st and 2nd generation networks are not compatible since the sensor depths were moved.

PyWCC is a Python tool for seismic waveform cross-correlation (PyWCC) that interrogates continuous recorded data to search for earthquakes with too small to trigger recording. This python program that uses the ObsPy, numpy and scipy modules to cross correlate known master template events with the continuous seismic data to identify smaller events missed in the original earthquake catalog due to problems with, for example, poor signal-to-noise ratio in the observed waveforms.

PyWCC version 0.1.1 computes seismic waveform cross-correlation on single- or multiple-component seismic data across a network of seismic sensors. PyWCC correlates symthetic waveform data templates with continuous seismic data, associates the resulting detections, identifies the template with the highest cross-correlation coefficient, and outputs a catalog of detections above a user-defined absolute cross-correlation threshold value. A note on the correlation: PyWCC computes cross-correlations in the frequency-domain for increased computational speed. The program package includes documentation on how to configure and run the code, a short tutorial, and a worked example with associated test dataset based on the permanent Bradys seismic network data. The program package is released for outside distribution through LLNL review and release procedures (https://www.osti.gov/biblio/1379475-python-waveform-cross-correlation). The software is publicly available at https://github.com/templetond/pywcc.git.

Required inputs to the program include the continuous data, a station text file, a master template text file, and a program input text file. As mentioned previously, a subset of the continuous data is held by LLNL and LBNL as well as the Bradys station location files, which is also available in the GDR. For convenience, a training data set is included the GitHub release. The full continuous data remains locally hosted at LLNL, LBNL; the relevant catalog of triggered events is available in the GDR and from the Northern California Seismic network. The earthquake catalog improved relocated earthquake catalog resulting from Phase 1 of this project for events between 12-10-2010 to 06-13-2014 was used to create the master template file.

The output of the program is a text file listing all the new events found in the seismic data stream that were missed in the original seismic catalog, the master event that it was matched with, and the cross-correlation coefficient between the new event and the master event.

Analysis results

SubTask 2: From an earthquake catalog provided by LBNL, 59 events that occurred in between 03/02/2014 and 06/10/2014 were identified as template events suitable for cross-correlation. Template events are previously identified earthquakes that have good signal-to-noise in the frequency band of interest to the study. These 59 events were cut from the continuous data and put into the example directory that will be distributed along with the PyWCC source code distribution.

SubTask 3: Advanced microearthquake detection using matched filter correlation techniques supplied by the PyWCC python module was performed on one month of continuous seismic data (04/01/2014 to 04/30/2014) using the 59 pre-determined templates from SubTask 2. In the original catalog, an earthquake swarm consisting of 113 events occurred between 04/07/2014 and 04/09/2014. No additional earthquakes were archived in the LBNL earthquake catalog outside of these dates. PyWCC identified an additional 103 events that also occurred during the time of the swarm. Interestingly, no additional events were identified outside the time period of the swarm.

SubTask 4: The PyWCC code was finalized. PyWCC (version 0.1.0) is a python code to compute seismic waveform cross-correlation on single- or multiple-component seismic data across a network of seismic sensors. PyWCC correlates wavefom data templates with continuous seismic data, associates the resulting detections, identifies the template with the highest cross-correlation coefficient, and outputs a catalog of detections above a user-defined absolute cross-correlation threshold value.

PyWCC is written in python 2.7 and currently has the following major package dependencies: NumPy, ObsPy, Python and SciPy. All run-time options are specified using an Input File. PyWCC computes the cross-correlation coefficient in the frequency-domain for increased computational speed. PyWCC computes the cross-correlation coefficient by convolving the two seismic signals and normalizing by the number of points and the product of the standard deviations. PyWCC makes use of built-in SciPy image modules to significantly improve the compute time associated with the standard deviations.

PyWCC is currently running and tested on Mac OS X, but should also be functional on Linux (32 and 64 bit) and Windows (32 bit and/or 64 bit). Memory space is a limiting factor when computing cross-correlation coefficients over an extended period of time (e.g., 24 hours), over a high sampling frequency (e.g., 500 Hz), and a low cross-correlation coefficient threshold (e.g., 0.0). The resulting internal arrays can become so large as to cause the operation to run out of memory on a typical desktop or laptop computer. Additionally, run times depend highly on computer load and user input specifications. On a typical desktop or laptop computer, the PyWCC package can determine cross-correlation coefficients for 24-hours of archived 100 Hz seismic data for a single template in approximately 3 minutes. In terms of disk space, the PyWCC package itself, with source code and example test case, needs at least 80 GB of space to download. The vast majority of the size of the distribution is due to the size of the 30-days of continuous data (78 GB).

PyWCC can be run on the command-line of standard computer terminal windows and on the command-line of Matlab application windows.